

A SEARCH FOR LIGHTLY IONIZING PARTICLES  
IN THE LUX DETECTOR AND R&D FOR FUTURE  
EXPERIMENTS

by

KATAYUN J KAMDIN

A dissertation submitted in partial satisfaction of the  
requirements for the degree of

Doctor of Philosophy

in

Physics

in the

Graduate Division

of the

University of California, Berkeley

Committee in charge:

Professor Daniel McKinsey, Chair

Professor Marjorie Shapiro

Doctor Peter Sorensen

Professor Kai Vetter

Summer 2018

## ABSTRACT

---

A Search for Lightly Ionizing Particles in the LUX Detector and R&D  
For Future Experiments

by

Katayun J Kamdin

Doctor of Philosophy  
University of California, Berkeley  
Professor Daniel McKinsey, Chair

Write the abstract here.

To my mom, for always making me feel like I could do this. To my friends, for being there when I was sure I couldn't.

## ACKNOWLEDGMENTS

---

Some Text

More Text.

More text

# CONTENTS

---

1	INTRODUCTION	1
I	THEORETICAL CONTEXT AND EXPERIMENTAL STRATEGIES	2
2	THEORETICAL BACKGROUND	3
2.1	A Little History . . . . .	3
2.2	Evidence for Dark Matter . . . . .	5
2.2.1	Galaxies and Clusters . . . . .	6
2.2.2	Cosmic Microwave Background . . . . .	8
2.3	Standard Models . . . . .	12
2.3.1	The Standard Cosmology . . . . .	12
2.3.2	The Standard Model of Particle Physics . . . . .	12
2.4	Dark Matter Candidates Motivated by Particle Physics .	14
2.4.1	WIMPs and the Hierarchy Problem . . . . .	14
2.4.2	Axions and the Strong CP Problem . . . . .	16
2.5	Motivation for LIPs . . . . .	17
2.6	Experimental Strategies for Detecting Dark Matter . .	17
2.6.1	Production . . . . .	17
2.6.2	Indirect Detection . . . . .	17
2.6.3	Direct Detection . . . . .	17
3	PARTICLE DETECTION WITH LIQUID XENON	18
3.1	Liquid Xenon as a Detector Medium . . . . .	18
3.1.1	Properties of Liquid Xenon . . . . .	18
3.1.2	Scintillation and Ionization Signal Generation	20
3.2	Dual-Phase Xenon Time Projection Chamber . . . . .	21
3.2.1	Energy Reconstruction . . . . .	23
3.3	Dual-Phase Xenon TPCs for Dark Matter Detection .	26
3.3.1	WIMP Searches with LXe TPCs . . . . .	26
3.3.2	Other Dark Matter Searches with LXe TPCs .	31
II	BIG SCIENCE	35
4	THE LUX DETECTOR	36
4.1	LUX Overview . . . . .	36
4.2	Internal Components . . . . .	36
4.3	External Components . . . . .	38
4.4	Trigger and Data Acquisition . . . . .	41
4.5	Data Processing . . . . .	43
4.6	Calibrations . . . . .	44
4.6.1	Energy . . . . .	45

4.6.2	Metastable Krypton-83 ( $^{83m}\text{Kr}$ ): A Multifunction Calibration . . . . .	46
4.6.3	Tritium Beta Decay: Calibration of the ER Band and Yields . . . . .	51
4.6.4	Low-energy nuclear recoils from Deuterium-Deuterium (DD) Neutrons: NR Band and Yields	53
4.6.5	Power of LUX Calibrations . . . . .	54
5	LIGHTLY IONIZING PARTICLE SEARCH	57
5.1	Modeling LIP Interaction . . . . .	57
5.1.1	Collision Cross Section . . . . .	57
5.1.2	Photo Absorption Ionization Model for Charge Particle Energy Loss . . . . .	58
5.1.3	Straggling . . . . .	59
5.1.4	Energy Resolution in LUX . . . . .	59
5.1.5	Position Resolution in LUX . . . . .	59
5.2	LIP Search . . . . .	59
5.2.1	LUX Run03 Conditions . . . . .	59
5.3	LIP Search Analysis . . . . .	59
5.3.1	Energy Consistency . . . . .	59
5.3.2	Track Linearity Criteria . . . . .	59
5.3.3	Background Rejection . . . . .	59
5.3.4	Muons . . . . .	59
5.3.5	Gammas . . . . .	59
5.3.6	Electron Trains? . . . . .	59
5.4	Result: Vertical Flux Limit . . . . .	59
III	LITTLE SCIENCE	60
6	RESEARCH AND DEVELOPMENT FOR FUTURE LXE TPCS	61
6.1	Test Bed Apparatus Overview . . . . .	61
6.2	Circulation System . . . . .	63
6.3	Charge Amplifiers . . . . .	63
6.3.1	Charge Amplifier Noise Behavior . . . . .	65
6.4	PMT . . . . .	67
6.5	Slow Control . . . . .	67
6.6	Data Acquisition . . . . .	68
6.7	High Voltage Feedthrough Design . . . . .	68
6.7.1	Implementing SHV Feed Throughs from Vacuum Suppliers . . . . .	69
6.7.2	Custom Feedthroughs . . . . .	75
7	SOLUBILITY OF RADON DAUGHTERS IN LIQUID XENON	79
7.1	Motivation . . . . .	79
7.1.1	Plate Out . . . . .	81
7.2	Experimental Configuration and Method . . . . .	82

## CONTENTS

7.2.1	Plate Out of $^{220}\text{Rn}$ Daughters . . . . .	84
7.2.2	Data Collection . . . . .	85
7.2.3	Calibration . . . . .	86
7.2.4	Position Reconstruction . . . . .	86
7.2.5	Fiducial Volume . . . . .	87
7.3	Analysis . . . . .	87
7.3.1	Number of $^{220}\text{Rn}$ daughters in the TPC . . . . .	87
7.3.2	Data Selection . . . . .	87
7.4	Results and Discussion . . . . .	90
8	ELECTRON TRAIN STUDIES	98
8.1	Electron Train Studies . . . . .	98
8.1.1	Motivation . . . . .	98
8.1.2	Experimental Configuration . . . . .	98
8.1.3	Results . . . . .	98
IV	APPENDIX	99
A	DUMMY APPENDIX	100
	BIBLIOGRAPHY	101

## LIST OF FIGURES

---

Figure 1	Superposition of 21 Sc rotation curves from galaxies with a large range of radii and luminosities. All galaxies have a distinctive flat rotation curve at large radii. Figure from [5]. . . . .	4
Figure 2	CfA Redshift Survey result showing the distribution of galaxies in a strip on the sky about 6 degrees wide and 130 degrees long. The radial coordinate is redshift, in km/sec, calculated with a Hubble constant of 20km/sec/million ly.	5
Figure 3	Galactic rotation curve from [9] . . . . .	6
Figure 4	(left) The visible light image from the Magellan telescope of the merging Bullet Cluster overlaid with the weak lensing measurement contours in green, and white 68.3%, 95.5%, and 99.7% confidence levels for the weak lensing peaks. (right) The Chandra x-ray image overlaid with the same weak lensing measurement. Figure from [20] .	8
Figure 5	(left) The FIRAS instrument on the COBE satellite mission measured the Cosmic Microwave Background ( <a href="#">CMB</a> ) temperature to be $2.7377 \pm 0.0038$ K. (right) The FIRAS instrument also confirmed the perfect Planck black body spectral shape of the <a href="#">CMB</a> radiation. Figures from [21] .	9
Figure 6	(top) The relative spatial resolution of COBE, WMAP, and Planck. Figure courtesy of NASA. (bottom) The Mollweide projection of the Planck 2013 CMB temperature map. The color scale represents fluctuations of $\pm 30 \mu\text{K}$ around a central value of 2.7377 K. Figure courtesy of ESA and the Planck Collaboration. . . . .	9
Figure 7	The angular power spectrum from Plank 2018 results [23] . . . . .	11
Figure 8	The effect of baryons (left) and total matter (right) on the magnitude and location of <a href="#">CMB</a> angular power spectrum peaks. [22] . . . . .	11

Figure 9	The particles that comprise the standard model of particle physics, including names, spins, masses, and charges. It is also indicated which fermions interact with which bosons, e.g. gluons interact with the quarks but not with the leptons. . . . .	13
Figure 10	(left) The co-moving number density $Y$ (left y-axis) resulting in the thermal relic density $\Omega_\chi$ (right y-axis) for a dark matter particle of mass $m_\chi=100$ GeV. The solid black line is the annihilation cross section which yields the correct relic density and bands indicate cross sections that differ by successive factors of 10 from the “correct” annihilation cross section (right) A band of natural values for a thermal relic $\chi$ that composes different percentages of the observed dark matter content. The width of the band is set by the deviation of $g$ from $g_{weak}$ in Equation 8, Figures from [26] . . . . .	16
Figure 11	(left) Diagram of a dual-phase xenon time projection chamber. The time difference between S1 and S2 gives the depth ( $z$ ) of the interaction, and $(x, y)$ is reconstructed from the S2 signal. (right) Diagram summarizing the generation of the scintillation and ionization signal generation in dual-phase xenon time projection chambers. . . . .	22
Figure 12	(left) Plot illustrating the effect of recombination and detector effects on a line source ( $^{127}\text{Xe}$ ), courtesy of E. Pease. (right) Field dependence of scintillation and ionization yield in LXe for 122 keV electron recoils (ER), 56.5 keV nuclear recoils (NR) and 5.5 MeV alphas, relative to the yield with no drift field from [40] . . . . .	24
Figure 13	Plots showing combined energy contours in two common sets of axis units, for an example set of $g_1$ and $g_2$ . . . . .	25
Figure 14	Plot showing ER and NR bands from LUX. Solid lines are the ER and NR Gaussian means $\mu$ , dotted lines are $\mu \pm 1\sigma$ . Figure from [37] . . . . .	27

Figure 15	Plot showing spin-independent WIMP rates in common detector target materials, dots indicate typical thresholds for the targets. Xenon gains in favored SUSY parameter space ( $M_\chi \gtrsim 100$ GeV) due to a kinematic enhancement ( $M_\chi \sim M_{Xe}$ ) and a cross-section enhancement ( $\sigma_{SI} \propto A^2$ ). Figure from [45] . . . . .	30
Figure 16	Projected limits of next-generation dark matter detectors and areas where SUSY models predict the presence of WIMPs. Although Xe (LZ, green dashed) performs better for WIMP parameter space, Ge and Si (SuperCDMS, blue dashed) can access other light dark matter parameter space below 10 GeV. The plot was generated by <a href="http://dmtools.brown.edu/">http://dmtools.brown.edu/</a>	30
Figure 17	Xenon 10 low-mass WIMP limit extended the range of the standard WIMP result. . . . .	32
Figure 18	(left) Top: Expected 1,2,3-electron signal rates for Sub-GeV DM with $\sigma_e = 10^{-36} \text{ cm}^2$ and Bottom: exclusion limit set with Xenon10 few-electron signals. (right) Exclusion limits for dark matter scattering through an electric-dipole moment (red) and through a very light ( $\ll$ keV) mediator (blue) . . . . .	33
Figure 19	(left) Recent limits on solar axion coupling and mass (right) recent limits on galactic axion coupling and mass. Figure taken from [54]. . . . .	34
Figure 20	Major components and dimensions of the LUX detector. . . . .	37
Figure 21	Field-shaping rings detail . . . . .	38
Figure 22	A simplified diagram of the LUX cryogenic system. [55] . . . . .	39
Figure 23	A photo of the LUX detector installed inside the water tank. . . . .	40
Figure 24	Backgrounds distributions in squared radius and height for expected (right) and measured (left) backgrounds in the energy range 0.9-5.3 keV <sub>ee</sub> (2-30 phe S1) for the 85.3 live-day Run03 Weakly Interacting Massive Particle (WIMP) exposure. Black lines show the 118 kg fiducial mass. Units are log <sub>10</sub> DRU <sub>ee</sub> , electron equivalent differential rate units, i.e. keV <sub>ee</sub> <sup>-1</sup> kg <sup>-1</sup> day <sup>-1</sup> . Figure from [58]. . . . .	41

Figure 25	Overview of the LUX trigger system. Figure from [59]. . . . .	41
Figure 26	An example recorded event. Channels that do not pass the POD threshold are not recorded. The waveforms are summed over all channels to produce the S1 and S2 [59]. . . . .	42
Figure 27	An example of Large Underground Xenon ( <a href="#">LUX</a> ) pulse classification showing individual pulses. . . . .	44
Figure 28	Plot showing calibration sources (Figure from [39]). The axis label subscript $c$ denotes corrected variables with calibration for geometrical effects and electron lifetime (these corrections are discussed in Section 4.6.2). . . . .	45
Figure 29	Doke plot used to fit $g_1$ and $g_2$ for LUX Run03 (Figure from [39]) . . . . .	46
Figure 30	Spatial dependence of pulse area corrections for S1 (left) and S2 (right) from an example $^{83m}\text{Kr}$ calibration. The red circle indicates normalization point. (Figure from [62]) . . . . .	48
Figure 31	(Left) A simplified 2D COMSOL model showing electric field lines and equipotentials for the <a href="#">LUX</a> detector in Run03. A radially inward component is seen. (Right) The resulting edge S2 coordinates of a uniform distribution of electrons drifted under the electric field model is shown in solid blue. The edge S2 coordinates of from $^{83m}\text{Kr}$ data is in dashed red; it is consistent with the field model prediction. Figure from [62] . . . . .	49
Figure 32	The effect of radial position mapping between S2 coordinates (left) and real coordinates (right). The top panels show a thin horizontal slice of the detector and the bottom panels show a thin vertical slice. The red and blue colors are to make the effect of the mapping visible. Note that squared radius in the bottom panels exaggerates the scale of the effect. Figure from [62] . . . . .	50
Figure 33	Field map of Run03 produced by $^{83m}\text{Kr}$ S1a:S1b ratio. Because only a fraction of $^{83m}\text{Kr}$ produce separate S1a and S1b, the bins are large to accommodate reduced statistics. Figure from [62] . . . . .	51

Figure 34	(Left) Plot showing the theoretical tritium beta spectrum with the spectrum obtained from data, and residuals. (Right) The ratio of data to theory convoluted with the detector energy resolution. Figure from [63] . . . . .	52
Figure 35	(Left) The measured quanta yields shown with lines of equal energy. (Right) A plot depicting the expected initial quanta yields, $N_{ion}$ and $N_{ex}$ , compared with the measured yield of photons and electrons. The difference is caused by the energy dependence of recombination. Figure from [63] . . . . .	52
Figure 36	(Left) The Electron Recoil ( <b>ER</b> ) band for in <b>WIMP</b> search energy range obtained from the tritium calibration. (Right) Leakage fraction of <b>ER</b> events below the Nuclear Recoil ( <b>NR</b> ) mean in the <b>WIMP</b> search energy range. Knowledge of the <b>NR</b> band comes from the DD calibration detailed in Section 4.6.4. Figure from [63] . . . . .	53
Figure 37	(Right) Photo of the water tank interior showing the neutron conduit, which is raised during Deuterium-Deuterium ( <b>DD</b> ) calibration. (Left) Diagram of the <b>DD</b> generator and water tank neutron conduit during <b>DD</b> operation. Figure courtesy of E. Pease. . . . .	54
Figure 38	Calibration showing the <b>NR</b> band mean and width from the <b>DD</b> calibration. Figure from [66] . . . .	55
Figure 39	Improved spin-independent <b>WIMP</b> limit of the Run03 exposure following the <b>DD</b> calibration of <b>LUX</b> . The first Run03 limit is the gray line labelled “LUX 2014”, the improved Run03 observed limit is the black line labelled “This Result”. Figure from [67] . . . . .	56
Figure 40	Large scale view of the experimental apparatus showing key parts. . . . .	62
Figure 41	Diagrams of two often used internal arrangements. . . . .	62
Figure 42	Pumping and instrumentation diagram of the test bed. Special symbols are labelled in the diagram, see key for other symbols. For readability, all gauges are not shown. . . . .	63

Figure 43	A picture of the CR-110 charge amplifier from the manufacturer's data sheet, shown with an equivalent circuit diagram. . . . .	64
Figure 44	A raw and shaped charge amp signal taken in -100C gaseous xenon, with the radon source plumbed in . . . . .	64
Figure 45	(Left) original mounting of CR-110 charge amplifiers inside the experimental vessel. (Right) Mounting in the outer vacuum reduced heat load on the TPC. . . . .	65
Figure 46	Different lengths of BNC cable attached to a CR-110 test board. . . . .	66
Figure 47	(Left) Event showing charge amp with detector -100 C, 1.5 bar, gas only. (Middle) Effect of circulation pump on charge amp is to cause 500 Hz oscillation noise (-100 C, 1.5 bar, gas only). (Right) Same event as (middle), but zoomed-in time scale. . . . .	66
Figure 48	(Left) Periodic noise from the Glassman 20 kV negative polarity voltage supply. (Right) Partial breakdown in R60 cable as picked up by charge amplifiers. . . . .	67
Figure 49	A diagram showing components of the slow control. . . . .	68
Figure 50	A 12kV SHV weldable connector from vacuum supplier Kurt Lesker. . . . .	70
Figure 51	(left) The copper tape in this picture is sitting on top of a 1/2 -in swage connector. The swage connector captures a 1/2 in pipe, which has the 12 kV SHV feedthrough welded to the end. (right) 12 kV SHV weldable connector, inverted, clipped, and attached with a machined copper connector. The connector uses a screw to capture the SHV feed though, and the same screw to capture a stranded wire, visible in this picture, which is then fed through a hole drilled in the PTFE to connect to the wire grid frames. The wire was wrapped around the grid frame. . . . .	70
Figure 52	The same 12kV SHV feed through, now with a modified spring connection connecting the feed through to the grid frame. A close up of the cathode grid showing the spring connection is on the <b>right</b> . . . . .	71

Figure 53	Oscilloscope showing baseline rate of single photons (left) compared to a high rate of single photons (right) caused by the high voltage feed through. . .	71
Figure 54	(Left) Full xenon breakdown as visible on the PMT trace. The large, saturated pulse is caused by the high intensity of light. This type of breakdown was often accompanied by an audible buzz, and a rise in current that would initiate a trip of the high voltage supply. (Right) a close up of the xenon-facing side of the feedthrough. Visible gaps where xenon gas is exposed to high fields are particularly problematic for breakdowns. . .	72
Figure 55	Top: (left) cathode connection side (right) SHV-20 connection side Bottom: (left) an example showing how the cable was attached to the stock SHV-20 feed though end (right) a custom cap fit over the connection, smoothing out triple points. . .	73
Figure 56	Effect of holding the feed through in place with PEEK zip ties was explored, effects were minimal. . .	73
Figure 57	The black line shows the aging observed in the course of normal operations. The red line shows breakdown tests of the SHV-20 feed though in gas, illustrating that the aging observed during operation was due to aging of the feed though. . .	74
Figure 58	First attempt at a custom feed through built out of Swagelock parts combined with basic materials like PTFE and stainless steel rods. The orientation shown (left) was later inverted due to concerns of temperature stress and pressure stress on the PTFE ferrules. The feedthrough as assembled (center) was functional, but higher voltage capability was desired. The effect of adding a grounding braid (right) was found to decrease the voltage capability instead of increasing it. . .	75
Figure 59	(top) Input to a COMSOL model simulating gaps between the grounding braid and dielectric of a high voltage feedthrough. (bottom) COMSOL output the model, showing that peak fields arise when gaps exist between dielectric and grounding braid.. Both images provided by high voltage engineer W. Waldron. . . . .	76

Figure 60	Top: (left) Close up showing the PTFE ferrules and notch. (right) Close up of the sealed top connection; epoxy was added to prevent leaks between the dielectric and conductor rod . Bottom: (left) Threaded U-bend cathode connector (right) Feed through assembled and installed. . . . .	77
Figure 61	Top: (left) Sealed top connection with liberal epoxy use. A male Bendix pin was soldered to the cable conductor. (middle) SHV connector with female Bendix to mate with feedthrough (right) Grounded safety housing with SHV connector. Bottom: (left) Ends of the feedthrough were held in the Teflon stack. (middle) Close up showing cable conductor, PTFE dielectric, and grounding sheath pulled back (right) Grounding scheme for feedthrough cables. . . . .	78
Figure 62	The $^{222}\text{Rn}$ decay scheme. The fast and slow chains are indicated. . . . .	80
Figure 63	Pathways to radon and radon daughter contamination. . . . .	81
Figure 64	Diagram of the test bed. For this study, the cathode is held at -6.0 kV, and the grid is held at -4.0 kV. $E_1^{\text{liq}} \approx 5.0 \text{ kV/cm}$ , $E_1^{\text{gas}} \approx 10.0 \text{ kV/cm}$ $E_2 = 1.0 \text{ kV/cm}$ . $E_3 = 2.7 \text{ kV/cm}$ . The large gray regions represent the structural rings of PTFE. The line between the grid and anode represents the liquid xenon level. The xenon inlet pipes incoming gas directly into the liquid region, and the liquid outlet pulls from the level of the active region. A gas outlet (not pictured) also draws xenon gas into the circulation system to be purified. . . . .	83
Figure 65	An example a circulation path used for plate out is shown on the pumping and instrumentation diagram. During data-taking the radon source was bypassed. The typical liquid level is indicated on the diagram to show that the outlet drew from the liquid via a capillary, ensuring purification of the liquid xenon. A gas purge also purified the gas column in the detector. . . . .	84
Figure 66	The $^{220}\text{Rn}$ decay scheme. The fast and slow chains are indicated. Events in the plate out data sets are from the slow chain. . . . .	85

Figure 67	a) and (b) and (c) show the plateout conditions of datasets A, B, and C, respectively. The gray bands indicate time when data was being acquired. Dataset D (calibration) was taken following dataset A and consisted of a few hours. . . . .	88
Figure 69	Monte Carlo study to find the maximum distance a $^{212}\text{Bi}$ beta (2.2 MeV) on the cathode could penetrate into the drift region. The projected range (red) is the relevant curve for this analysis; it shows a beta is not expected to travel more than 1.2mm from the cathode. . . . .	92
Figure 70	For datasets A and B: <b>(left)</b> Distribution of events in $z$ . <b>(right)</b> The same events distributed in the S1-S2 plane, showing selection criteria for candidate $^{212}\text{Bi}$ alpha events in the bulk liquid xenon.	93
Figure 71	For datasets C and D: <b>(left)</b> Distribution of events in $z$ . <b>(right)</b> The same events distributed in the S1-S2 plane, showing selection criteria for candidate $^{212}\text{Bi}$ alpha events in the bulk liquid xenon.	94

## LIST OF TABLES

---

Table 1	Summary of plate out and data-taking conditions. Data sets A and B are taken after circulating radon gas and data set C, background, had no radon circulation. Data set D was taken following dataset A, and radon was circulated in a liquid xenon environment, purposefully introducing radon into the detector bulk to calibrate the detector. . . . .	86
Table 2	Calculations of fiducial volume. Liquid level is taken to be $14 \pm 1$ mm. Density of Liquid Xenon ( <a href="#">LXe</a> ) near boiling point is 2.9 g/mL. . . . .	87
Table 3	Number of detected alpha particle events whose energy determination was consistent with $^{212}\text{Bi}$ decay to $^{208}\text{Tl}$ . Live times are quoted in Table 1	92
Table 4	Using observations from 3, proceed through solubility calculation. . . . .	97

## ACRONYMS

---

- SM Standard Model
- BSM Beyond the Standard Model
- SUSY Supersymmetry
- MSSM Minimal Supersymmetric Model
- LSP Lightest Supersymmetric Particle
- WIMP Weakly Interacting Massive Particle
- LIP Lightly Ionizing Particle
- CDM Cold Dark Matter
- MOND Modified Newtonian Dynamics
- NFW Navarro-Frenk-White
- CMB Cosmic Microwave Background **GUT!** (**GUT!**)Grand Unified Theory Lightest Supersymmetric Particle (**LSP**)Lightest Super Partner
- LUX Large Underground Xenon
- LXe Liquid Xenon
- TPC Time Projection Chamber
- SURF Sanford Underground Research Facility
- ER Electron Recoil
- NR Nuclear Recoil
- VUV Vacuum Ultra Violet
- DPF Data Processing Framework
- LUG LUX Electronic Log
- DAQ Data Acquisition
- FPGA Field Programmable Gate Array

POD Pulse Only Digitization  
ADC Analog-to-Digital Converter  
SE Single Electron  
SPHE Single Photoelectron  
LRF Light Response Function  
RQ Reduced Quantity  
DD Deuterium-Deuterium  
PVC Polyvinylchloride  
MFC Mass Flow Controller  
HV High Voltage  
SHV Safe High Voltage  
SS Stainless Steel  
CF Conflat  
PMT Photomultiplier Tube  
QE Quantum Efficiency  
EEE Electron Extraction Efficiency  
LBNL Lawrence Berkeley National Laboratory  
PTFE Polytetrafluoroethylene  
PEEK Polyether ether ketone  
RMS root mean square  
CCS Collisional Cross Section  
PAI Photo Absorption Ionization  
FVP Fermi Virtual Photon

# 1

## INTRODUCTION

---

*I was dreamin' when I wrote this, forgive me if it goes astray.*

— Prince, 1999, 1989

This Thesis is laid out in three main sections. The first section deals with the evidence for dark matter, theoretical background for different dark matter candidates, and an overview of experimental strategies to detect dark matter, going into detail for one particular detection strategy, the dual-phase [LXe](#) Time Projection Chamber ([TPC](#)).

The second section, Big Science, delves into details about the [LUX](#) detector, a dual-phase [LXe TPC](#), and presents a search for the Lightly Ionizing Particle ([LIP](#)) dark matter candidated carried out with [LUX](#) data.

The last section, Little Science, describes an R&D test bed that was built at L ([LBNL](#)) over the course of this PhD and describes two studies completed with the test bed.

## PART I

# THEORETICAL CONTEXT AND EXPERIMENTAL STRATEGIES

This section describes the theoretical foundation for the analysis presented in [Part II](#). It includes an overview of the Standard Cosmology...

# 2

## THEORETICAL BACKGROUND

---

### 2.1 A LITTLE HISTORY

Our understanding of the universe develops in a leap-frog of theory and observation, one catching up to and surpassing the other as technology improves, to be passed in turn by a new idea or new observation. The picture of dark matter commonly accepted today is much different than what Zwicky anticipated in 1933 when he found that the velocity dispersion of the galaxies in the Coma Cluster was much larger than expected from the Virial Theorem [1]. This observation is typically cited as popularizing the term “dark matter”, and starting the hunt for the mysterious invisible substance. Zwicky postulated that the faster rotation was caused by dark matter consisting of cold gas or stars and both macro- and micro-scopic solid bodies, and estimated that there was about 400 times more dark matter than visible matter. Smith, a contemporary of Zwicky’s, did a similar analysis with the Virgo Cluster and his results yielded a much smaller dark matter to visible matter ratio [2]. Meanwhile, many in the astrophysics community disagreed with an underlying assumption of these analyses and argued that galaxy clusters are not at equilibrium so the Virial Theorem does not apply [2]. At the time, the only consensus reached was that more information was needed to understand the dynamics of galaxy clusters.

In the 1970’s, a new technology called the image tube spectrograph allowed Vera Rubin and Kent Ford, the developer of the spectrograph, to measure the rotational velocity of the Andromeda Galaxy at different points along its radius (called a galactic rotation curve) [3]. The new data was of higher quality than previous attempts at measuring galactic rotation curves, and the result, that the galaxy was rotating faster than expected at large radius, indicating “hidden mass”, was soon replicated by others [2]. Over the next decade, a significant number of galactic rotation curves were obtained, all showing essentially the same result: galaxies were rotating faster than expected at high radii, indicating that the mass of galaxies continued to grow past where their lights dimmed. A figure showing this characteristic behavior in 21 galaxies from a 1980 review paper by Rubin, Ford, and Thonnard is shown in Figure 1. Another

argument in favor of dark matter came from contemporary numerical simulations of galactic gravitational dynamics. At first, many simulations showed that disk galaxies were unstable, in contradiction with many observations [2]. However, Ostriker and Peebles demonstrated that if the galactic disk was embedded in a massive (i.e. gravitationally interactive) spherical halo, the disk was stable [4].

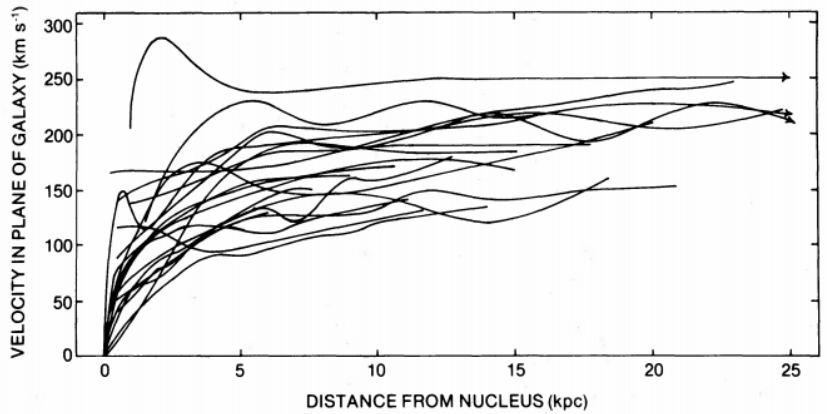


Figure 1: Superposition of 21 Sc rotation curves from galaxies with a large range of radii and luminosities. All galaxies have a distinctive flat rotation curve at large radii. Figure from [5].

In order to explain the behavior of galactic rotation curves without dark matter, Milgrom proposed Modified Newtonian Dynamics (**MOND**) in a trio of 1983 papers, [6], [7], [8]. Milgrom showed that if Newtonian dynamics was modified from  $F = ma$  to  $F = ma/a_0$ , for a  $\ll a_0 \approx 1.2 \times 10^{-10} m/s^2$  the observed galactic rotation curves could be accounted for without requiring any hidden or dark matter. Milgrom's goal in these first papers describing **MOND** was to present an approximate limit of some as-yet unknown full theory, which he and others went on to develop in the following decades [2]. However, theoretical and technological advancements in the fields of cosmology and astronomy have made **MOND** an unsatisfying theory, unable to explain several observed phenomena. Of these phenomena, gravitational lensing and **CMB** are discussed further below.

Big-Bang cosmology had a large success in 1965 with Penzias and Wilsons' observation of the **CMB**. It was in the 1980's however, that cosmology, particle physics, and astronomy became tied together as they are understood today, and dark matter came to refer to an as yet undiscovered particle species and not the cold gas and stars of Zwicky's day [2]. Cosmological inflation, a period of exponential expansion  $10^{-36}$  to  $10^{-33}$  seconds after Big Bang was proposed. Without an inflationary period, fluctuations would be washed out as the universe expanded, leading to a universe de-

void of structure. Inflation, however, provides mechanism for quantum fluctuations to be ‘blown up’ and seed the structure observed by the 1982 CfA redshift survey (Figure 2). Numerical simulations to reproduce the structure seen by the CfA redshift survey benefited from new improvements in processing speed and numerical techniques, and also from the new theory of inflation, which provided a physical reason for initial density perturbations [2]. The structure was reproduced only in the presence of gravitationally-interacting dark matter. It is interesting to note here that these cosmological simulations were largely insensitive to any additional, non-gravitational interactions the dark matter had, as long they were sufficiently weak. However, the simulations did require the dark matter to be non-relativistic or “cold”. Such dark matter is referred to as Cold Dark Matter ([CDM](#)), and plays a prominent part in the standard cosmology to describe the structure and evolution of our universe at all scales.

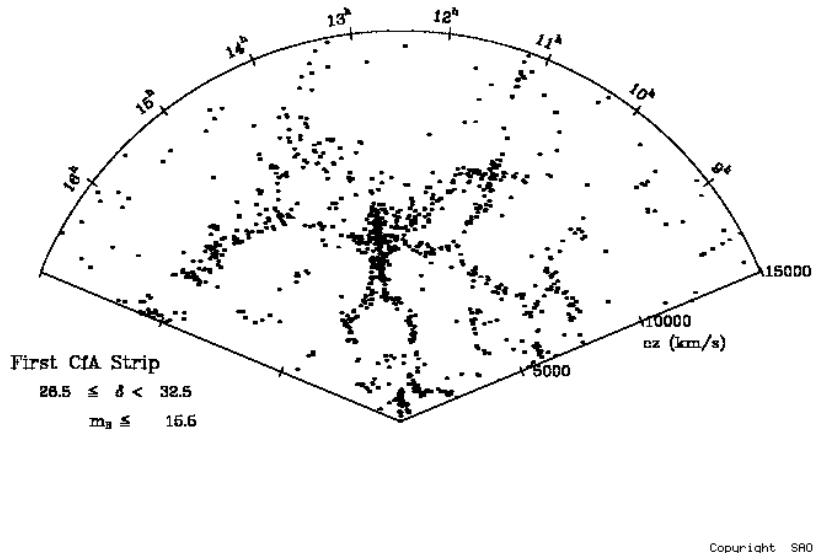


Figure 2: CfA Redshift Survey result showing the distribution of galaxies in a strip on the sky about 6 degrees wide and 130 degrees long. The radial coordinate is redshift, in km/sec, calculated with a Hubble constant of 20km/sec/million ly.

## 2.2 EVIDENCE FOR DARK MATTER

The previous section gave an overview of why [CDM](#) has become, over the last century, the leading paradigm to explain the small and large-scale

structure observed in our universe. The following subsections deal with particular pieces of evidence, discussed in detail.

## 2.2.1 GALAXIES AND CLUSTERS

Galactic rotation curves were discussed above, as evidence for dark matter halos. Here we further discuss the properties of dark matter halos. An example of a galactic rotation curve of a spiral galaxy showing the presence of an inferred dark matter halo is shown below in Figure 3. Each side of Figure 3 shows the same galaxy, NGC 3198, but fit with a different disk and halo model. In this particular example from 1985, the authors note their uncertainty about which halo model is the correct one: “Should one seriously consider the case where the amount of visible matter is negligible with respect to the amount of dark matter [Figure 3 (left)]? Or is the maximum disk case [Figure 3 (right)] closer to the truth?” [9]. A decade later, in 1996, Navarro, Frenk and White published a paper describing high-resolution simulations of CDM, which could all be fit with a universal dark matter halo profile [10]. This formula became known as the Navarro-Frenk-White (NFW) profile; it is still widely used today, and is the basis for many direct detections experiments, including LUX.

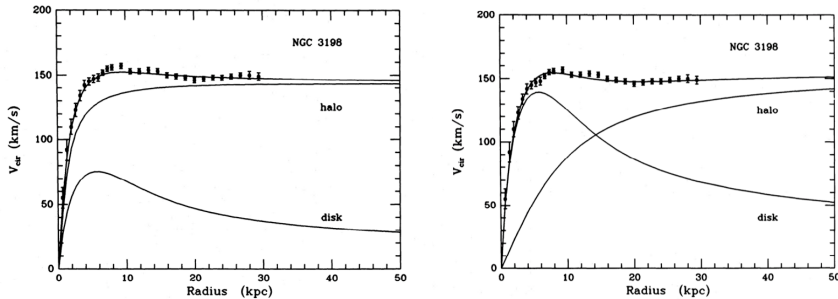


Figure 3: Galactic rotation curve from [9]

The astrophysics community is near unanimous that galaxies have a dark matter component. Today, research continues into the particular shape of the dark matter profile. While NFW is in common use and agrees with many observations, it is not consistent with observations of low surface brightness and dwarf galaxies [11], [12]. This known as the core-cusp problem: NFW galaxies have an over-density of dark matter at small radius (cuspy), while dwarf galaxies favor flatter density profiles (core). Some argue that such behavior may be a consequence of the nature of dark matter, or that current simulations are not sufficient to properly understand dwarf galaxies [13]. Others argue that a cusp can be changed to a core via baryonic feedback that arises in simulations of active galactic nuclei [14]. Other current research centers on the globular clusters

and stars that orbit the Milky Way. These researchers look for evidence of halo substructure and streams of dark matter from the movements of stars orbiting the Milky Way. Data from the Gaia satellite, launched in 2013, calls into question whether dark matter halos are truly in equilibrium, which has consequences for direct detection experiments, as it would change the expected dark matter recoil spectrum [15] [16]. In addition to the stars and globular clusters orbiting the Milky Way, there could be clusters of dark matter more dense than the surrounding halo. Telescope data shows evidence for dark matter halo substructure in the Milky Way [17], and simulations expect upcoming data from LSST to further contribute to understanding of Milky Way halo substructure and rule out certain dark matter halo models [18].

Galaxy clusters make up some of the strongest direct evidence for dark matter though the method of gravitational lensing. A gravitational lens is created when a massive object is located between a light source and an observer. General relativity requires photons to propagate on the null geodesics of spacetime, meaning the path the light takes from the source will be bent by the distorted space-time of the the massive object. Thus images of background galaxies are distorted by invisible mass along the line of sight from the observer. Being dependent on general relativity, and therefore Newtonian dynamics, the numerous observations of gravitational lensing in large structures strongly disfavor MOND.

There are a few types of gravitational lensing: strong, weak, and microlensing. Weak lensing has been used to observe dark matter in large scale structures (galaxy clusters); the other types of lensing are not treated here. In weak lensing, the light sources are far away from the foreground mass (or the mass is small). Several light sources are required, and the location of mass is statistically reconstructed. The Bullet Cluster (1E0657-558) is one of the most dramatic weak lensing measurements: it is actually the collision of the galaxy cluster 1E0657-56 and smaller cluster (the “bullet”) [19]. The x-ray image of the collision, by the Chandra x-ray observatory, shows the location of the baryonic matter. The baryonic matter suddenly slowed down upon the collision, emitting shock x-rays [19]. The authors of [19] call it “a textbook example of a bow shock”, indicating the x-ray behavior is well understood. A few years later, Clowe et al. also call the Bullet Cluster “a direct empirical proof of the existence of dark matter.” Their weak lensing observations show the location of the large, invisible (in x-ray and visible light) mass centers of the two clusters to be offset from the location of the baryonic matter at a significance of  $8\sigma$  [20]. In the collision, the dark matter halos of the two clusters are expected to pass through each other without slowing down, while the baryonic matter of the two clusters interacts, slowing down. The weak lensing measurement is shown overlaid with the visible and x-ray images in Figure 4.

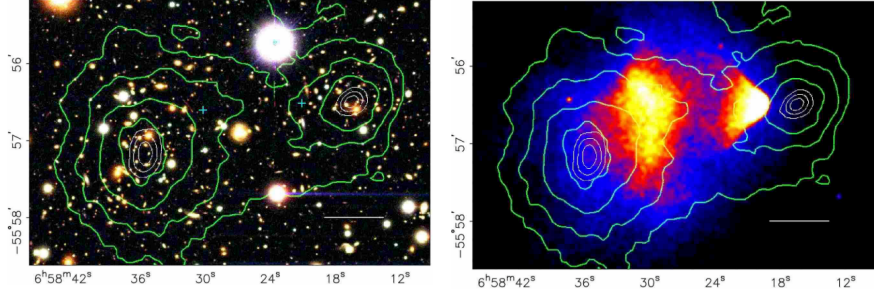


Figure 4: (left) The visible light image from the Magellan telescope of the merging Bullet Cluster overlaid with the weak lensing measurement contours in green, and white 68.3%, 95.5%, and 99.7% confidence levels for the weak lensing peaks. (right) The Chandra x-ray image overlaid with the same weak lensing measurement. Figure from [20]

## 2.2.2 COSMIC MICROWAVE BACKGROUND

In the thermal history of our universe, the term recombination refers to the epoch when temperatures had cooled enough to allow electrons and protons to combine into hydrogen, leaving photons to propagate freely through the universe. The photons should have decoupled from the matter as a black body peaked at the temperature of recombination,  $\approx 3000$  K. The relic radiation from this epoch is visible today as the [CMB](#), where the continuing expansion of the universe has redshifted the photons to a temperature of  $\approx 2.7$  K. The [CMB](#) photons are also referred to as the light of last scattering, referring to the interaction the photons had with free electrons before the electrons became bound to protons in hydrogen. The temperature of the [CMB](#) was precisely measured to be  $2.7377 \pm 0.0038$  K by the COBE mission, which also confirmed its perfect adherence to a black body spectrum [21] (Figure 5).

While the COBE satellite mission's measurements of the [CMB](#) provided strong support for the Big Bang model of cosmology, it was COBE's discovery of anisotropies in the [CMB](#) that eventually led to powerful evidence for [CDM](#). Since COBE, two more [CMB](#) satellite missions, WMAP and Planck, have launched and gathered data, each with successively higher spatial and energy resolution. The relative resolutions of COBE, WMAP, and Planck are shown in Figure 6 along with the full Planck [CMB](#) anisotropy map. The scale of the anisotropy fluctuations represent a scale of  $\pm 30 \mu\text{K}$ ; the [CMB](#) power spectrum remains the most perfect black body spectrum observed in nature.

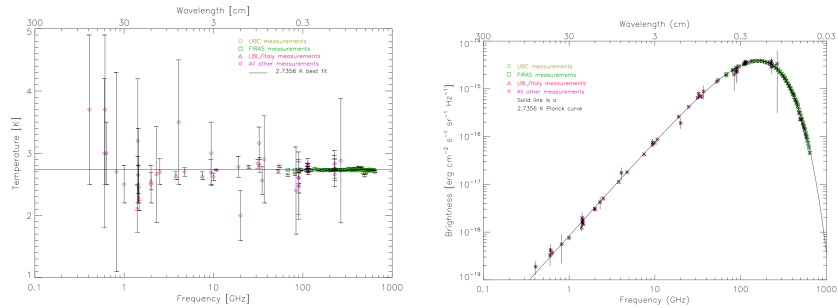


Figure 5: (left) The FIRAS instrument on the COBE satellite mission measured the CMB temperature to be  $2.7377 \pm 0.0038$  K. (right) The FIRAS instrument also confirmed the perfect Planck black body spectral shape of the CMB radiation. Figures from [21]

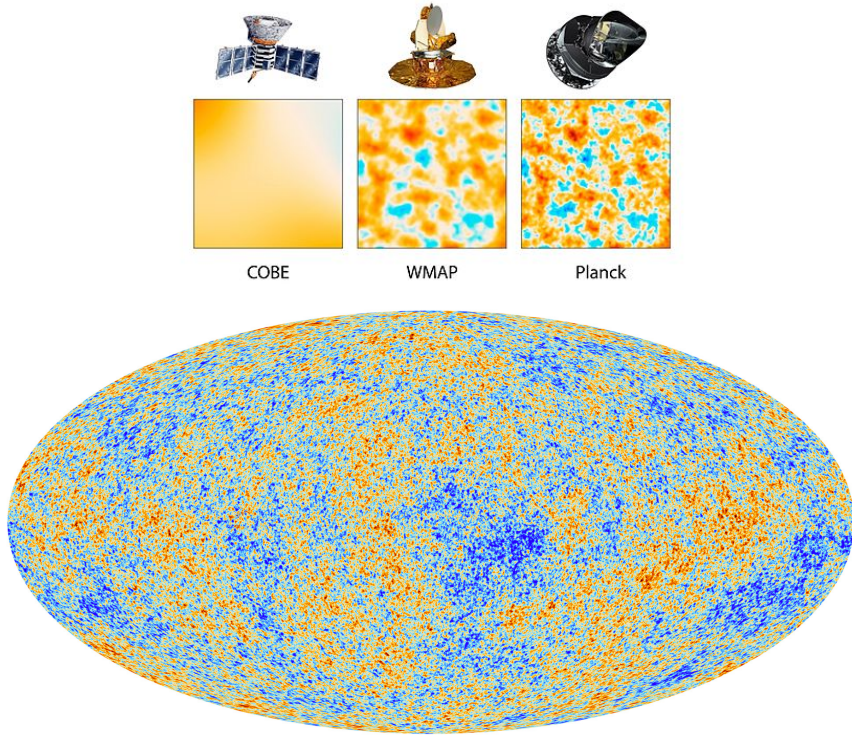


Figure 6: (top) The relative spatial resolution of COBE, WMAP, and Planck. Figure courtesy of NASA. (bottom) The Mollweide projection of the Planck 2013 CMB temperature map. The color scale represents fluctuations of  $\pm 30 \mu\text{K}$  around a central value of 2.7377 K. Figure courtesy of ESA and the Planck Collaboration.

The fluctuations  $\Delta T(\theta, \phi)$  of the CMB map shown in Figure 6 can be decomposed into its basis components via Fourier analysis, where each expansion component is represented by the spherical harmonics,  $Y_{lm}$ :

$$\Delta T(\theta, \phi) = \sum_{l=2}^{\infty} \sum_{m=-l}^l b_{lm} Y_{lm}(\theta, \phi) \quad (1)$$

The sum leaves out the  $l = 0$  (mean) and  $l = 1$  (dipole Doppler shift caused by movement of the earth) components, which were subtracted from the CMB temperature map, leaving only the fluctuations as in Figure 6. The power spectrum of the temperature fluctuations, which is calculated by squaring Equation 1, averaging it over all points that have the same angular separation  $\theta$ , and performing an integral over all  $m$  (because the temperature anisotropies have no preferred direction), encodes all the statistical variation in the CMB sky (see, e.g. [22] for a derivation). The angular correlations of the different multipole moment  $l$  are typically extracted from this power spectrum and plotted as function of  $l$  and the coefficients  $C_l$  from the power spectrum. This quantity is referred to as the angular power spectrum and takes the form:

$$D_l^{TT} = \frac{l(l+1)}{2\pi} C_l \quad (2)$$

where the  $TT$  superscript denotes temperature anisotropies (polarization anisotropies, not discussed here, can be parameterized similarly). The latest angular power spectrum from Planck is shown in Figure 7.

The location and magnitude of peaks in the angular power spectrum (Figure 7), constrain the curvature, content, and evolution of our universe. The physical interpretation of the CMB is as follows: photons from the time of last scattering, newly free to propagate through the universe, carry information about the density fluctuations in the plasma from which they decoupled. The plasma, which was then composed of photons, baryons, and dark matter, behaved as an oscillator driven by gravitational attraction, with a restoring force from the fluid pressure of the plasma. The maxima of the angular power spectrum indicate extrema, overdensities or underdensities, in the plasma. The presence of baryons increases the magnitude of odd peaks relative to even peaks. The physical interpretation of this is that baryons add inertia to the oscillator system, causing an increase in compression (odd) compared to expansion (even) [22]. The presence of dark matter is apparent in the relative heights of the second and third peak in the spectrum. The driving force of the oscillator is total matter content (baryons + dark matter,) which contributes to odd peaks, while baryons contribute characteristically to the even peaks. A

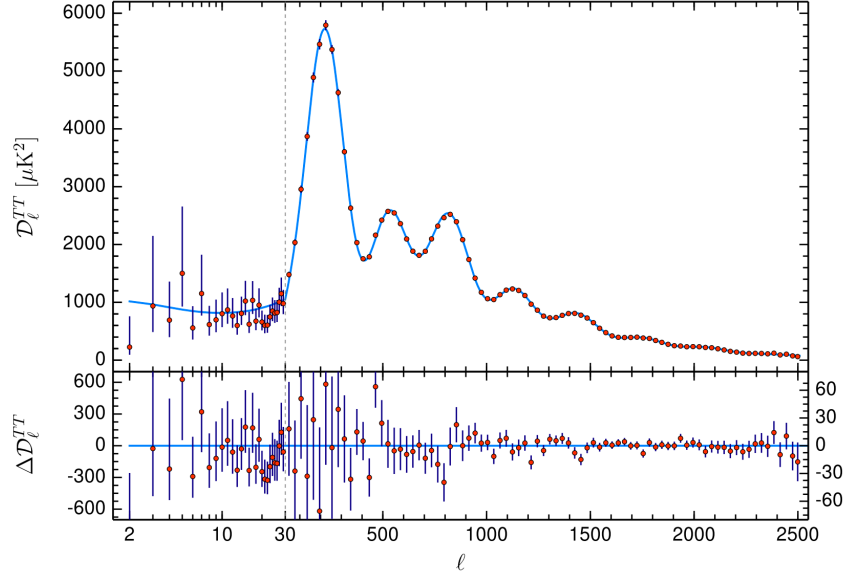


Figure 7: The angular power spectrum from Planck 2018 results [23]

third peak that is similar or larger than a second peak indicates that the matter content at the time of recombination was dominated by dark matter. A useful demonstration of the effect of baryons and total matter on the angular power spectrum is shown in Figure 8.

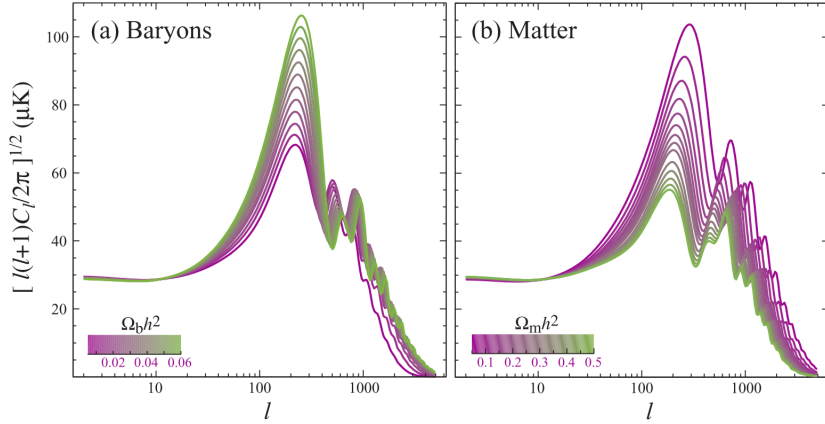


Figure 8: The effect of baryons (left) and total matter (right) on the magnitude and location of CMB angular power spectrum peaks. [22]

The measure of the dark matter content and baryon content of today's universe can be extrapolated from fitting the CMB angular power spec-

trum as in Figure 8. The results from the Planck 2018 angular power spectrum ([23]) are:

$$\Omega_{cdm} = 0.2696 \pm 0.0047 \quad (3)$$

$$\Omega_b = 0.0495 \pm 0.0005 \quad (4)$$

Each  $\Omega_x$  represents the fraction of today's mass-energy density comprised by constituent  $x$ . These values do not add to one because a large fraction of the mass-energy density of the universe is comprised of dark energy, which we have left discussion of until now.

## 2.3 STANDARD MODELS

Thus far we have focused only on the astrophysical evidence for particle **CDM**. **CDM** plays a central role in the standard model of cosmology, known as  $\Lambda$ **CDM** ("Lambda" - **CDM**). In this section, we briefly summarize the standard models of cosmology and particle physics.

### 2.3.1 THE STANDARD COSMOLOGY

The standard  $\Lambda$ **CDM** cosmology is

### 2.3.2 THE STANDARD MODEL OF PARTICLE PHYSICS

The Standard Model (**SM**) of particle physics describes all the currently known matter particles and force carrier particles, which can also have mass, and which dictate interactions between the matter particles. As of 2012, it also includes a mass generation mechanism from the Higgs boson. The **SM** is formulated using the principles of Quantum Field Theory, where symmetries in the Lagrangian give rise to conserved physical quantities and thereby determine the rules for interactions.

The known particles of the **SM** are shown in Figure 9, along with a theoretical force carrier for gravity, the graviton. These particles are typically grouped into categories: fermions and bosons. Fermions comprise all the known matter particles and are spin- $\frac{1}{2}$  particles. Each of the fermions in Figure 9 has an anti-particle, although it is an open question whether the neutrino is its own anti-particle. The integer-spin bosons, excepting the Higgs boson, which provides a mechanism for giving mass to all the other particles, are the force carriers of the standard model. The spin-1

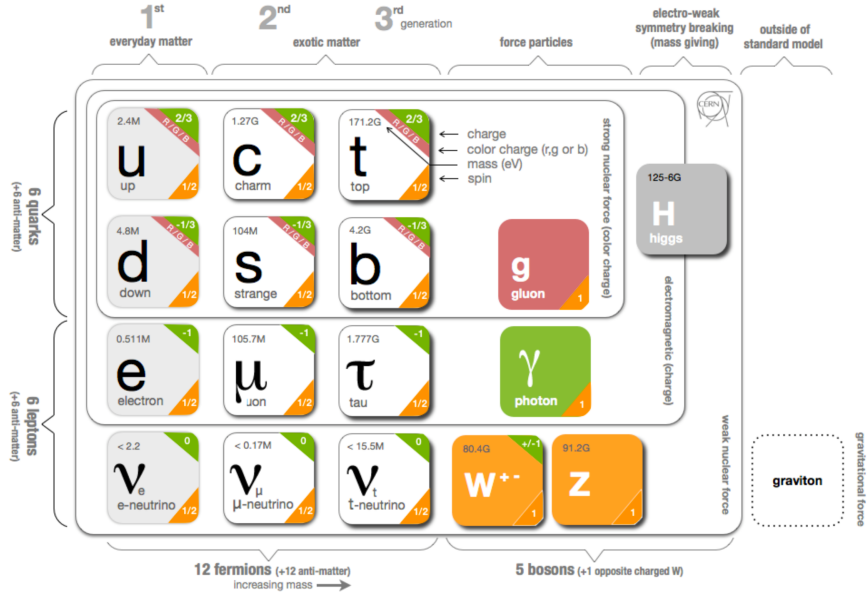


Figure 9: The particles that comprise the standard model of particle physics, including names, spins, masses, and charges. It is also indicated which fermions interact with which bosons, e.g. gluons interact with the quarks but not with the leptons.

bosons: the gluon, photon, and  $W$  and  $Z$  boson, describe three of the four forces known to physics. The gluon mediates the strong force, which governs interactions between quarks, binding them in hadrons (three quark states which make up e.g. protons and neutrons) and mesons (two-quark states such as pions). The photon mediates electromagnetism, governing interactions between particles with electric charge. The  $W^+$ ,  $W^-$ , and  $Z$  bosons mediate the weak force, which includes phenomena such as beta-decay and neutrino-electron scattering.

It was once proposed that the  $Z$  boson could mediate the interaction between **DM!** (**DM!**) and **SM**, because a **DM!** particle that interacts via the weak force fits the **WIMP** paradigm discussed below. However, direct detection experiments have long excluded such scattering cross sections, of  $10^{-39} \text{ cm}^2$ . Naively, it is possible for neutrinos, which interact weakly and have mass, to be **CDM**. However, neutrinos were relativistic during structure formation so could not perform the role of necessary of **CDM**. Estimates of the density of today's relic neutrinos show that they  $\Omega_v \approx (1.2 - 2.2) \times 10^{-3} \ll \Omega_{cdm}$  [24], [25]. The standard model, as it is known today, contains no particles that could be **CDM**.

## 2.4 DARK MATTER CANDIDATES MOTIVATED BY PARTICLE PHYSICS

Cosmology, while providing very precise measurements of the dark matter content of the universe, essentially requires only three things of dark matter candidates: (1) the candidate, *en masse*, must account for the observed  $\Omega_{cdm}$ , (2) at least 95% of it is non-relativistic or “cold” [**something**], (3) it is not strongly self-interacting (“collisionless”) or strongly interacting with baryons. Requirement (1) is fairly loose, as it is possible for multiple different dark matter particles to comprise together  $\Omega_{cdm}$ , but note that implies the dark matter candidate(s) must be stable on the timescale of the universe. This section briefly summarizes two very different dark matter candidates, which have additional motivation due to open questions from the standard model.

### 2.4.1 WIMPS AND THE HIERARCHY PROBLEM

Any system that describes particle interactions today at “low energy”, should also scale to describe particle interactions at different times (and therefore energies) in the history of our universe, namely immediately after the Big Bang in a time known as the Planck epoch. During the Planck epoch, energies were at the Planck scale of  $10^{19}$  GeV, and gravitational interactions become as large as the other forces. Any sound quantum theory should be able to account for gravitational interactions at this energy scale. However, the highest energies described by the **SM** is the known as the electroweak scale, when electromagnetism and the weak force unify. The breaking of the electroweak symmetry is done by the Higgs mechanism, which provides mass. There is a compelling argument that the strong and electroweak forces unify at energies referred to as the **GUT!** scale, and that this theory then unifies with gravity at the Planck scale (sometimes called “Theory of Everything”). The 16 orders of magnitude between the Planck scale and the electroweak scale is known as the Hierarchy Problem; there must be new physics between the electroweak scale and the Planck scale, i.e new particles with  $m > m_{Higgs}$  and new symmetries, to properly describe particle interactions during the history of our universe.

In order to solve the Hierarchy Problem, a framework known as Supersymmetry (**SUSY**) was developed. In **SUSY** each **SM** particle has a “superpartner.” In general, the superpartners have a spectrum of masses higher than **SM** particles and a symmetry called *R*-parity partitions and limits interactions between **SM** and **SUSY**. The lightest of the **SUSY** particles, called the **LSP**, can be stable. If the **LSP** neutrally charged it is a dark matter candidate.

The **WIMP** paradigm has its roots in the mathematical coincidence called the **WIMP** Miracle. If one assumes a weak-scale coupling and mass for dark matter, it naturally produces the entire  $\Omega_{cdm}$  observed today via thermal freezeout. When universe was small and dense with particles, a **WIMP**,  $\chi$ , would meet its antiparticle  $\bar{\chi}$  and annihilate into lighter particles:  $\chi\bar{\chi} \rightarrow l\bar{l}$ . The reverse reaction to produce the heavier **WIMP** ( $l\bar{l} \rightarrow \chi\bar{\chi}$ ) proceeds as long as the energies of the particle is sufficiently high, i.e.  $T > m_\chi$ . When this condition is met, the number density  $n$  of **WIMPs** is at its thermal equilibrium value  $n_{eq}$ . As the universe expands, the reaction falls out of thermal equilibrium. Both directions of the reaction ( $\chi\bar{\chi} \rightleftharpoons l\bar{l}$ ) are affected: the reverse reaction cannot produce more  $\chi$  due to cooling, and the forward reaction stalls because annihilation rate  $\Gamma_A$  relies on a sufficiently high number density  $n$ , such that the probability of  $\chi$  to meet  $\bar{\chi}$  is large. The number density of **WIMPs** become frozen into a relic density that we can observe today when the Hubble expansion rate overcame the annihilation rate:

$$\begin{aligned} H(t) &> \Gamma_A \\ &> n_\chi \langle \sigma_A v \rangle \end{aligned} \tag{5}$$

where  $\langle \sigma_A v \rangle$  is the thermally averaged annihilation cross section. The time when  $H(t) = \Gamma_A$  is referred to as freezeout. Following [26], the time evolution of the number density is described by the Boltzmann equation (see Figure 10 (left) for number density evolution before and after freezeout):

$$\frac{dn}{dt} = -3Hn - \langle \sigma_A v \rangle (n^2 - n_{eq}^2) \tag{6}$$

This equation must be solved numerically (a more complete analysis can be found in [27]), but making a few assumptions, [26] finds:

$$\begin{aligned} \Omega_\chi &\sim \frac{m_\chi T_0^3}{\rho_c} \frac{n_f}{T_f} \\ &\propto [\text{constants}] \langle \sigma_A v \rangle^{-1} \end{aligned} \tag{7}$$

Where  $\rho_c$  is the critical density,  $f$  subscripts refer to freezeout and 0 subscripts refer to today's values.  $\Omega_\chi$  then depends only depends on the particular annihilation cross section, which is set by the mass scale  $m_\chi$ :

$$\sigma_A v = k \frac{g_{weak}^4}{16\pi^2 m_\chi^2} (1 \text{ or } v^2) \tag{8}$$

Where  $v^2$  is present or absent for S- or P-wave annihilation and  $k \sim \frac{1}{2} - 2$  parameterizes the deviation of  $g$  from  $g_{weak} \approx 0.065$ . If the mass of the dark matter particle is in the range  $m_\chi \sim 100$  GeV-1 TeV, then  $\Omega_\chi$  accounts for 100% of today's observed  $\Omega_{cdm}$ . This is the **WIMP** miracle: weak-scale particles can account for *all* the dark matter content. Even the **WIMP** mass  $m_\chi$  deviates from this perfect situation, the particle can still make up a substantial percentage of dark matter (see Figure 10 (right)),

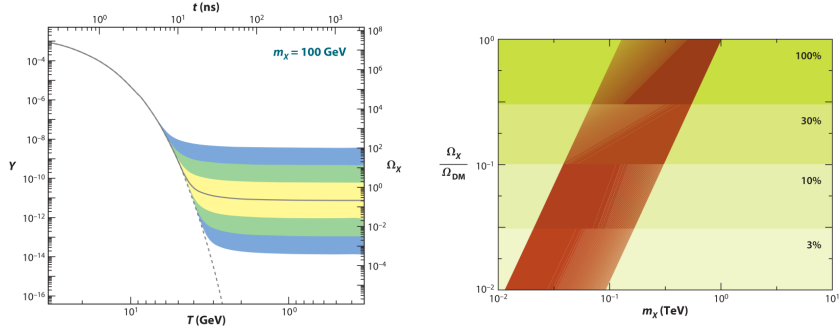


Figure 10: (left) The co-moving number density  $Y$  (left y-axis) resulting in the thermal relic density  $\Omega_\chi$  (right y-axis) for a dark matter particle of mass  $m_\chi = 100$  GeV. The solid black line is the annihilation cross section which yields the correct relic density and bands indicate cross sections that differ by successive factors of 10 from the “correct” annihilation cross section (right) A band of natural values for a thermal relic  $\chi$  that composes different percentages of the observed dark matter content. The width of the band is set by the deviation of  $g$  from  $g_{weak}$  in Equation 8, Figures from [26]

A particle with the exact mass and weak-scale coupling, i.e the Z-boson has been ruled out by direct detection experiments, but various **SUSY** parameter regions remain. The **LSP** can be a **WIMP**, and thereby it could solve two mysteries of physics: the hierarchy problem, and dark matter.

#### 2.4.2 AXIONS AND THE STRONG CP PROBLEM

The **SM** includes a term in the quark sector that should contribute to CP-violating, flavor-conserving, observables that scale with a mixing angle  $\theta_3$ . An excellent example of such an observable is the electric dipole moment of the neutron,  $d_e$ . For natural values of  $\theta_3 \sim 1$ , one would expect  $d_e \sim 10^{-16}$  e cm. However, such a dipole moment has never been observed and current experimental limits constrain  $d_e < 2.9 \times 10^{-26}$  e cm [26]. To account for this,  $\theta_3$  must be ‘fine tuned’ to  $\theta_3 \rightarrow \theta_3 10^{-10}$ . This is known as the Strong-CP Problem: we expect CP-violating observables from the **SM**, but instead we find that CP is strongly conserved.

## 2.5 MOTIVATION FOR LIPS

Chapter 5 of this thesis details a search for LIPs, here the theoretical underpinning of such a particle is discussed.

## 2.6 EXPERIMENTAL STRATEGIES FOR DETECTING DARK MATTER

2.6.1 PRODUCTION

2.6.2 INDIRECT DETECTION

2.6.3 DIRECT DETECTION

# 3

## PARTICLE DETECTION WITH LIQUID XENON

---

### 3.1 LIQUID XENON AS A DETECTOR MEDIUM

Liquid xenon detectors are powerful tools for rare event searches. In particular, the dual phase [LXe TPC](#) has been very successful in accessing [WIMP](#) parameter space and currently holds the worlds most sensitive limits on [WIMPs](#). This section describes the properties of [LXe](#) and the basic principles of [TPCs](#) that have allowed this technology to play a large role in the hunt for dark matter.

#### 3.1.1 PROPERTIES OF LIQUID XENON

Liquid xenon has many properties relevant to particle detection, particle identification, and also many properties related to the ease of detector operation:

- The density of [LXe](#) is 2.9 g/cm<sup>3</sup> at 170 K, much denser than other possible [TPC](#) target materials, such as liquid argon which has density 1.4 g/cm<sup>3</sup> at 87 K. The advantage in this two-fold: (1) the same volume contains more kg of Xe than Ar, so for two detectors of the same volume, one filled with Xe and the other with Ar, both running for one year, the Xe detector has more exposure; (2) xenon's high density effectively stops external radiation, producing an ultra-low-background volume in the center of the detector where rare-event searches can be performed (this region is called the "fiducial volume").
- Xenon gas is easily liquefied with liquid nitrogen (77 K) or commercially available pulse tube refrigerators.
- Xenon has no long-lived radioisotopes that cause troublesome backgrounds. The one exception is the  $2\nu\beta\beta$  decay of  $^{136}\text{Xe}$  (natural abundance 8.875%) with measured half-life of  $2.1 \times 10^{21}$  years. The long half-life and relatively low abundance together result in a very low count rate, and the isotope can be used to search for neutrino-less double beta decay ( $0\nu\beta\beta$ ).

- Xenon, as a noble element, is easily purified with a heated getter to rid electronegative impurities. Some of these impurities absorb xenon scintillation light, e.g. N<sub>2</sub>, and others can attract electrons, interfering with the ionization signal in TPCs, e.g. O<sub>2</sub>.
- The comparatively large mass of xenon allows it to be purified of other noble gasses via gas chromatography [28] and cryogenic distillation [29]. As other noble gasses cannot be removed via getter, this feature is extremely useful in removing the troublesome background of <sup>85</sup>Kr decay. <sup>85</sup>Kr decays via beta emission to stable <sup>85</sup>Rb with a half-life of 10.8 years and  $Q_\beta = 687$  keV. The decay proceeds directly to the <sup>85</sup>Rb ground state with a branching ratio of 99.6%. Since no de-excitation of <sup>85</sup>Rb follows, this beta decay cannot be rejected as background by coincidence with a gamma, and relies purely on the ability to discriminate between WIMP-like NR and beta- or gamma- produced ER. While ER/NR discrimination is one of the features of LXe TPCs (described in section 3.3.1.1), leakage of ER events into the NR signal region can occur and the best mitigation is to remove as much of the <sup>85</sup>Kr as possible. Single-phase LXe detectors, with no ER/NR discrimination, benefit greatly from the ability to remove <sup>85</sup>Kr.
- Particles interacting in LXe excite atoms and create electron ion-pairs, producing detectable quanta: scintillation photons and ionization electrons, respectively (described in section 3.1.2).
- Xenon produces scintillation light of wavelength  $\lambda = 178$  nm (described in section 3.1.2). Xenon is transparent to this wavelength so it can propagate freely and be directly detected with current Photomultiplier Tube (PMT) technology, and doesn't require the use of e.g wavelength shifter.
- Ionization electrons produced in particle interactions can be drifted and extracted into a gaseous region via applied electric fields, where they undergo proportional scintillation. By this method, a single electron is amplified many-fold into detectable photons. This basic operating principle of dual-phase TPCs makes even a single ionization electron detectable.
- Xenon has high light and charge yields, and therefore a low threshold for producing detectable quanta. A useful quantity is the so-called ‘W-value’ of LXe:  $W = 13.7 \pm 0.2$  eV [30]. The W-value, analogous to a work-function, is a measure of the average energy expenditure to produce one quanta (scintillation photon or an ionization electron) from liquid xenon.

- LXe TPCs are easily scalable: creating a large homogenous volume is straightforward. In contrast, solid state detectors, such as cryogenic Ge, are more difficult to scale up directly and require instead the production of multiple small modules ( $O(10)$  cm) which each must be instrumented separately.

### 3.1.2 SCINTILLATION AND IONIZATION SIGNAL GENERATION

A particle can interact with a xenon atom through interaction with an orbiting electron, creating an ER, or though an interaction with the xenon nucleus, where the nucleus is imparted with momentum and recoils, NR. Some energy is lost to atomic motion (heat). The recoiling electron or nucleus loses energy via interaction with neighboring xenon atoms, creating more excited atoms and electron-ion pairs. The excited xenon atoms,  $Xe^*$ , combine with other atoms to form an excited dimer, or excitons,  $Xe_2^*$ . The excited dimer forms two states: a triplet and a singlet, which de-excite with the emission of a 178 nm photon. The lifetimes of the triplet and singlet are measured to be 24 ns and 3 ns, respectively [31]. Since the scintillation light is produced by the excimer, which has a different electronic structure than atomic xenon, the light is free to propagate through the detector and will not be absorbed by the atomic xenon. The  $Xe^+$  ions of the electron-ion pairs combine with other Xe atoms to form dimers  $Xe_2^+$ , and these dimers can combine with electrons (from the electron-ion pairs) to form excitons,  $Xe_2^*$ , which then decay and produce additional 178 nm scintillation photons. This process is called recombination. If no electric field is applied, all electron-ion pairs recombine to produce additional scintillation photons. If an external electric field is present, some electrons can be drifted away from the interaction site to be detected with other methods.

The sensitivity of liquid xenon detectors to low energy recoils depends on their ability to detect the 178 nm scintillation photons with high-efficiency. High Quantum Efficiency (QE) PMTs constructed with ultra-low radioactivity materials are the go-to instrument for this purpose. In addition to high-efficiency photon-detectors, liquid xenon detectors must also have high geometrical light collection efficiency to optimize sensitivity. Single-phase liquid xenon detectors, where no electric field is applied, maximize light-collection by with a spherical geometry, endeavoring to cover  $4\pi$  steradians surrounding the LXe. The XMASS detector uses spherical geometry to accomplish photocathode coverage of 62%, and two types of Hamamatsu PMTs (R10789-11 and R10789-11MOD) with QE of 28%, and quote a signal collection efficiency of 20% [32], [33]. Dual-phase TPC detectors are lined with Polytetrafluoroethylene (PTFE) to take advantage of its extremely high ( 99%) reflectivity for 178 nm light in LXe [34]. The

[LUX](#) detector uses a cylindrical geometry, with all non-light-collecting surfaces lined with [PTFE](#), and Hamamatsu R8778 [PMTs](#) ([QE](#) of 33%) only on the top and bottom of the detector (low photocathode coverage), to accomplish a light collection efficiency of 90% [35].

If the detector is a [TPC](#) the ionization electrons are drifted away from the interaction site to be detected. Single phase [TPC](#) employ thin wires to collect the ionization electrons. For example, the EXO-200 experiment is a single-phase liquid xenon [TPC](#) that uses crossed-wire planes to collect the ionization electrons and avalanche photodiodes to collect the scintillation photons [36]. [LUX](#) is a dual-phase xenon [TPC](#), where ionization electrons produced in the large liquid region are drifted and extracted into gaseous xenon via applied electric fields, where they undergo proportional scintillation. The proportional scintillation light is the same 178 nm wavelength as scintillation in the liquid produced in the liquid, and it is similarly collected via high [QE PMTs](#).

In addition to light-collection efficiency, the sensitivity of [TPC](#) xenon detectors also depends on their ability to collect signal from the ionization electrons. There are challenges in delivering High Voltage ([HV](#)) to liquid xenon in order to set up the electric field which drifts the ionization electrons (some of these challenges are explained in Chapter 6). Additionally, electronegative impurities such as oxygen ( $O_2$ ) present in the detector attract and capture ionization electrons as they drift, eating away the ionization signal. These non-noble impurities are removed by constantly circulating the xenon through a heated zirconium getter and returning it to the detection volume. Purification through a getter must be done in gaseous phase, so liquid xenon removed from the detection volume is evaporated, passed through the getter via a circulation system, and re-condensed into the detection volume.

## 3.2 DUAL-PHASE XENON TIME PROJECTION CHAMBER

A particle interacting in a noble liquid or gas target deposits energy into scintillation and ionization channels (Section 3.1.2). The basic operating principle of [TPCs](#) is to drift the ionization electrons away from the interaction site and detect them at a later time than the scintillation signal is detected. A dual phase liquid xenon [TPC](#) is a type of [TPC](#) with a large liquid target volume and a small region of xenon vapor above the liquid volume, instrumented with light sensors (typically [PMTs](#)). A particle interacting in the liquid target produces both scintillation photons and ionization electrons at the interaction site. The scintillation photons are promptly detected by the [PMTs](#), this primary signal is called S1. The ionization elec-

trons are drifted upward to the gas region by an applied electric field, and extracted across the liquid-gas boundary by a higher electric field, where they undergo proportional scintillation and produce a second signal detected by the PMTs, called S2. The field is supplied by a series of electrodes, composed of wire planes, grids, or chemically etched meshes, held at constant voltages. The bottom-most field-producing electrode is called the cathode, at the top of the liquid region is the gate or extraction electrode, followed O(1) cm by the anode. The liquid region is often referred to as the ‘drift region’ and region between the gate and anode is referred to as the ‘extraction region’. The drift region takes up by far more volume than the extraction region. The electrons are extracted from liquid to gas with some efficiency, called the Electron Extraction Efficiency (EEE). This efficiency plays an important role in the operation of dual-phase LXe TPCs, and is discussed further in **E-Train CHAPTER**.

The S2 in a dual-phase TPC plays two important roles: (i) internal amplification of the signal, whereby a few electrons are transformed into O(10) times as many photons (ii) ( $x, y$ ) localization via PMT hit pattern. The time spacing of the S1 and S2 signals can be converted to depth ( $z$ ) of the interaction, providing full ( $x, y, z$ )-reconstruction of the interaction position.

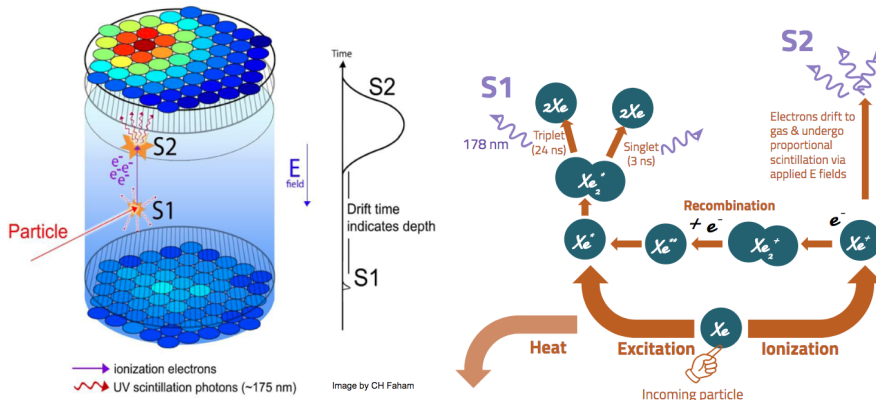


Figure 11: (left) Diagram of a dual-phase xenon time projection chamber. The time difference between S1 and S2 gives the depth ( $z$ ) of the interaction, and ( $x, y$ ) is reconstructed from the S2 signal. (right) Diagram summarizing the generation of the scintillation and ionization signal generation in dual-phase xenon time projection chambers.

### 3.2.1 ENERGY RECONSTRUCTION

Energy reconstruction in dual-phase xenon TPCs comes from the measurable quantities, S1 and S2, but begins with the number of excitons  $n_{ex}$  and electron-ions pairs  $n_i$  generated at the interaction site.

$$E = fW(n_{ex} + n_i) \quad (9)$$

where  $E$  is the deposited energy.  $W$  is the average energy needed to produce a single excited or ionized atom,  $W = 13.7 \pm 0.2$  eV [31]. The quenching factor,  $f$  is 1 for electronic recoils but  $f \neq 1$  for nuclear recoils. For now, take the case of electronic recoils and set  $f = 1$ . This equation can be rewritten:

$$E_{ER} = W\left(1 + \frac{n_{ex}}{n_i}\right)n_i \quad (10)$$

The ratio of excitons to ions is constant for electron recoils  $n_{ex}/n_i = 0.2$  [37]. As discussed in Section 3.1.2, each exciton deexcites, emitting a 178 nm photon, some fraction  $r$  of the initial electron-ion pairs recombine and form additional excitons. The total number of prompt scintillation photons created by the interaction is then:

$$n_\gamma = \left(r + \frac{n_{ex}}{n_i}\right)n_i \quad (11)$$

And the total number of electrons created by interaction site (electrons escaping recombination) is:

$$n_e = (1 - r)n_i \quad (12)$$

Thus, the effect of recombination is to “trade-out” electrons for photons, but the total number of quanta is conserved (Figure 12 (left)). The amount of recombination depends on applied electric field, LXe density, and particle energy [37]. In the case of the 122 keV electron recoils in Figure 12 (right): at low fields, most of the electron-ion pairs recombine, which results in more scintillation photons. As the applied electric field increases, more electrons are pulled away from the interaction site resulting in fewer scintillation photons and more ionization electrons. These amounts of photons and electrons are referred to as the scintillation and ionization yields. The two quantities,  $n_\gamma$  and  $n_e$  relate directly to the observable S1 and S2 signals:

$$\begin{aligned} E_{ER} &= W(n_\gamma + n_e) \\ &= W\left(\frac{S1}{g_1} + \frac{S2}{g_2}\right) \end{aligned} \quad (13)$$

where  $E_{ER}$  reminds us that we are taking the case of electronic recoils and set  $f = 1$  in Equation 13.  $S1$  and  $S2$  are in units of detected photons (phd) or photoelectrons (phe), and  $g_1$  and  $g_2$  are detector gains in units of phd / quanta or phe / quanta<sup>1</sup>.  $g_1$  is the detection efficiency for the prompt scintillation photons: it is a product of the the average geometrical light collection efficiency and the average PMT QE. Typical values for  $g_1$  are in the range of 0.01-0.02.  $g_2$  is the analogous quantity for  $S2$  proportional scintillation light: it is a product of the EEE and the average number of detected photons produced by one extracted electron. Typical values for  $g_2$  are in the range 10-60.

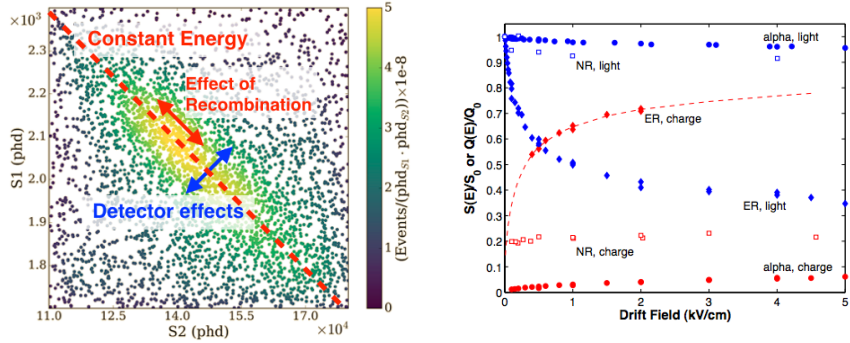


Figure 12: (left) Plot illustrating the effect of recombination and detector effects on a line source ( $^{127}\text{Xe}$ ), courtesy of E. Pease. (right) Field dependence of scintillation and ionization yield in LXe for 122 keV electron recoils (ER), 56.5 keV nuclear recoils (NR) and 5.5 MeV alphas, relative to the yield with no drift field from [40]

To properly reconstruct the energy of nuclear recoils, we must revisit the quenching factor factor  $f$ . Equation 13 then becomes:

$$\begin{aligned} E_{NR} &= fW(n_\gamma + n_e) \\ &= fW\left(\frac{S1}{g_1} + \frac{S2}{g_2}\right) \end{aligned} \tag{14}$$

This equation can be rewritten:

$$E_{NR} = fE_{ER} = \frac{E_{ER}}{\mathcal{L}} \tag{15}$$

---

<sup>1</sup> An distinction should be made between the traditional units of phe and the units of phd which are used in many LUX publications. The Hamamatsu R8778 PMTs used in LUX emit two photoelectrons for a single VUV photon 20% of the time [38], but the PMT gain calibration photons (from blue LEDs) do not. LUX performed additional calibration with VUV photons to account for the difference, and report detected photons instead of photoelectrons [39]

where  $\mathcal{L}$  is Lindhard's factor. Lindhard's factor accounts for the fraction of energy lost to atomic motion (heat) in nuclear recoils [41]. An incoming particle interacts with a “patient zero” Xe atom, resulting in a nuclear recoil. The patient zero Xe atom interacts with surrounding atoms in a cascade to produce S1 and S2; it is the energy partitioning in this cascade that results in different energy scales for **ER** and **NR**. Lindhard shows that the energy partitioned in nuclear interactions and electron interactions from a recoiling xenon nucleus is:

$$\mathcal{L} = \frac{kg(\epsilon)}{1 + kg(\epsilon)} \quad (16)$$

where  $k = 0.133Z^{2/3}A^{-1/2}$  is a proportionality constant that relates electronic stopping power and the velocity of the recoiling xenon atom, and  $\epsilon = 11.5(E_{NR}/\text{keV})Z^{-7/3}$ . Lindhard's calculation yields  $k = 0.166$ , which is the commonly accepted value. Measurements of nuclear recoils in **LXe** are used to fit for  $k$ . Several experiments were compared by Sorensen and Dahl to determine that nuclear recoil energy is well described by  $0.110 < k < 0.166$  [42]. Results from **LUX** yielded  $k = 0.1735 \pm 0.0060$  [**LUX:DD**].

If it is not known *a priori* whether an interaction is a nuclear recoil or electron recoil, the ‘electron equivalent’ energy is given in units  $\text{keV}_{ee}$ . If it is known that the recoil is a nuclear recoil, Lindhard’s factor is applied and the units can be given in  $\text{keV}_{nr}$ . Lindhard’s factor allows us to combine nuclear recoils and electronic recoils on one energy scale by labelling contours of constant reconstructed energy with both  $\text{keV}_{ee}$  and  $\text{keV}_{nr}$  (example in Figure 13).

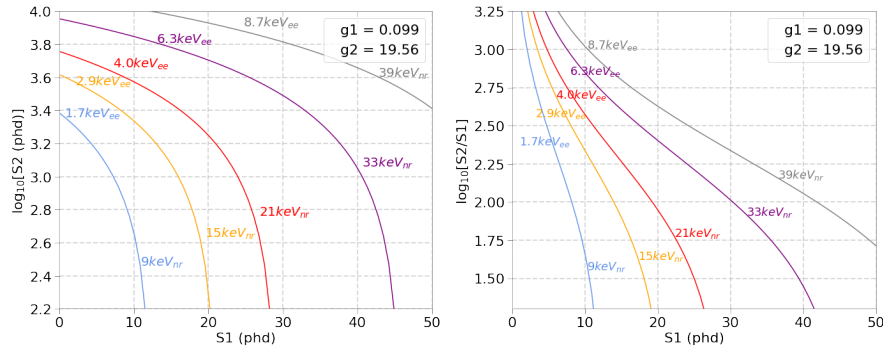


Figure 13: Plots showing combined energy contours in two common sets of axis units, for an example set of  $g_1$  and  $g_2$ .

### 3.3 DUAL-PHASE XENON TPCS FOR DARK MATTER DETECTION

Dual phase Xe TPCs have been at the forefront of the hunt for dark matter in the last several decades. As described above, the xenon medium and detector technology make excellent low-background, rare-event searches with high signal yields. Dual phase Xe TPCs also provide a few enhancements to WIMP dark matter searches, but other dark matter or rare event searches are also possible with the same detector.

#### 3.3.1 WIMP SEARCHES WITH LXE TPCS

Dual-phase LXe TPCs are optimized for WIMP searches. They have been very successful in reaching large areas of WIMP parameter space.

##### 3.3.1.1 ER, NR DISCRIMINATION

One of the most powerful features of LXe TPCs, which has made the technology especially useful in the hunt for WIMP dark matter, is the ability to discriminate between electron recoils and nuclear recoils. WIMP interactions are expected to be nuclear recoils, but most natural radioactivity ( $\beta, \gamma$ ) are electron recoils. The amount of recombination for equal energy ER and NR is different, so for events with the same reconstructed energy  $E(\text{keV}_{ee})$ , the ratio of S2/S1 is characteristically different. A useful discrimination space is  $\log_{10}(\text{S2}/\text{S1})$  vs S1, as the distributions of  $\log_{10}(\text{S2}/\text{S1})$  for ER and NR events are Gaussian. Different calibration sources are used to develop a population of events known to be ER and a population of events known to be NR, these calibration sources reveal what is known as the ER and NR bands (Figure 14).

In the course of a WIMP search, the experimentalists are tasked with keeping a stable detector operating for months or years. In this time, the detector will see events of natural radioactivity and perhaps WIMPs. The natural radioactivity appears in the ER band (location of bands is known from calibration), and nuclear recoil events appear in the NR band. Due to band overlap, only events appearing below the NR mean are considered WIMP candidates. This restriction cuts signal acceptance to 50%, but allows dual-phase TPCs to reject background electronic recoils at  $\gtrsim 99\%$ . The background acceptance rate is known as ER leakage. It is the fraction of events appearing below the NR mean from the ER calibration source. For a background rejection rate of 99.99%, the ER leakage is 0.01%, this number determines the sensitivity of the detector.

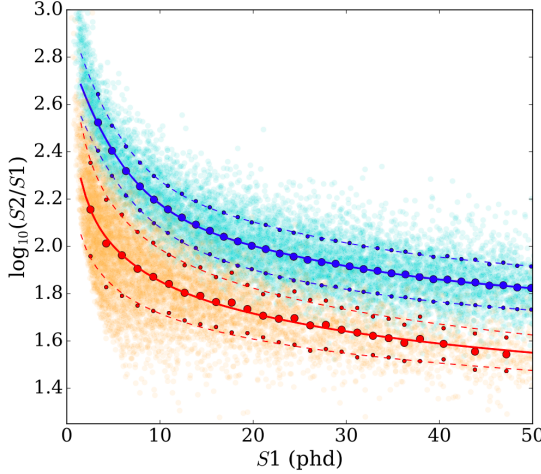


Figure 14: Plot showing ER and NR bands from LUX. Solid lines are the ER and NR Gaussian means  $\mu$ , dotted lines are  $\mu \pm 1\sigma$ . Figure from [37]

### 3.3.1.2 WIMP RATES AND CROSS SECTION

The choice of direct detection for **WIMP** searches was touched on ???. Here, we go through the specifics of **WIMP** rates and their cross section in **LXe**, showing that the **LXe TPC** technology gets an enhancement that makes it especially suited for **WIMP** searches.

**WIMPs** scattering in the **TPC** produce measurable nuclear recoils. The shape of this nuclear recoil spectrum determines eventually the number of **WIMP** events observed, and it depends on both **WIMP** properties and detector properties. The energy imparted to nucleus depends on **WIMP** mass  $M_\chi$  and velocity distribution, as well as the mass of the target nucleus  $M_T$  and a nuclear form factor  $F$  that governs how effectively energy is transferred to the nucleus. Assuming a uniform, spherical dark matter halo, estimates for the local density of dark matter  $\rho_\chi$  can be made from astrophysical observations. The velocity distribution  $f(v)$  is assumed to be isotropic and Maxwellian, with a cut-off at the escape velocity  $v_{esc}$  of the Milky Way. If we account for the velocity of the Earth through the galactic plane  $v_E$ , the velocity distribution is shifted:  $f(v) = f(v, v_E)$ . Following Lewin and Smith [43], we can write the local number density:

$$\begin{aligned} dn &= \frac{n_0}{k} f(v, v_E) d^3v \\ &= \frac{n_0}{k} \exp\left(-\frac{(v + v_E)^2}{v_0^2}\right) d^3v \end{aligned} \tag{17}$$

Where  $n_0 = p_\chi/M_\chi$  is the average local number density of dark matter particles,  $v_0 \approx 220 \text{ km/s}$  [?] is the mean of the dark matter velocity dis-

tribution, and  $k$  is a normalization constant such that  $\int_0^{v_{esc}} \equiv n_0$ . If the escape velocity is infinite, the normalization integral is easily evaluated:

$$k = \int_0^{2\pi} \int_{-1}^{1i} d(\cos\theta) \int_0^{\infty} f(v, v_E) v^2 dv = (\pi v_0^2)^{3/2} \equiv k_0 \quad (18)$$

$v_{esc}$  is not infinite ( $v_{esc} \approx 544 \text{ km/s}$  [44]), and so the normalization integral evaluates to:

$$k = k_0 \left[ \operatorname{erf}\left(\frac{v_{esc}}{v_0}\right) - \frac{2}{\pi^{1/2}} \frac{v_{esc}}{v_0} \exp(-v_{esc}^2/v_0^2) \right] \equiv k_1 \quad (19)$$

Although this is a more complicated expression, it should be noted the difference between  $k_0$  and  $k_1$  is less than 0.5%. We now have a full picture of the local number density of dark matter, and we focus on the scattering rate in the detector. If we let  $\sigma$  be the scattering cross-section per nucleus (the details of  $\sigma$  are discussed later), the event rate per unit mass detector with target mass  $M_T$  is:

$$dR = \frac{1}{M_T} \sigma v dn \quad (20)$$

The experimentalist is concerned with the observable recoil energy spectrum produced by such a dark matter rate. A **WIMP** of mass  $M_\chi$  and initial energy  $E_\chi = \frac{1}{2} M_\chi v^2$  scattering at angle  $\theta$  (in the center-of-mass frame) will impart a recoil energy  $E_R$  to a target nucleus of  $M_T$

$$E_R = r E_\chi \frac{1 - \cos\theta}{2} \quad (21)$$

Where  $r$  is the kinematic factor:

$$r = \frac{4M_\chi M_T}{(M_\chi + M_T)^2} \quad (22)$$

Note that the kinematic factor indicates that recoil energies are greatest for  $M_\chi \approx M_T$ . SUSY models favor **WIMP** masses in the range 100GeV-1000GeV (Figure 16), which makes xenon ( $M_{Xe} \approx 123 \text{ GeV}$ ) an excellent target. **WIMP** scatters are assumed to be isotropic, so recoil energies are distributed uniformly in the range  $0 < E_R < rE_\chi$  (i.e. Equation 21 for  $0 < \cos\theta < 1$ ). We can put this together with Equation 20 to arrive at an differential rate per recoil energy in the detector – i.e. the observable recoil spectrum for **WIMP**-nucleus scattering. Note that equation Equation 20 is in terms of the **WIMP** velocity  $v$  and Equation 21 is in terms of

[WIMP](#) energy  $E_\chi = \frac{1}{2}M_\chi v^2$ , so a change of variables is required. After the variable change, we can write:

$$\frac{dR}{dE_R} = \frac{\rho_\chi}{M_\chi} \frac{\sigma}{k} \left( \frac{M_T + M_\chi}{M_T M_\chi} \right)^2 \int_{v_{min}}^{v_{max}} \frac{1}{v} f(v, v_E) d^3 v \quad (23)$$

Until now, we have left off discussion of the [WIMP](#)-nucleus cross section  $\sigma$ . Equation 23, as it stands is the [WIMP](#) spectrum in the limit of billiard-ball coherent scattering. In reality, nucleus has structure which must be accounted for, which is accomplished with a nuclear form factor  $F = F(q)$ . In addition, the cross-section is split into spin-independent ( $\sigma_{SI}$ ) and spin-dependent ( $\sigma_{SD}$ ) components:

$$\sigma = \sigma_{SI} F_{SI}^2(q) + \sigma_{SD} F_{SD}^2(q) \quad (24)$$

The nuclear form factor,  $F(q)_{SI,SD}$ , decreases the cross section at higher momentum transfer. The two coherent terms  $\sigma_{SI}$  and  $\sigma_{SD}$  are parametrized as follows:

$$\begin{aligned} \sigma_{SI} &= \frac{4\mu^2}{\pi} [(A - Z)f_n + Zf_p]^2 \\ &\approx \frac{4\mu^2 A^2}{\pi} f_n^2 \end{aligned} \quad (25)$$

Where  $\mu$  is the usual reduced mass, and the second line takes into account that for [SUSY WIMP](#) models, the couplings to neutrons and protons are approximately equal ( $f_n \approx f_p$ ).

$$\sigma_{SD} = \frac{32G_F\mu^2}{\pi} \frac{J+1}{J} [\langle s_n \rangle a_n + \langle s_p \rangle a_p]^2 \quad (26)$$

Where  $G_F$  is the Fermi constant,  $J$  is the total nuclear spin of the target, and  $\langle s_{n,p} \rangle$  and  $a_{n,p}$  represent values for neutron and proton spins and couplings, respectively. It should be noted that  $\sigma_{SI}$  scales as  $A^2$ , which indicates a cross-section enhancement for larger targets.  $\sigma_{SD}$  lacks the  $A^2$  scaling, and is smaller  $\sigma_{SI}$ . This indicates that recoil-rates are dominated by spin-dependent interactions. The two cases are treated separately, with collaborations releasing both spin-independent and spin-dependent [WIMP](#) limits. in liquid xenon detectors, the odd-numbered nuclei  $^{129}\text{Xe}$  and  $^{131}\text{Xe}$  contribute to the spin-dependent rate. The enhancements for the [WIMP](#) recoil rate in Xe are illustrated in Figure 15

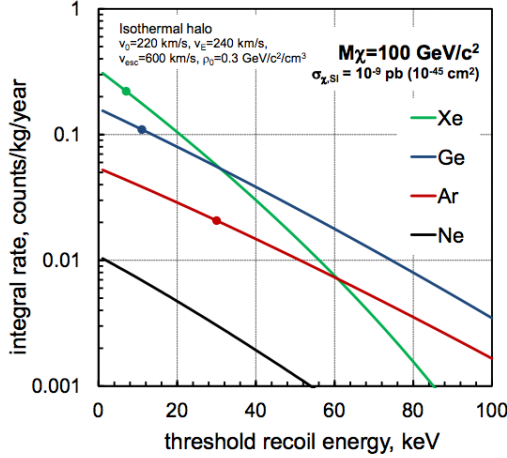


Figure 15: Plot showing spin-independent WIMP rates in common detector target materials, dots indicate typical thresholds for the targets. Xenon gains in favored SUSY parameter space ( $M_\chi \gtrsim 100$  GeV) due to a kinematic enhancement ( $M_\chi \sim M_{Xe}$ ) and a cross-section enhancement ( $\sigma_{SI} \propto A^2$ ). Figure from [45]

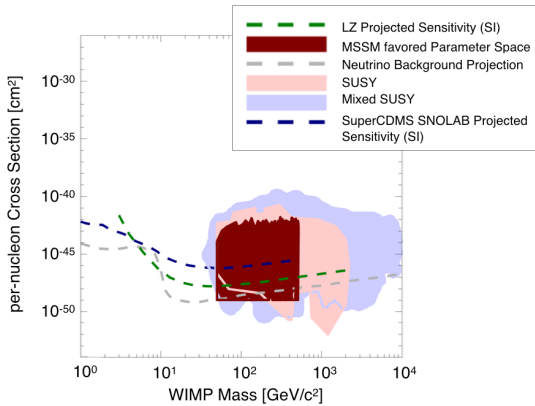


Figure 16: Projected limits of next-generation dark matter detectors and areas where SUSY models predict the presence of WIMPs. Although Xe (LZ, green dashed) performs better for WIMP parameter space, Ge and Si (SuperCDMS, blue dashed) can access other light dark matter parameter space below 10 GeV. The plot was generated by <http://dmtools.brown.edu/>

### 3.3.2 OTHER DARK MATTER SEARCHES WITH LXe TPCs

The available [SUSY](#) parameter space has dwindled greatly in the last few decades, due in large part to the success of this detector technology. Coupled with no observation of [SUSY](#) at the [LHC!](#) ([LHC!](#)), experimentalists are beginning to look to other models and parameter spaces for dark matter. New technologies are being developed and refined for new dark matter candidates, but already existing, well-understood detector technologies such as dual-phase [TPCs](#) can also be employed in the search for non-[WIMP](#) dark matter.

In their first [WIMP](#) search results, the Xenon10 collaboration imposed an analysis threshold of  $4.5 \text{ keV}_{nr}$  [46]. The first [LUX](#) results set an analysis threshold of  $4.3 \text{ keV}_{nr}$  (with  $2 < S1(\text{phd}) < 30$  and  $S2(\text{phd}) > 200$ ;  $S2(\text{electrons}) \gtrsim 8$ ) [47]. The first Xenon100 results set an analysis threshold of  $8.7 \text{ keV}_{nr}$  ( $4 < S1(\text{phe}) < 20$  and  $S2(\text{phe}) > 300$ ;  $S2(\text{electrons}) \gtrsim 10$ ) [48]. Such thresholds are common practice, and are set by the light-collection efficiency of the detector; the detection threshold is much lower. Dual-phase [TPCs](#) are sensitive to events which produce a single electron, due to the internal amplification of the  $S2$  signal; the reason for setting analysis thresholds is to ensure the presence of an  $S1$  in the event. Without both  $S1$  and  $S2$  in the event, the full  $(x,y,z)$  position cannot be reconstructed, and so a fiducial cut cannot be applied. Sorensen showed that the Xenon10  $S2$  pulse width carries a mild  $z$ -dependence [49], and so larger detectors with a long drift time may gain reliable  $z$ -position reconstruction via  $S2$  pulse width [50]. Improvements in analysis techniques such as this allow dual-phase xenon [TPCs](#) to reach lower [WIMP](#) masses, and even other dark matter models.

In 2011 the Xenon10 collaboration presented a search for low-mass (5 - 20 GeV) dark matter [51]. The detector conditions were distinct from the Xenon10 [WIMP](#) search in [46]: the secondary scintillation gain was about 12% higher, and the  $S2$ -sensitive trigger threshold was set at the level of a single electron. With this, the collaboration carried out a standard [WIMP](#) analysis (i.e one based on the procedure presented in 3.3.1.2), with a lowered  $S2$  analysis threshold of 4 electrons ( $1.4 \text{ keV}_{nr}$ ). Why they did not proceed down to the detection threshold of 1 electron is very interesting; and is discussed further in Chapter 8. Since Xenon10 is a small detector, they were not able to take advantage of  $S2$ -width  $z$ -correlations, but they employed a radial fiducial cut and other analysis techniques to produce the result in Figure 17, which also shows the Xenon10 standard [WIMP](#) analysis for comparison.

A few years later, Essig et al. used the information reported in [51] and other Xenon10 publications to produce the first direct detection limits of sub-Gev dark matter [52]. The detection threshold for [WIMPs](#) in [LXe](#)

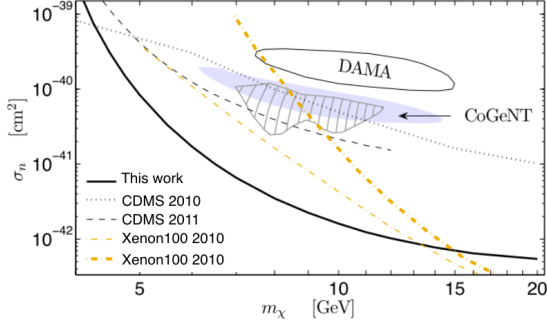


Figure 17: Xenon 10 low-mass WIMP limit extended the range of the standard WIMP result.

decreases sharply for  $M_{WIMP} \lesssim 10 \text{ GeV}$ ; however, this detection threshold is based on the assumption that the dark matter is interacting only with the xenon nucleus. If sub-GeV dark matter scatters with atomic *electrons*, as opposed to nuclei, then it can produce observable signals of a few electrons. In L<sub>Xe</sub> TPCs the S1 signal is lost due to light collection, and the few electron signals are observable as S2s. The approach in the paper is to follow approximately the same procedure as in Section 3.3.1.2, with a few but significant substitutions. The  $E_R$  in Equation 21 must now account for the binding energy of the electron, and take a different form to refer to the recoil of the electron and not the nucleus. The cross section of interest is now  $\sigma_e$ , the sum over all of the differential ionization cross sections for electrons in the (n, l) shell. For a dark photon with mass  $O(\text{MeV-GeV})$  coupled to the visible sector via kinetic mixing (a very generic class of standard model extensions discussed in Chapter ??, Essig et al. set the exclusion limit in the  $m_{DM} - \sigma_e$  plane in Figure 18 (left). If there is some momentum-transfer enhancement due to e.g. scattering through an electric-dipole moment,  $\sigma_e \rightarrow \sigma_e F_{DM}(q) \equiv \bar{\sigma}_e$ . Essig set exclusion limits for such dark matter candidates in Figure 18 (right).

In addition to the dark sector, dual-phase TPCs can search for other dark matter signals with scattering on electrons. Annual modulation searches (in ER or NR) can provide clues to dark matter. Such searches take advantage of the fact that  $v_E$  varies with the rotation of the earth around the sun, reaching a maximum in June and minimum in December. The modulation in  $v_E$  leads to a modulation in the recoil rate observed in the detector. Searches for dark matter-induced rate modulations can offer a generic approach to identify dark matter interactions, complementary to the model-driven dark matter searches. The LUX experiment did such a search, looking at ER modulations in an energy rage of interest (2-6 keV<sub>ee</sub>). This energy range was chosen to overlap with the DAMA/LIBRA Collaboration's long-standing and controversial claim of dark matter modulation

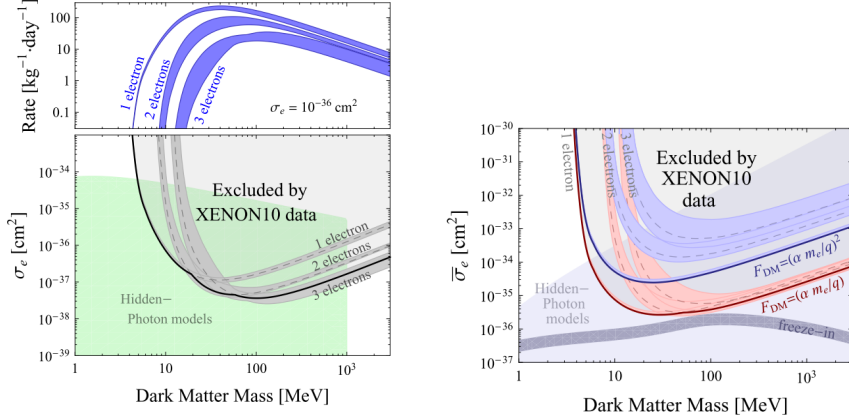


Figure 18: (left) Top: Expected 1,2,3-electron signal rates for Sub-GeV DM with  $\sigma_e = 10^{-36} \text{ cm}^2$  and Bottom: exclusion limit set with Xenon10 few-electron signals. (right) Exclusion limits for dark matter scattering through an electric-dipole moment (red) and through a very light ( $\ll$  keV) mediator (blue)

on a target of NaI(Tl), which appears strongest around a recoil energy of 3 keV<sub>ee</sub>. LUX found no significant indication of rate modulation [53]. If future large dual-phase TPCs like XenonNT and LZ observe a NR WIMP signal, the additional positive identification of a modulation signal of the NR signal would be a smoking-gun for WIMP discovery.

Another dark matter candidate that could produce an electron recoil signal in xenon is the axion (or more generally, axion-like-particles). For searches such as these, a signal model is produced from the spectrum of axions from different sources, such as galactic axions or solar axions. The resulting signal model is an ER spectrum accounts for finite detector energy resolution and threshold. The signal model spectrum is compared to the observed ER spectrum in the appropriate energy ranges, resulting in a confidence statement mass of the axion  $m_A$  and the axio-electric coupling  $g_{Ae}$ . The results of searches for solar axion and galactic axion signals are shown in Figure 19.

Finally, a model-independent search for LIPs is possible in dual-phase xenon TPC. As discussed in Chapter ??, LIPs appear in dark sector models with a masses dark photon, where another dark sector particle  $\chi$  couples to the standard model electron via kinetic mixing of the dark photon and standard model photon. LIPs deposit energies that can be described with particles of effective fractional charge. Chapter 5 describes the signal model and analysis method to search for LIPs in LUX.

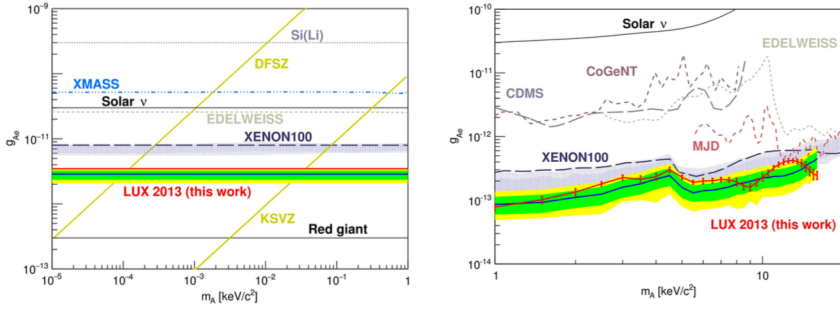


Figure 19: (left) Recent limits on solar axion coupling and mass (right) recent limits on galactic axion coupling and mass. Figure taken from [54].

## PART II

### BIG SCIENCE

This section describes research done with the LUX Detector.

# 4

## THE LUX DETECTOR

---

### 4.1 LUX OVERVIEW

The [LUX](#) detector was an ultra-low background dual-phase liquid xenon TPC that set world-leading limits on [WIMP](#) interactions.

[LUX](#) began underground commissioning in July 2012, moving to the 4850 level (4300 m.w.e) of Sanford Underground Research Facility ([SURF](#)) in Lead, South Dakota. The [LUX](#) Collaboration’s first [WIMP](#) search exposure was for a period of 85.3 live-days, acquired between April 2013 and August 2013. This period of time is referred to as Run03, and the [WIMP](#) result is referred to as WS2013. The detector then underwent a grid conditioning campaign to improve voltage capabilities, followed by a series of extensive calibrations to characterize the new operating conditions. The detector then ran for a period of 332 live-days from September 2014 to May 2016 (Run04, WS2014-2016), ending with decommissioning in September 2016. Run03 and Run04 had distinct operating conditions and calibrations. The [LIP](#) search in Chapter 5 was carried out using Run03 data, and the calibrations in the latter half of this chapter describe the detector conditions as they were in Run03.

### 4.2 INTERNAL COMPONENTS

The active volume of [LUX](#) was composed of 300 kg of liquid xenon, instrumented with two arrays of Hamamatsu R8778 Vacuum Ultra Violet ([VUV](#))-sensitive [PMTs](#) viewing the liquid region from the top and bottom. Both arrays were composed of 61 [PMTs](#) that detected S1 and S2 photons from particle interactions in the active liquid volume, and were held in place by copper mounting blocks. The [PMTs](#) were tightly packed in a hexagonal formation to maximize light collection. The xenon-facing surfaces of copper [PMT](#) mounting blocks were covered with [PTFE](#) tri-foils to reflect the 178 nm light, since copper is a poor reflector of [VUV](#) light.

The active region was defined by a series of strung wire or mesh grids: the cathode grid was at the bottom of the detector, and the gate grid was 48.3 cm above the cathode when cold. These two grids formed the drift

field, which was 180 kV/cm during Run03. The region is known as the drift region, it is where particle interactions occur. The anode mesh plane was 1 cm above the gate grid, and the xenon liquid level was held constant between these two electrodes by a spillover weir. The anode and gate form the extraction region of the experiment, where electrons are extracted across the liquid-gas boundary and undergo proportional scintillation to form S2. There are two additional grids, the top and bottom grids, which are placed 2 cm from the top and bottom PMT arrays to insulate the PMTs from the high fields produced by the other grids. The top and bottom grids were held at approximately the same voltage applied to the PMTs. All electrodes were 88%-99% optically transparent at normal incidence, and made of stainless steel 316. The major components of LUX are shown in Figure 20

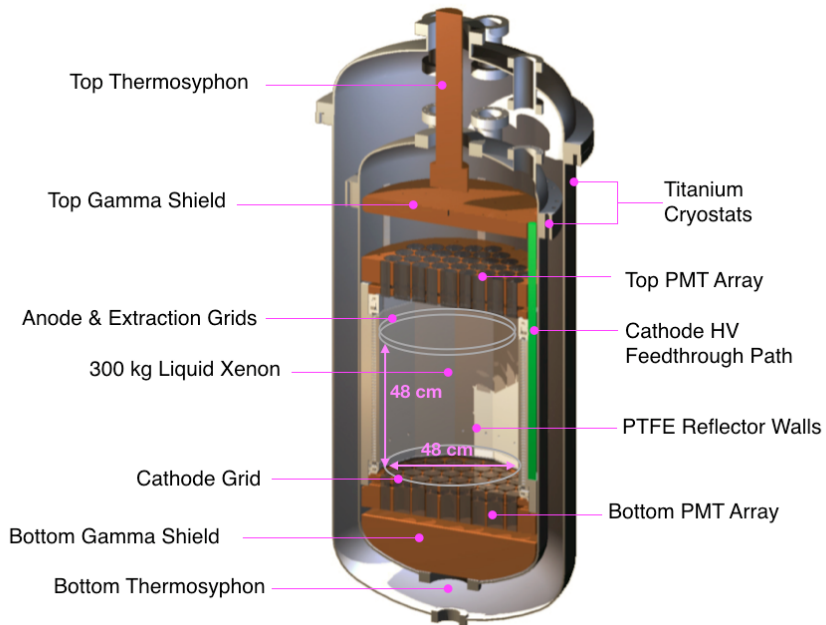


Figure 20: Major components and dimensions of the LUX detector.

The insides of the detector walls were lined with 12 PTFE panels, which made the exact detector geometry a dodecagonal prism with flat faces, instead of a cylinder one rounded face. Immediately behind the PTFE were 48 copper field-shaping “rings” (dodecagons). The rings were vertically separated by 1 cm, and the gate-to-cathode voltage was graded evenly over the rings by a resistor chain connecting the rings.

Below and above the PMT mounting blocks were two large solid copper domes which act as gamma shields and also function as thermal mass that aid in keeping the detector temperature stable. The bottom dome also acts as a heat exchanger to quickly re-thermalize incoming xenon

gas (from the circulation system) as it enters the liquid region, and minimizes the volume filled with non-active liquid xenon. See Figure 21 for details of the field-shaping rings and copper shields.

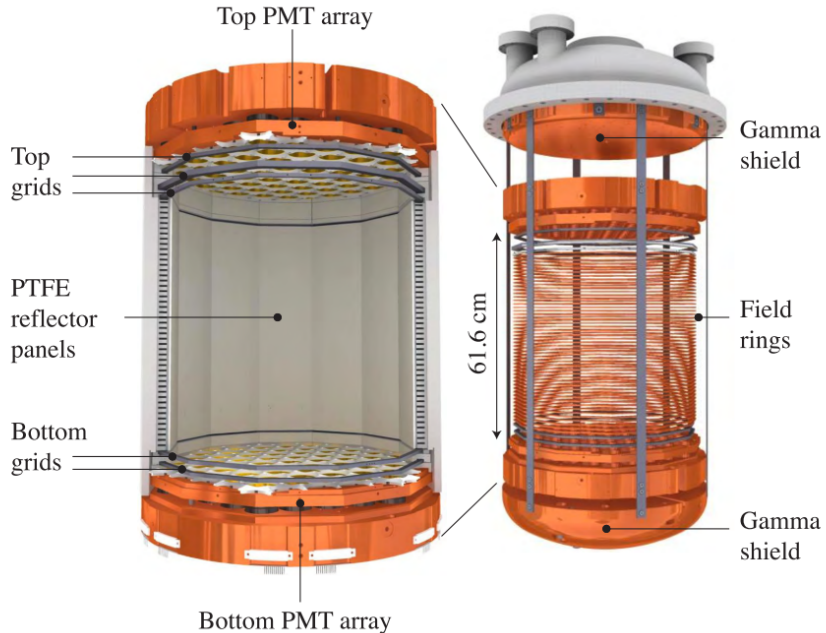


Figure 21: Field-shaping rings detail

More details about the internal components can be found in C. Faham’s PhD thesis [35].

### 4.3 EXTERNAL COMPONENTS

The [LUX](#) cryogenic system was based on thermosyphons, which deliver “cooling power” to solid copper cold heads, which are in thermal contact with the liquid xenon space. A simplified diagram is shown in Figure 22. A thermosyphon is a closed-loop cooling device containing a thermal messenger gas; N<sub>2</sub> is a common choice and was the choice for the [LUX](#) thermosyphons. The top of the thermosyphon is immersed in a bath of liquid nitrogen, and the bottom is in thermal contact with the liquid xenon space. The internal messenger gas condenses at the top and drips down to the cold head, where it absorbs heat from the xenon space, evaporates, and returns to the top of the thermosyphon to condense and repeat the cycle. In this manner, heat from the liquid xenon space is transferred to the external nitrogen bath, which boils off and must be periodically replenished. The pressure of the internal nitrogen messenger gas can be adjusted, providing more or less cooling power as desired. The [LUX](#) ther-

mosyphons were also instrumented with resistive heaters, for further fine control. Four thermosyphons were used to operate the LUX detector stably at 175 K with a xenon vapor pressure of 2 bar.

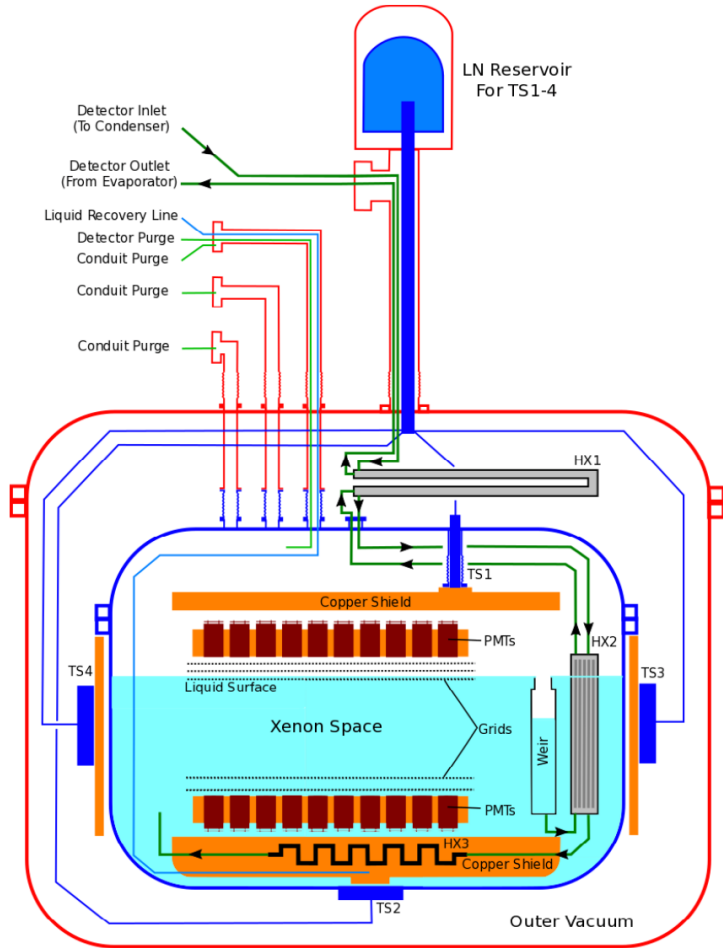


Figure 22: A simplified diagram of the LUX cryogenic system. [55]

The spillover liquid xenon from the liquid-level-setting weir mentioned above was directed into a circulation system through a series of heat exchangers that helped cool clean, incoming xenon gas. The xenon circulation was driven by one twin-head KNF double-diaphragm pump, which pushed liquid xenon from the spillover weir through a SAES MonoTorr heated zirconium getter to remove non-noble impurities before returning the clean xenon gas into the detector. A sampling system was able to pull xenon gas samples from different parts of the circulation system and measure impurity content, as well as test for the presence of  $^{85}\text{Kr}$  [56], a troublesome beta emitter which must be removed from the xenon prior to carrying out a successful WIMP search.

The circulation pump was installed in parallel with a backup pump, which could be switched on immediately in case of a pump outage. Flow was regulated to the system by two high-flow Mass Flow Controller ([MFC](#)s). Additional low-flow [MFCs](#) controlled purge flow through the cabling conduits in Figure 22 to ensure gas flow was away from the detector and prevent any contaminants from diffusing into the active xenon space.

Internal calibration sources were plumbed in to alternate flow paths of the circulation system. Xenon gas could be directed through a substrate source, such as the  $^{83m}\text{Kr}$  source described below, to pull  $^{83m}\text{Kr}$  into the detector volume. A bottle containing a source such as the  $\text{CH}_3\text{T}$  source described below could be used to deposit the gaseous source in an evacuated section of pipe. Xenon could then be directed through the section of pipe containing the source, sweeping it into the detector volume.

Lastly, [LUX](#) was placed in a 7.6 m diameter, 6.1 m high water tank (Figure 23). The shielding provided by the water tank attenuated the  $\gamma$  background from the cavern walls and thermalized neutrons from cavern background radioactivity and muon spallation. The water tank provided superior shielding from cavern radioactivity such that the detector backgrounds were dominated by the radioactivity of internal detector components, which in turn were controlled through a strict campaign of cleanliness and choice of detector materials [57], [58]. Vertical tubes visible in Figure 23 were used to deploy external calibration sources at different heights, such as  $^{137}\text{Cs}$ , which were directed into the detector via a collimating source assembly.



Figure 23: A photo of the LUX detector installed inside the water tank.

The LUX detector water tank and material screening achieved a very low background in the WIMP search energy range shown in Figure 24

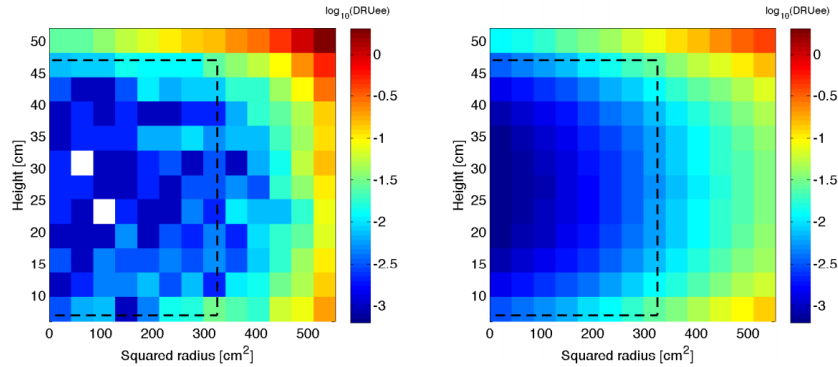


Figure 24: Backgrounds distributions in squared radius and height for expected (right) and measured (left) backgrounds in the energy range 0.9-5.3 keV<sub>ee</sub> (2-30 phe S1) for the 85.3 live-day Run03 WIMP exposure. Black lines show the 118 kg fiducial mass. Units are  $\log_{10}\text{DRU}_{ee}$ , electron equivalent differential rate units, i.e.  $\text{keV}^{-1}\text{kg}^{-1}\text{day}^{-1}$ . Figure from [58].

## 4.4 TRIGGER AND DATA ACQUISITION

Cabling for PMTs and other monitoring instrumentation were routed from the inner detector volume to the outside via conduits illustrated in in Figure 22. A flow char illustrating the signal path is shown in Figure 25.

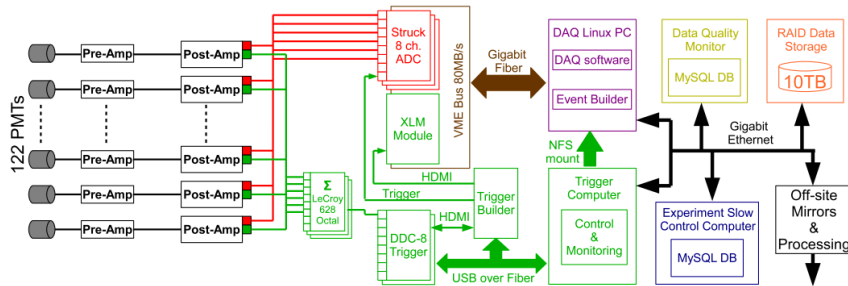


Figure 25: Overview of the LUX trigger system. Figure from [59].

The PMT signals were shaped and amplified by two sets of amplifiers. These analog voltage waveforms were then digitized by Struck Analog-to-Digital Converter (ADC)s, with 14 bit, 100 MHz sampling (1 sample every 10 ns). A copy of the analog PMT voltage waveforms passed through

the **LUX** Field Programmable Gate Array (**FPGA**) trigger system, which signaled the data acquisition computer to save the waveforms when they passed above a certain threshold, and stop when they fell below the threshold. Each of the 122 **PMTs** was dedicated its own channel in the recorded data, so recording only the channels that passed threshold allowed for a great amount of data reduction. This technique is called Pulse Only Digitization (**POD**). A **POD** threshold of 1.5 mV was used for **LUX**, which resulted in a single photoelectron efficiency of  $> 95\%$  [39]. A figure showing the **POD** threshold and example waveform are shown in Figure 26.

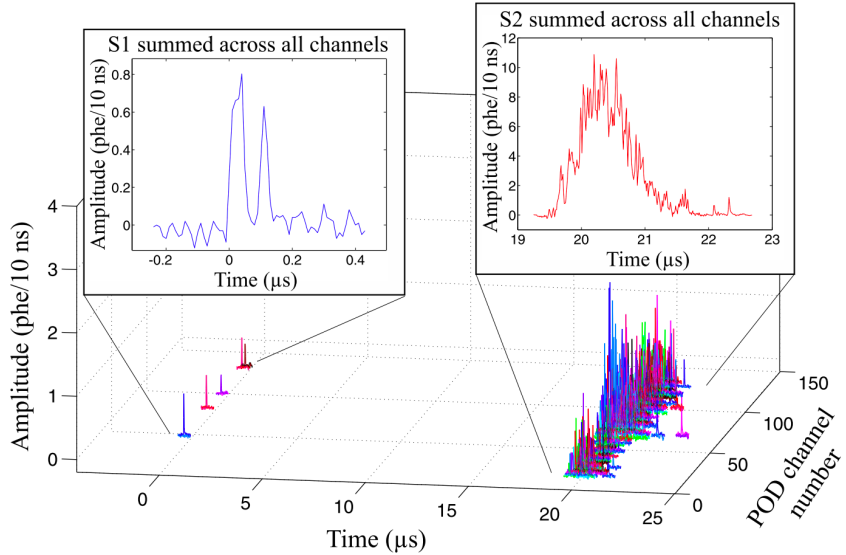


Figure 26: An example recorded event. Channels that do not pass the **POD** threshold are not recorded. The waveforms are summed over all channels to produce the **S1** and **S2** [59].

The channel-wise **POD** data is written continuously to disk as the **ADC** memory buffer fills; this is the rawest and least filtered form the **LUX** data that is saved in binary format with the **.dat** extension. The Event Builder takes the raw data and extracts portions located in a pre-trigger and post-trigger window. A additional hold-off time is applied after the post-trigger window to assure **PODs** are not duplicated by the subsequent event. The pre- and post-trigger windows for Run03 were set to be  $500 \mu\text{s}$ , chosen to ensure both **S1** and **S2** pulses were contained in the same event. The maximum electron drift time in Run03 was  $322 \mu\text{s}$ , so a pre- and post-trigger time of  $500 \mu\text{s}$  ensured no **S2** would appear without its partner **S1**. Both types can pass the **POD** threshold and signal the Data Acquisition (**DAQ**) computer to save the waveforms, but some small **S1s** are may not cross the threshold and must be “found” only at the event-

building stage. The Event Builder then saved the waveform data in binary format with the `.evt` extension.

## 4.5 DATA PROCESSING

After event-building, the waveform `.evt`-files were sent off site for additional processing. The `LUX` Data Processing Framework (`DPF`) extracts essential information from the waveforms and produces Reduced Quantity (`RQ`) files with the `.rq` extension. The `DPF` is modular, and can be applied repeatedly to the same `.evt` data with different settings if desired. `RQ` files include event-level information (e.g. trigger timestamp), pulse-level quantities (e.g. pulse type, pulse area), and some channel-level quantities (e.g. pulse area recorded by each `PMT`). The `DPF` classifies pulses as one of five types: S1, S2, Single Photoelectron (`SPHE`), Single Electron (`SE`), and Else (for pulses that do not fit one of the previous four types). The pulse-finding and classification algorithm was designed and optimized for the `WIMP` search, and is crucial in identifying `WIMP` “golden events”, which are single-scatter interactions with only one S1 and one S2 in the event. Detector backgrounds such as gammas often scatter more than once in the active volume, producing an event with one S1 and multiple S2s. The pulse-finder and classifier also play a large role in `LIP` search, which is discussed more in Chapter ch:lips. An example of pulse identification for a multiscatter event is shown in Figure 27

Following identification of S1 and S2 pulses, the `DPF` position reconstruction module is run. This module uses the Mercury algorithm, originally developed for the ZEPLIN-III `LXe TPC` [60], which is based on maximum-likelihood to find the best (x,y) position of the event. Mercury uses Light Response Function (`LRF`s), obtained for each `PMT`, to predict the response of the `PMT` to interactions at some arbitrary position of the `PMT`. The `LRF`s were obtained using calibration data, of which  $^{83m}\text{Kr}$  was the most important for position reconstruction. The position reconstruction method and `LRF`s are discussed in more detail in [61].

The `DPF` also applies calibration constants to the data. Calibration constants, many of which change over time, are tracked and recorded in the `LUX` Electronic Log (`LUG`), which produces date-specific record files in XML format, which in turn determine the settings for some of the `DPF` modules. For example, the  $^{83m}\text{Kr}$  calibration (see Section 4.6.2) was used to normalize S1 pulse areas. The photon detection efficiency for S1s varies with z-position, with events occurring near the bottom `PMT`s 50% more likely to be detected than those near the liquid-gas boundary. The `DPF` applies corrections like this to several RQs, and both the corrected and uncorrected versions are kept.

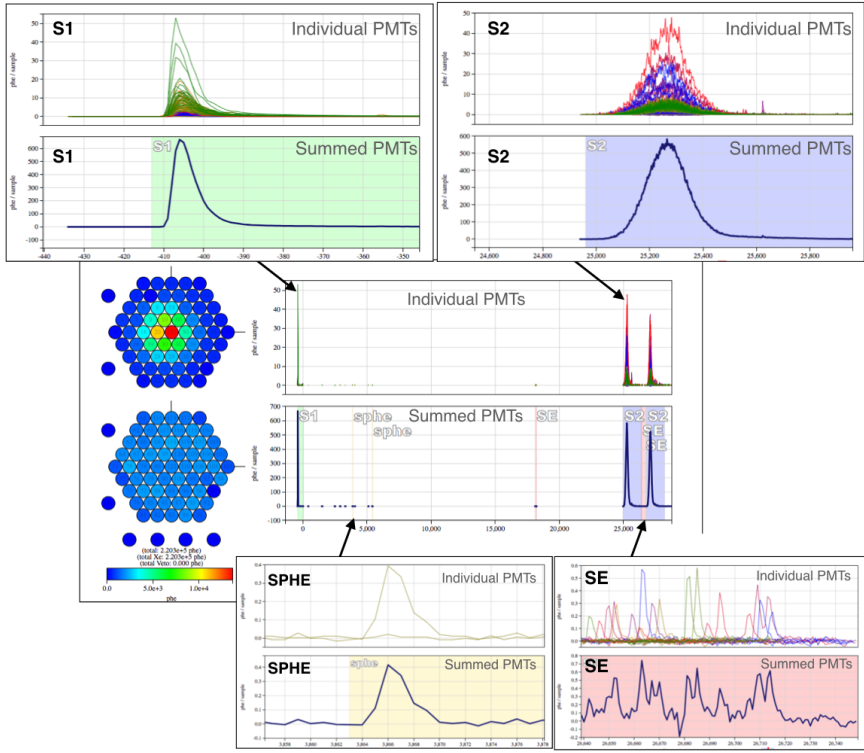


Figure 27: An example of [LUX](#) pulse classification showing individual pulses.

## 4.6 CALIBRATIONS

Several novel calibration methods were developed by the [LUX](#) Collaboration to fully characterize the detector. The superior self-shielding ability of [LXe](#) detectors also makes them difficult to calibrate. Sources placed external to the detector cannot penetrate the fiducial volume very effectively; since high-statistics are desired for calibration data, relying on external sources becomes untenable. The solution, then, is counterintuitive: purposely introduce radioactive material into painstakingly developed, ultra low-background, fiducial volume of the detector. For such a source to not destroy the ability to carry out a [WIMP](#) search, it must either (i) be short lived or (ii) be effectively removed by getter on a short timescale. [LUX](#) demonstrated that  $^{83m}\text{Kr}$  fit the former [62] requirement and tritiated methane ( $\text{CH}_3\text{T}$ ) fit the latter [63].

## 4.6.1 ENERGY

This section covers the energy calibration of [LUX](#). Recall from Section 3.2.1 that the electron-equivalent energy of an event in a dual phase xenon TPC is reconstructed as follows:

$$E = W \left( \frac{S1}{g_1} + \frac{S2}{g_2} \right) \quad (27)$$

Two or more calibration line sources of different energies are required to fit for the detector gains  $g_1$  and  $g_2$ . The [LUX](#) experiment used a suite of sources to calibrate the energy response of the detector, shown in 28. The  $^{83m}\text{Kr}$  is an injected source distributed in the entire internal volume. The  $^{137}\text{Cs}$  is an external source lowered at different heights into the source tubes. The xenon lines,  $^{131}\text{Xe}$ ,  $^{129}\text{Xe}$ ,  $^{127}\text{Xe}$ , are of cosmogenic origin and were only present early in Run03.

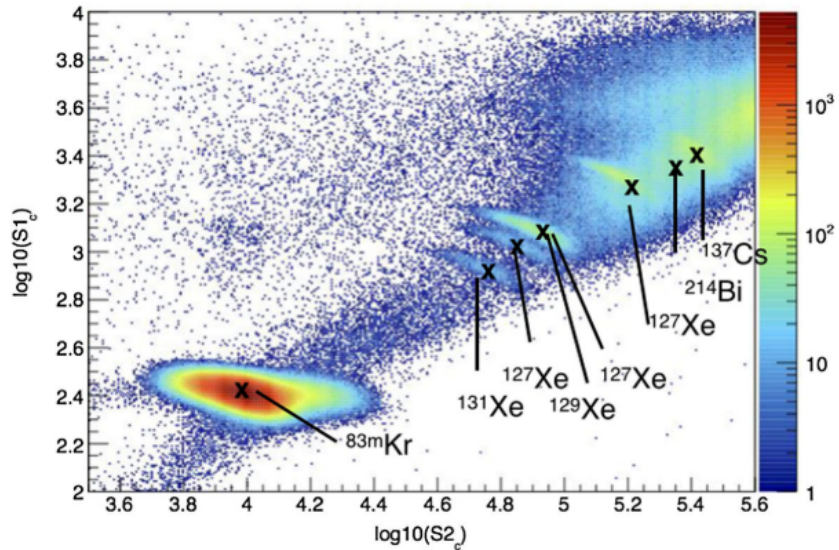


Figure 28: Plot showing calibration sources (Figure from [39]). The axis label subscript  $c$  denotes corrected variables with calibration for geometrical effects and electron lifetime (these corrections are discussed in Section 4.6.2).

The average  $S1$  and  $S2$  of each calibration source is normalized to the true energy:

$$(S1, S2) \rightarrow \left( \frac{\langle S1 \rangle}{E}, \frac{\langle S2 \rangle}{E} \right) \quad (28)$$

and a line  $y = mx + b$  is fit to the transformed variables, where the slope is  $m = -g_1/g_2$  and the y-intercept is  $b = g_1/W$ . Such a plot is called a Doke plot. The sources from figure Figure 28 are shown normalized in a Doke plot in Figure 29.

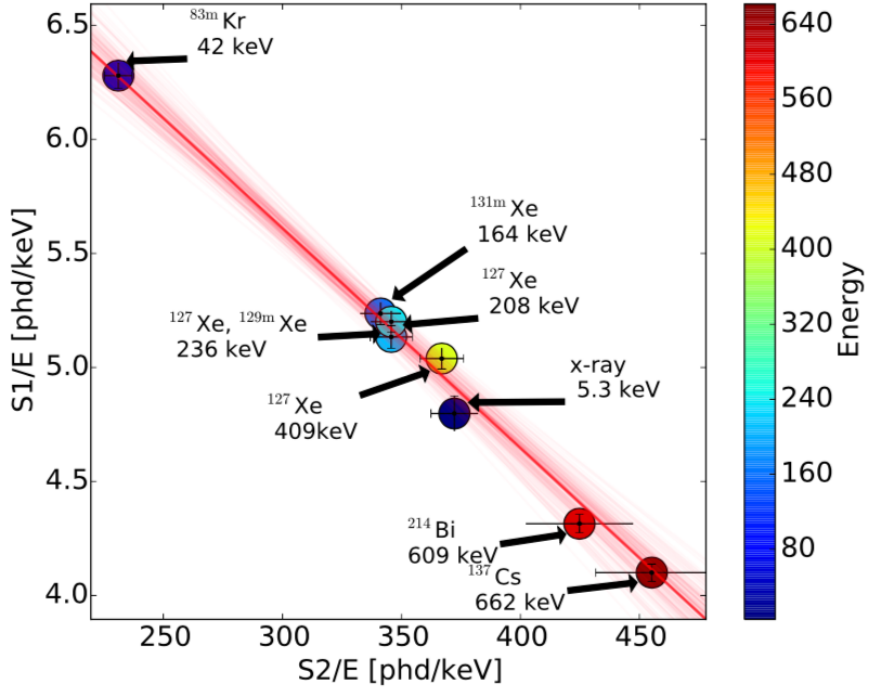


Figure 29: Doke plot used to fit  $g_1$  and  $g_2$  for LUX Run03 (Figure from [39])

From the fit in Figure 29, the LUX gains for Run03 were measured to be  $g_1 = 0.117 \pm 0.003$  phd/photon and  $g_2 = 12.1 \pm 0.8$  phd/electron.  $g_2$  depends on a combination of the EEE and the number of photons produced by a single extracted electron – it is useful to know both values. Single electrons are periodically emitted into the gas and undergo proportional scintillation. This phenomenon is well known in liquid xenon detectors and is discussed further in Chapter 8. A sample of pure single electrons was collected to find the average number of S2 photons produced by one electron, referred to the single electron size. The single electron size in Run03 was a skew-gaussian with mean 24.66 phd and a  $1-\sigma$  width of 5.95 phd. Combing this with  $g_2$  gives an EEE of  $49\% \pm 3\%$  [39].

#### 4.6.2 METASTABLE KRYPTON-83 ( $^{83m}\text{Kr}$ ): A MULTIFUNCTION CALIBRATION

The  $^{83m}\text{Kr}$  source used by LUX was  $^{83}\text{Rb}$  deposited on a charcoal substrate. Gaseous xenon within the circulation system was diverted over the char-

coal substrate, where it could sweep  $^{83m}\text{Kr}$  on a flow path through the getter, and then into the detector.

$^{83m}\text{Kr}$  decays by two steps releasing a total energy of 41.5 keV. The two branching ratios that dominate are first the internal conversion and subsequent Auger emission of a 32.1 keV  $\beta$  followed by another internal conversion and Auger emission of a 9.4 keV  $\beta$ , with an intervening half-life of 154 ns. The time structure of the decay sometimes yields two S1s, called S1a and S1b. If the second 9.4 keV  $\beta$  is prompt (i.e. within the timing resolution of the detector), then only one S1 is observed. The S2s are always merged because (1) the low energy of the decays made the energy depositions  $O(10 \mu\text{m})$  from each other, smaller than the position resolution of the detector  $O(1 \text{ mm})$  (2) the close timing of the two decays was smaller than the typical electron diffusion distances during drift  $O(1 \text{ mm})$ , merging the two electron bunches together into one S2 [62].

$^{83m}\text{Kr}$  was a workhorse calibration source for LUX, with  $^{83m}\text{Kr}$  injections performed weekly at activities ranging from 10 Bq to hundreds of Bq, depending on the specific calibration goal.  $^{83m}\text{Kr}$  was found to mix uniformly in the detector within 10 min of the injection, and would decay (half life 1.83 hours) back to an acceptable WIMP search background rate within a day, or few days, depending on the injected activity [62]. The combined energy of the  $^{83m}\text{Kr}$  was well out of the WIMP search energy range, so no long-term pollution, though unlikely, was risked.  $^{83m}\text{Kr}$  was used for two main calibrations, described below.

**Pulse Area Corrections** Detector efficiencies and gains can vary over time and position within the detector.  $^{83m}\text{Kr}$  served as a “standard candle”, which produced monoenergetic signals with uniform initial light and charge yields distributed uniformly throughout the active volume. The efficiency for detecting the initial light yield as an S1 was dominated by spatially varying geometrical light detection efficiency. The areas of the S1s were binned in 3D, and the averages were found for each bin. A correction map was then constructed as the inverse of the S1 areas, normalized to the S1 amplitude at the center of the detector. The map of relative S1 amplitudes in Figure 30 (left) shows the strong  $z$ -dependence for S1 light collection. The corrections for S2 areas were more complex, as detection efficiency for the initial charge yield as an S2 depends on the presence of electronegative impurities, electron extraction efficiency, production of proportional scintillation photons, and then detection of those photons in PMTs. The  $xy$ - and  $z$ - dependence for S2s are corrected in two separate maps. The electronegative impurities caused a strong  $z$ -dependence in S2 size – events originating at the bottom of the detector must drift longer and so were more likely to encounter and lose electrons to impurities. The  $z$ -dependent S2 area correction map was an exponential function of drift time, normalized to unity at the liquid surface. The  $xy$ -dependence

was from detector conditions such as pressure, liquid level, and electric field deflection from the grid. The  $xy$ -correction map for S2s was normalized to (0,0) in the x-y plane. Examples of both the z and  $xy$  S2 area correction maps can be seen in Figure 30 (right).

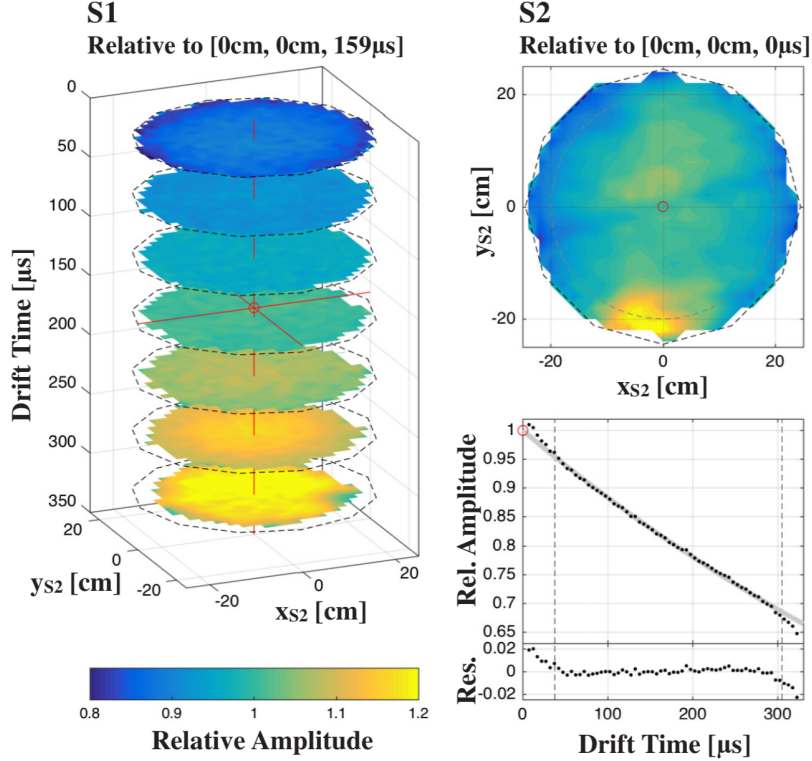


Figure 30: Spatial dependence of pulse area corrections for S1 (left) and S2 (right) from an example  $^{83m}\text{Kr}$  calibration. The red circle indicates normalization point. (Figure from [62])

**Position Corrections** 3D position reconstruction depends on a full understanding of the path electrons take from an interaction site to the position observed after extraction at the surface. The reconstructed position of the proportional scintillation signal in the xy-plane, based on the Mercury algorithm, is referred to “S2 coordinates”, often with subscripts ( $x_{S2}$ ,  $y_{S2}$ ). The real coordinates may be displaced from ( $x_{S2}$ ,  $y_{S2}$ ) due to, for example, a radial field pushing electrons inwards deep in the detector. In fact, there was a small radially inward component to the electric fields in LUX Run03 due to the geometry of the field cage and grids (Figure 31). The spatial distribution of reconstructed  $^{83m}\text{Kr}$  events was used to verify a COMSOL multiphysics electric field model of the detector by drifting electrons in simulation under the electric field model conditions. This field model could then be used to transform events from S2 coordinates to real (x,y) coordinates, however this was not done for Run03. Instead,

the  $^{83m}\text{Kr}$  data itself was found to be more precise in for position corrections, since it didn't rely on the accuracy of the field model or electron drift simulation (Figure 32). The electric field conditions were very different in Run04, and so extensive calibrations and field maps were used to map S2 coordinates to real coordinates [64].

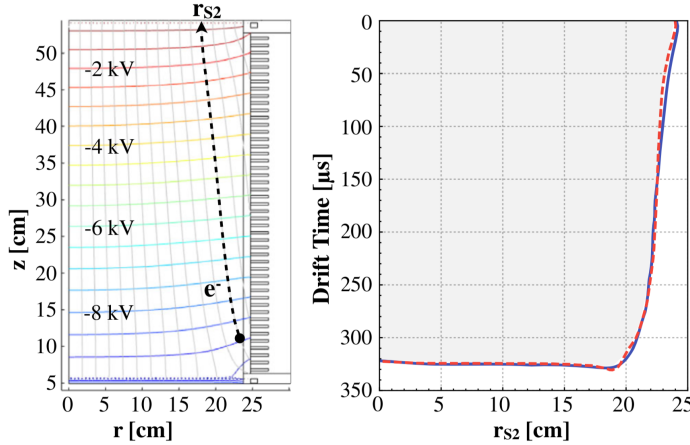


Figure 31: (Left) A simplified 2D COMSOL model showing electric field lines and equipotentials for the LUX detector in Run03. A radially inward component is seen. (Right) The resulting edge S2 coordinates of a uniform distribution of electrons drifted under the electric field model is shown in solid blue. The edge S2 coordinates of from  $^{83m}\text{Kr}$  data is in dashed red; it is consistent with the field model prediction. Figure from [62]

In addition to the small radial dependence, the electric fields illustrated in Figure 31 also vary in magnitude. The two decays of  $^{83m}\text{Kr}$  can be leveraged to directly probe the magnitude of the field, as they exhibit different field dependence. The ratio of S1a to S1b increases with field, and provides a measure the spatial dependence of the magnitude of the electric field. A highly variant electric field would affect recombination, and cause different light and charge yields at different positions in the detector, in turn affecting sensitivity. The fields measured via this method in Run03 were found to only cause corrections on the order of a percent and so no field-dependent corrections were applied [62]. However, in Run04 the ratio technique was of central importance (see [65] [64] [62] for more detail). The result of the ratio method for measuring electric field magnitude is shown in Figure 33 for Run03 fields.

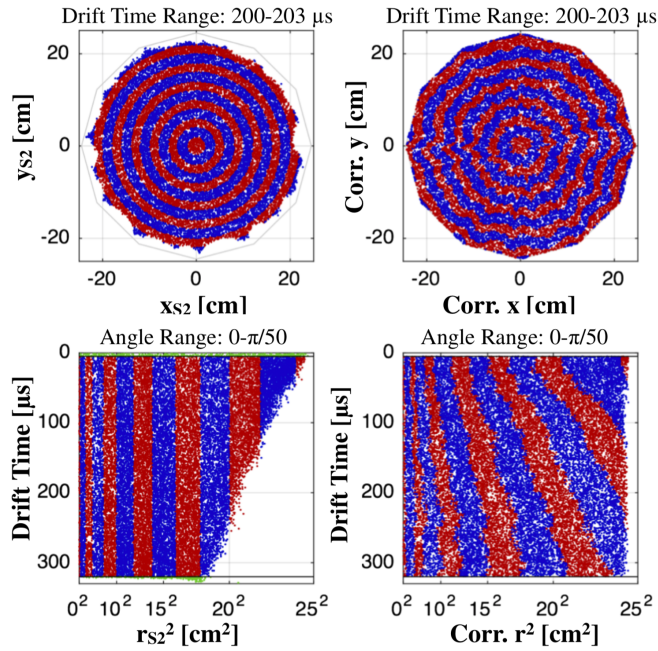


Figure 32: The effect of radial position mapping between S2 coordinates (left) and real coordinates (right). The top panels show a thin horizontal slice of the detector and the bottom panels show a thin vertical slice. The red and blue colors are used to make the effect of the mapping visible. Note that squared radius in the bottom panels exaggerates the scale of the effect. Figure from [62]

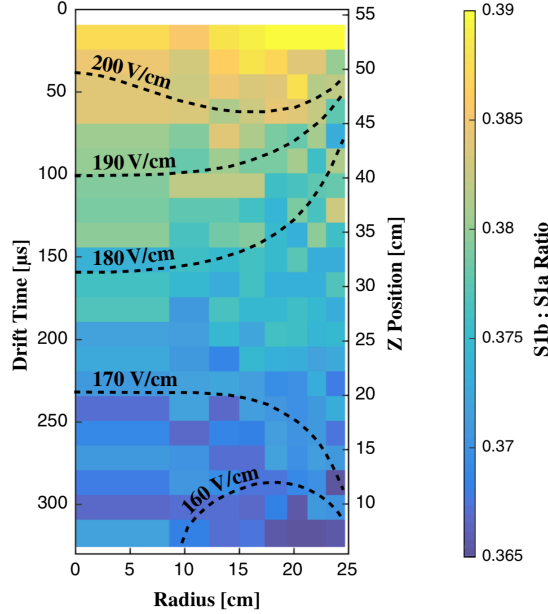


Figure 33: Field map of Run03 produced by  $^{83m}\text{Kr}$  S1a:S1b ratio. Because only a fraction of  $^{83m}\text{Kr}$  produce separate S1a and S1b, the bins are large to accomidate reduced statistics. Figure from [62]

### 4.6.3 TRITIUM BETA DECAY: CALIBRATION OF THE ER BAND AND YIELDS

In order to calibrate the **ER** band of **LUX** a  $\beta$  source in the **WIMP** energy range was needed. **LUX** used a gaseous tritiated methane ( $\text{CH}_3\text{T}$ ) source to deliver tritium uniformly into the active volume. Tritiated methane was chosen over the molecular tritium ( $\text{T}_2$ ) because it does not adsorb onto surfaces like the smaller  $\text{T}_2$  molecule and it does not interfere with charge transport in **LXe** [63]. Tritium has a Q-value of 18.6 keV, but the spectrum peaks at 2.5 keV, with 64.2% of the decays occurring in the **WIMP** search energy range of 1 to 8 keV [63]. The half-life of tritium is 12.3 years, so efficient removal was essential. **LUX** demonstrated that once deployed,  $\text{CH}_3\text{T}$  was removed with a 6 hour time constant, returning the detector back to acceptable **WIMP** search rates.  $\text{CH}_3\text{T}$  was shipped to site in a bottle, mixed with purified xenon and released into the circulation system after the getter, to be swept into the inner volume.

The tritium energy spectrum from data is shown with the theoretical energy spectrum convoluted with the detector energy resolution in Figure 34 (left). The ratio of the two is shown in Figure 34 (right), demonstrating a 50% effective energy threshold for **ER** events at  $1.24 \pm 0.026$  keV. The agreement between data and theory shows powerful support for the energy model  $E = W(S1/g_1 + S1/g_2)$ .

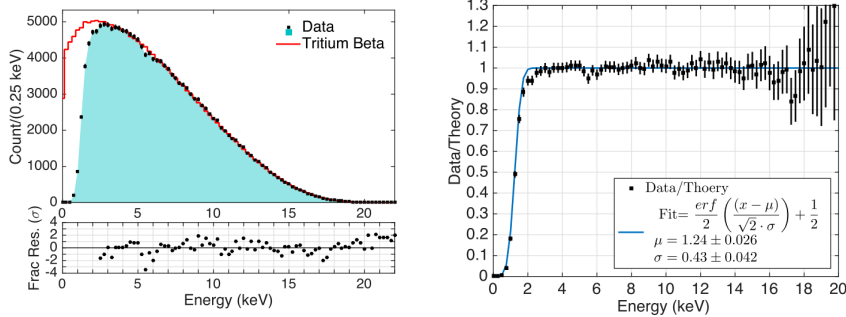


Figure 34: (Left) Plot showing the theoretical tritium beta spectrum with the spectrum obtained from data, and residuals. (Right) The ratio of data to theory convoluted with the detector energy resolution. Figure from [63]

Tritium was also used to measure the light and charge yields over a wide energy range. Figure 35 (left) shows the detected number of quanta,  $n_\gamma$  and  $n_e$ . Recall that this is not necessarily the number of initial quanta  $n_{ex}$  and  $n_{ion}$  that are produced, as some number of  $n_{ion}$  undergo recombination to produce additional scintillation photons. Figure 35 (right) shows the effect that event energy has on recombination. For ER events  $n_{ex}/n_{ion} = 0.2$  is assumed to be constant [LUXYieldsAndRecombination], but the observed ratio  $n_\gamma/n_e$  is clearly energy dependent.

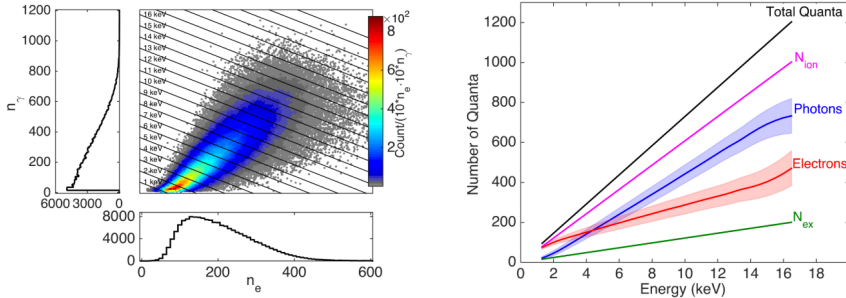


Figure 35: (Left) The measured quanta yields shown with lines of equal energy. (Right) A plot depicting the expected initial quanta yields,  $N_{ion}$  and  $N_{ex}$ , compared with the measured yield of photons and electrons. The difference is caused by the energy dependence of recombination. Figure from [63]

Lastly, as is tritium was used to construct the ER band (Figure 36 (left)), which is necessary for WIMP search. The width of the ER band is of significant interest, as it determines the nuclear recoil discrimination of the detector. The number of ER events from the tritium calibration that occur below the nuclear recoil band mean is known as leakage fraction ( $f$ ),

and is shown as a function of energy in (Figure 36 (right)). The average **ER** discrimination efficiency ( $1 - f$ ) for Run03 was  $99.81\% \pm 0.02\%(\text{stat}) \pm 0.1\%(\text{sys})$ , where the systematic error comes from the error on  $g_1$  and  $g_2$ . This measurement of discrimination efficiency relies on knowing the mean and width of the **NR** band, which is discussed in the next section.

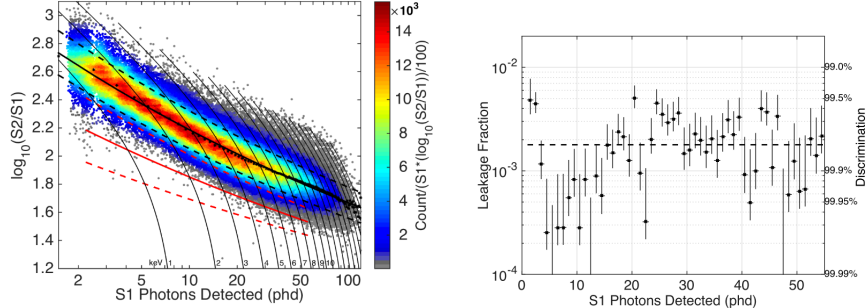


Figure 36: (Left) The **ER** band for in **WIMP** search energy range obtained from the tritium calibration. (Right) Leakage fraction of **ER** events below the **NR** mean in the **WIMP** search energy range. Knowledge of the **NR** band comes from the **DD** calibration detailed in Section 4.6.4. Figure from [63]

#### 4.6.4 LOW-ENERGY NUCLEAR RECOILS FROM DEUTERIUM-DEUTERIUM (DD) NEUTRONS: NR BAND AND YIELDS

A **DD** generator was used to calibrate the **NR** response and signal yields for **LUX** in the **WIMP** search energy range. A photo and diagram of the calibration scheme are shown in Figure 37. Following Run03, **LUX** employed the **DD** generator to deliver a collimated beam of 2.45 MeV neutrons into the **TPC**. As Figure 37 shows, the generator was positioned outside the water tank, but when aligned with the neutron conduit (a Polyvinylchloride (**PVC**) tube of air), deposited neutrons into the **LXe** space. The **DD** calibration leverages known kinematics of neutron scattering, the known incoming neutron energies, and the known detector gains  $g_1$  and  $g_2$  to develop a complete characterization of low-energy **NR** in **LUX**. The method is summarized here, but details are available in [66].

First, charge yield was derived from a population of multiscatter events: those with one S1 (the S1s are merged due to simultaneous collection of S1s) and two S2s (separated in space and z-position/drift time). Neutron scattering kinematics allow for the reconstruction of energy at the first scatter site, so the unknown first S1 is not needed to ascertain the energy deposition. The charge yield is then obtained from the first S2 and the energy of the first scatter from kinematics.

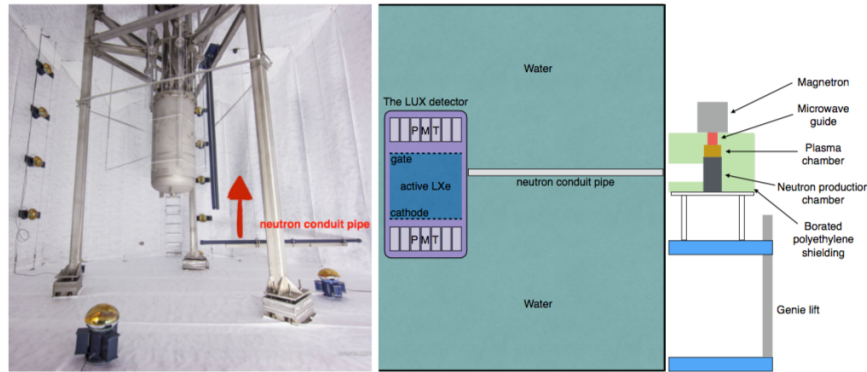


Figure 37: (Right) Photo of the water tank interior showing the neutron conduit, which is raised during [DD](#) calibration. (Left) Diagram of the [DD](#) generator and water tank neutron conduit during [DD](#) operation. Figure courtesy of E. Pease.

Once the charge yield was obtained, a population of single scatter events was collected: one S1 and one S2. These events were from neutrons that scattered once the detector, and then exited. Here, the second scatter is not available to kinematically reconstruct energy, so instead the charge yield is employed to infer the energy of the single scatter. The light yield is then obtained from the S1 and the energy deposition inferred from charge yield.

It should be noted that though the [DD](#) generator produced monoenergetic neutrons of initial energy  $E_i$ , the energy deposited  $E_d$  by a neutron scatter is

$$E_d = E_i \frac{m_n M_{Xe}}{m_n + M_{Xe}} \sin^2 \theta_{CM} \quad (29)$$

Where  $m_n$  is the neutron mass,  $M_{Xe}$  is the xenon mass, and  $\theta_{CM}$  is the scattering angle relative to the neutron conduit in the center of mass frame. The deposited energy,  $E_d$  then covers a range of energies, allowing for calibration of the [NR](#) band and yields over a range of energies. After determination of the light yield, the single scatter events were used to construct the [NR](#) band in Figure 38.

#### 4.6.5 POWER OF LUX CALIBRATIONS

Although this thesis is concerned mainly with a search for [LIPs](#), it should be noted that the extensive [LUX](#) calibrations allowed for excellent understanding of the detector, resulting in a world-leading [WIMP](#) limit. In particular, the [DD](#) calibration (carried out after Run03) yielded a much better

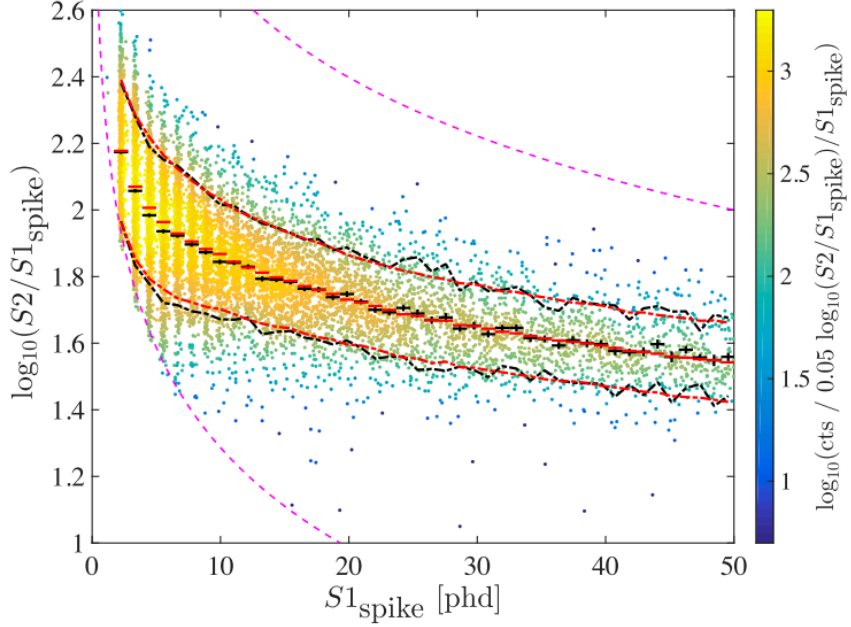


Figure 38: Calibration showing the [NR](#) band mean and width from the [DD](#) calibration. Figure from [66]

understanding of the [NR](#) band and yields, and therefore detector thresholds, than the initial AmBe neutron calibration which was carried out in the early days of [LUX](#). The power of the [DD](#) calibration can be seen in the difference between the first [LUX](#) result [47] and the Run03 re-analysis [67] shown in Figure 39. In particular, improved knowledge of the scintillation yields allowed a re-analysis threshold down to  $1.1 \text{ keV}_{nr}$  where the initial [WIMP](#) search adopted the more conservative threshold of  $3.0 \text{ keV}_{nr}$ . This improvement allowed [LUX](#) to exclude new spin-independent parameter space below a [WIMP](#) mass of 10 GeV.

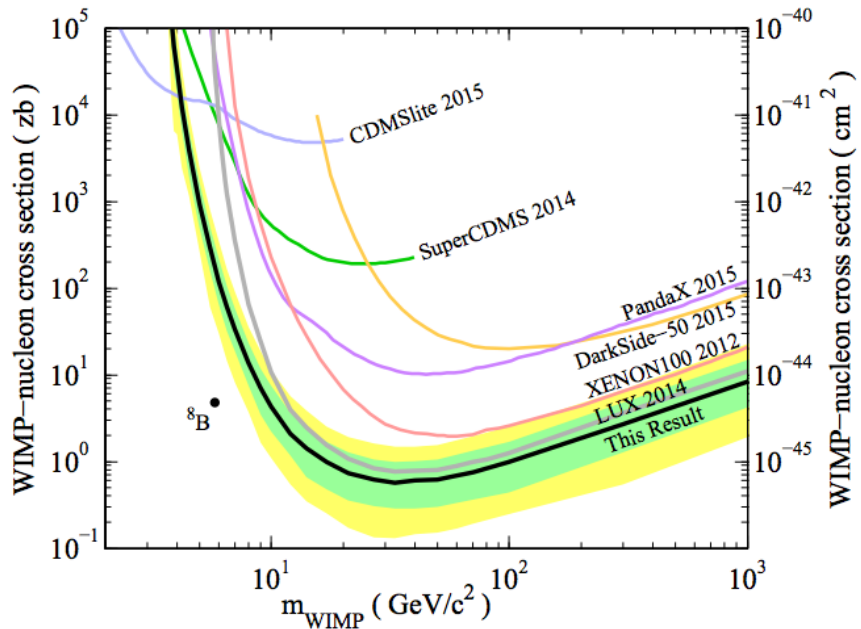


Figure 39: Improved spin-independent WIMP limit of the Run03 exposure following the DD calibration of LUX. The first Run03 limit is the gray line labelled “LUX 2014”, the improved Run03 observed limit is the black line labelled “This Result”. Figure from [67]

# 5

## LIGHTLY IONIZING PARTICLE SEARCH

---

*And all this science I don't understand,  
It's just my job five days a week*

— Elton John *Rocket Man*, 1972

### 5.1 MODELING LIP INTERACTION

#### 5.1.1 COLLISION CROSS SECTION

A LIP interacting in the LXe volume loses energy via interaction with electrons. To model LIPs in LUX, the expression of interest is the collision cross section Collisional Cross Section (CCS). The differential CCS describes the energy lost to electrons in a single collision for incident energy of the LIP. For particles with charge  $ze$  and mass M heavier than the electron mass,  $m_e$  (“heavy” particles), the Rutherford cross section is a familiar differential CCS [68]:

$$\frac{d\sigma_R}{dE} = \frac{2\pi r_e^2 c^2 z^2}{\beta^2} \frac{1 - \beta^2 E/T_{max}}{E^2} \quad (30)$$

where  $r_e$  is the classical electron radius,  $E$  is the energy loss of incoming particle,  $\beta = v/c$  of the incoming particle, and  $T_{max}$  is the maximum energy transfer possible in a single collision:

$$T_{max} = \frac{2m_2 c^2 \beta^2 \gamma^2}{1 + 2\gamma m_2/M + (m_e/M)^2} \quad (31)$$

Often the expression  $T_{max} \approx 2m_e c^2 \beta^2 \gamma^2$  for  $2\gamma m_2/M \ll 1$  is used implicitly, or is referred to as the “low energy approximation” in older texts. The Rutherford cross section is a good starting point, but it describes the “hard interaction” or head-on, billiard-ball type collision of a particle interacting with free electrons. Real electrons are bound in atoms, and an incident particle can undergo “soft interactions”, in which virtual photons are exchanged. When the virtual photon matches the energy of electron

orbitals of the target material, there are resonances in the [CCS](#). The energy transfer,  $E$ , must also be finite in real atoms, where the dielectric properties modify the electromagnetic field of a moving charged particle and limit the growth of the cross section. This real-world behavior is described by a correction factor  $B(E)$ , also sometimes called an “inelastic form factor” [68]:

$$\frac{d\sigma_{CCS}}{dE} = \frac{d\sigma_R}{dE} B(E) \quad (32)$$

Various attempts, spanning a better half of the last century, have been made to take into account the real-world behavior of electrons bound in matter. Some of these can be found in [cite 18,27, 41-43 papers from Bichsel]. More well-known contributions are those of Bethe and Fano. In 1930, Bethe derived a cross section doubly differential in energy loss and momentum transfer using the first Born approximation for scattering on free atoms [69]. In 1963, Fano extended the method to describe atoms in solids [70]. Combining their two methods yields the Bethe-Fano cross-section, which has undergone much study and by our current understanding has been verified to be close to reality [71]. There is another method, called the Photo Absorption Ionization ([PAI](#)) model, that is easier to calculate than the Bethe-Fano cross section, and approximates the Bethe-Fano calculation very closely. This thesis uses the [PAI](#) model as a base, building the full signal model for [LIPs](#) interacting in the [LUX](#) detector.

### 5.1.2 PHOTO ABSORPTION IONIZATION MODEL FOR CHARGE PARTICLE ENERGY LOSS

The [PAI](#) model is also sometimes known as the Fermi Virtual Photon ([FVP](#)) or Weis&Ocker-Williams approximation. A full description of the [PAI](#) model is described in detail in [72]. The complex dielectric constant  $\epsilon = \epsilon_1 + i\epsilon_2$  can be thought of as encoding all the information about a medium. The real part  $\epsilon_1$  describes the polarization of the material and imaginary part  $\epsilon_2$  describes the absorptive properties. Typically both  $\epsilon_1$  and  $\epsilon_2$  are thought of as functions of  $\omega$ , or incident photon energy. So  $\epsilon(\omega) = \epsilon_1(\omega) + i\epsilon_2(\omega)$ . This description is limited to free photons, but we desire to describe inelastic collisions as well. So  $\epsilon(k, \omega)$ , a generalized dielectric constant, is introduced to describe momentum transfer  $k$  to atomic electrons. The generalized dielectric constant  $\epsilon(k, \omega)$  can be related to atomic matrix elements, and if desired, calculated completely and tediously. However, the [PAI](#) model allows us to avoid these tedious calculations by making specific approximations, which, when taken together, define the [PAI](#) model itself.

In particular, the PAI model approximates  $\epsilon_2(k, \omega)$  by noting that typically, the momentum  $k$  transferred to an electron is much less than the energy transfer  $\omega$ .

### 5.1.3 STRAGGLING

### 5.1.4 ENERGY RESOLUTION IN LUX

### 5.1.5 POSITION RESOLUTION IN LUX

## 5.2 LIP SEARCH

### 5.2.1 LUX RUN03 CONDITIONS

## 5.3 LIP SEARCH ANALYSIS

### 5.3.1 ENERGY CONSISTENCY

### 5.3.2 TRACK LINEARITY CRITERIA

### 5.3.3 BACKGROUND REJECTION

### 5.3.4 MUONS

### 5.3.5 GAMMAS

### 5.3.6 ELECTRON TRAINS?

## 5.4 RESULT: VERTICAL FLUX LIMIT

### PART III

## LITTLE SCIENCE

This section describes research with a small test bed at Lawrence Berkeley National Lab.

# 6

## RESEARCH AND DEVELOPMENT FOR FUTURE LXE TPCS

---

*All systems go, are you sure?*

— Peter Schilling *Major Tom*, 1969

A small test bed was built at Lawrence Berkeley National Laboratory to study various detector effects facing large [LXE TPCs](#). The test bed was built and instrumented over the course of about two years, from 2015 through 2016. This chapter describes some of the details of that instrumentation.

### 6.1 TEST BED APPARATUS OVERVIEW

The experimental apparatus consisted of an inner vessel, a vacuum outer vessel, and a xenon circulation system. The inner vessel was a Stainless Steel ([SS](#)) canister, topped with a 2.75 in Conflat-adaptable tower that allowed space for instrumentation cabling and [HV](#) feedthroughs. The inner vessel was offset below a 7.09 in ISO K flange, which held the (removable) vacuum outer vessel in place. Several Mini-CF ports were welded to the ISO K flange for instrumentation cabling. A large-scale overview is shown in Figure 40.

The inner vessel contained the [TPC](#). A PTFE housing cylinder fastened a PMT in place. Above the PTFE housing, a series of interlocking PTFE rings held strung wire grids and a segmented anode in place. During data taking, the entire PMT and housing were immersed in [LXe](#). The liquid level was chosen depending on the experiment at hand, approximated by the S2 width. In some cases, the TPC was “overfilled” by allowing the liquid level to rise above the anode. The segmented anode was instrumented with charge amplifiers for direct charge readout. When the [TPC](#) was overfilled, the charge amplifiers detected the ionization electrons directly from the liquid. During typical dual phase [TPC](#) operation, the charge amplifiers provided a secondary measurement of the ionization electrons in addition to S2. Two typical arrangements of the inner vessel are shown in Figure 41.

## 6.1 TEST BED APPARATUS OVERVIEW

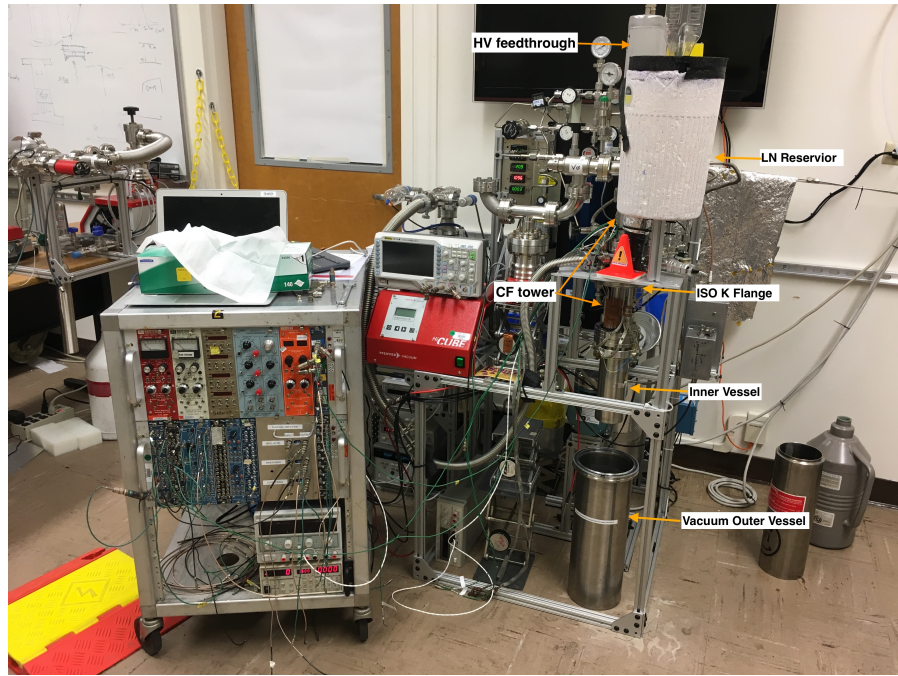


Figure 40: Large scale view of the experimental apparatus showing key parts.

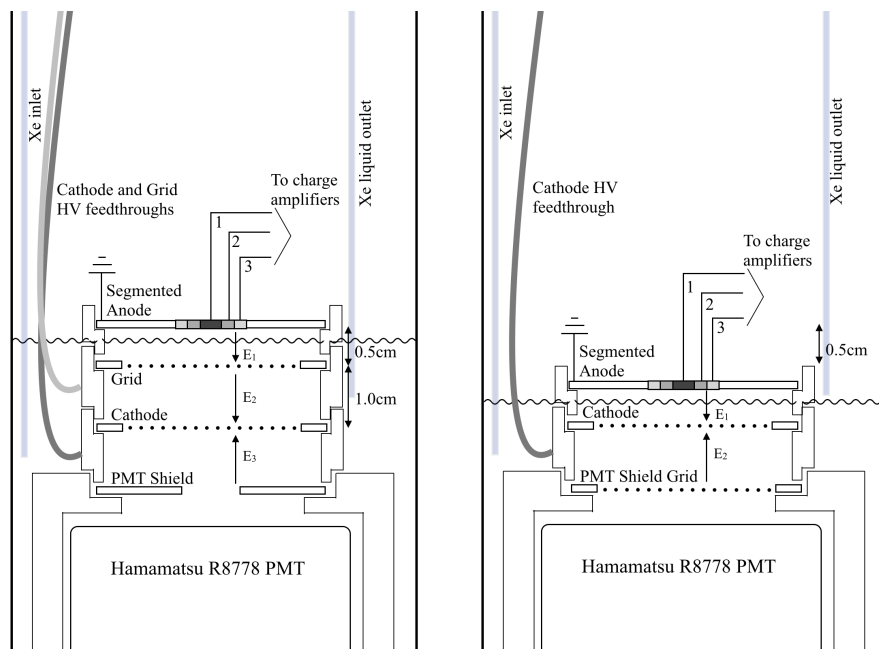


Figure 41: Diagrams of two often used internal arrangements.

## 6.2 CIRCULATION SYSTEM

The xenon circulation system is shown in Figure 42. A stainless steel capillary extending into the liquid drew xenon from the inner vessel during operation to be purified. Purified xenon that was returned to the vessel was directed into the liquid via a PTFE tube so it could condense quickly. A gas purge was added to the Conflat (CF) tower above the inner vessel to continually renew the gas column.

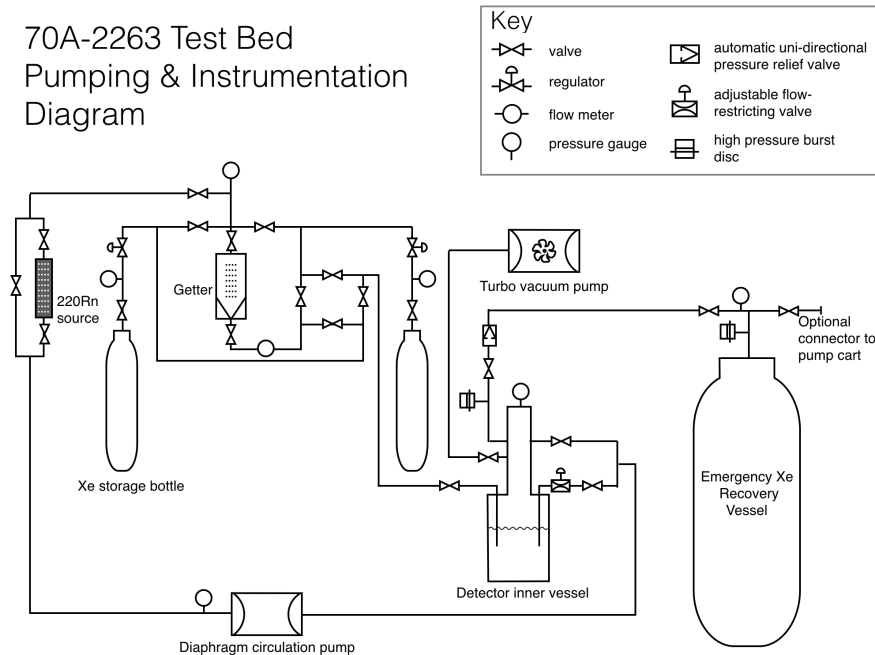


Figure 42: Pumping and instrumentation diagram of the test bed. Special symbols are labelled in the diagram, see key for other symbols. For readability, all gauges are not shown.

## 6.3 CHARGE AMPLIFIERS

The segmented anode was instrumented with three CR-110 charge amplifiers from Cremat (Figure 43). The raw charge amplifier signals were each fed into a CR-160-R7 shaper evaluation board, also from Cremat. The evaluation board houses two more modules: one CR-200-X shaping amplifier and one CR-110 baseline restorer. The CR-200-X shaping amplifier is an X- $\mu$ s gaussian shaping amplifier; it was determined that 1  $\mu$ s was most appropriate for the test bed signals.

The shaper evaluation board produced gaussian pulses from raw charge signals as shown in Figure 44.

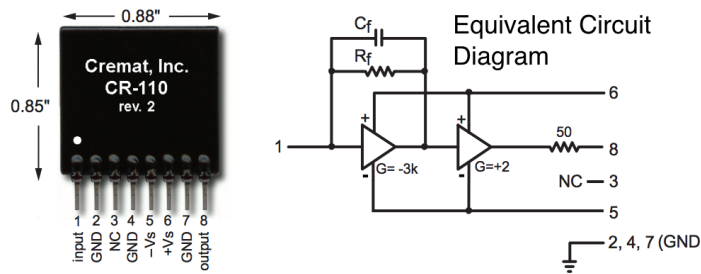


Figure 43: A picture of the CR-110 charge amplifier from the manufacturer's data sheet, shown with an equivalent circuit diagram.

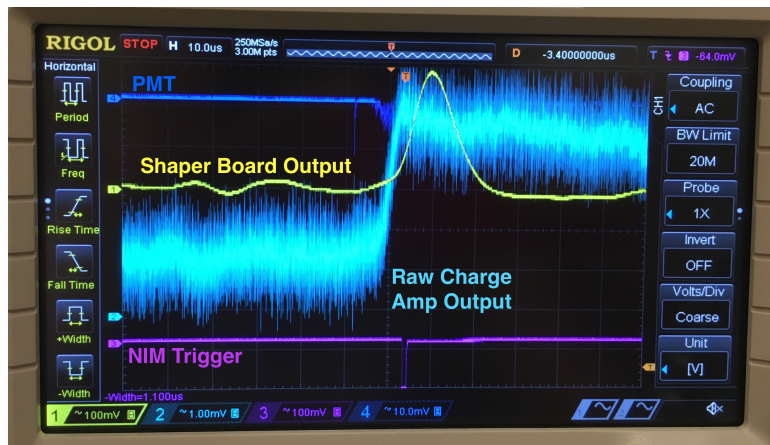


Figure 44: A raw and shaped charge amp signal taken in -100C gaseous xenon, with the radon source plumbed in

The charge amplifiers were originally placed inside the experimental vessel, mounted directly on the segmented anode. The functionality in [LXe](#) conditions didn't deviate from manufacturer's specifications, however it was found that the CR-110 units generated enough heat to create a perpetual gas layer under the anode. In general this is not an issue, but for the purpose of the intended absolute electron extraction efficiency measurement, overfilling the [TPC](#) and using the charge amplifiers as a direct read-out of electrons in the liquid was required. The charge amplifiers were moved to the outer vessel space, surrounded by a small Faraday cage made of copper mesh. See Figure 45 for the charge amplifier mounting configurations.

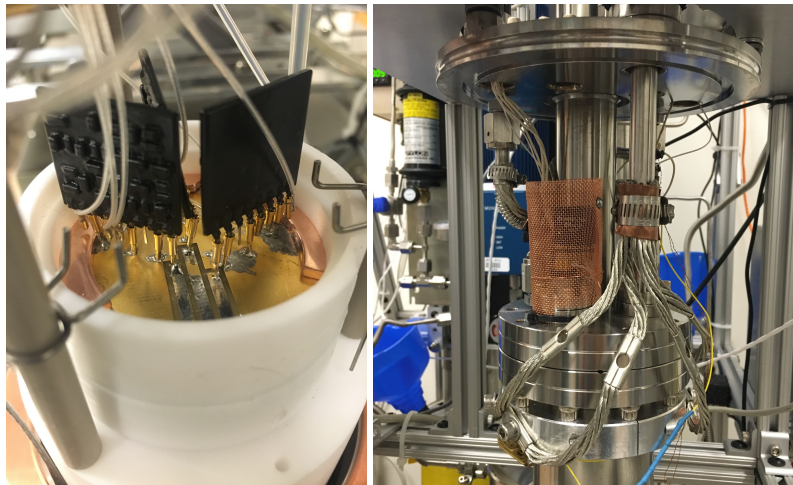


Figure 45: (Left) original mounting of CR-110 charge amplifiers inside the experimental vessel. (Right) Mounting in the outer vacuum reduced heat load on the TPC.

### 6.3.1 CHARGE AMPLIFIER NOISE BEHAVIOR

Charge amplifiers have baseline RMS noise proportional to the attached capacitance. Figure 46 shows the RMS noise of a CR-110 unit attached to different lengths of BNC cable. The longer the cable, the higher the RMS noise. [TPCs](#) are essentially capacitors, and when filled with [LXe](#) have a higher capacitance than when the detector is at vacuum. The capacitance of large [LXe TPCs](#) like [LUX](#) prohibit the use of charge amplifiers for direct readout of the S2 electrons because the RMS noise would swamp the signal.

Charge amplifiers also respond to acoustics. Tapping a finger near a charge amplifier will show as a baseline-jumping response on an oscilloscope. This additional source of noise makes [LXe TPCs](#) challenging places

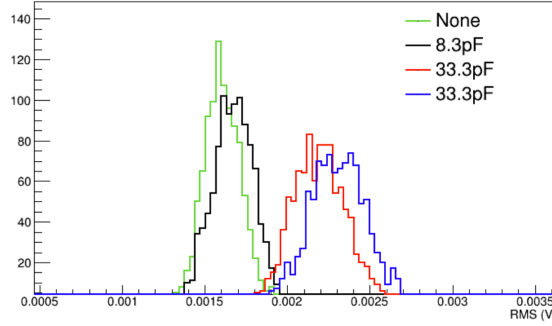


Figure 46: Different lengths of BNC cable attached to a CR-110 test board.

to use charge amplifiers for signal readout because any bubbles in the [LXe](#) create micro-acoustic signals which the charge amplifiers pick up. By design, dual phase [LXe TPCs](#) are operated near the xenon liquid-gas boundary so the formation and dissipation of gas bubbles in the liquid is likely. Additional sources of acoustic noise like circulation of xenon into the experimental vessel also produce visible responses in charge amplifiers. The difference in micro-acoustic noise environment is illustrated in Figure 47.



Figure 47: (Left) Event showing charge amp with detector -100 C, 1.5 bar, gas only. (Middle) Effect of circulation pump on charge amp is to cause 500 Hz oscillation noise (-100 C, 1.5 bar, gas only). (Right) Same event as (middle), but zoomed-in time scale.

As [TPCs](#) are large capacitors, any transients coupling to the “TPC capacitor” may be picked up by the charge amplifiers. In particular, instabilities in the [HV](#) chain induce a current in the “TPC capacitor” that is picked up by the charge amps. Instabilities in [HV](#) can come from many places. It was observed that for the characteristic capacitance and impedance of the the test bed, partial breakdowns in a length of R60 cabling caused a disruption in the functionality of the charge amplifiers. It was also found that a standard laboratory [HV](#) supply, a Glassman 20 kV negative polarity unit, created pick-up in the charge amplifiers (see Figure 48).



Figure 48: (Left) Periodic noise from the Glassman 20 kV negative polarity voltage supply. (Right) Partial breakdown in R60 cable as picked up by charge amplifiers.

## 6.4 PMT

The test bed was instrumented with an R8778 PMT, the same PMTs used in LUX. Both LUX and LZ PMT bases were used. The radon daughters study presented in Chapter 7 exclusively used the LUX PMT base, the electron trains studies first used the LUX base, and later used the LZ base. The LZ base was favored for its larger capacitors. Various shaping amplifiers were used when digitizing the PMT over the course of these studies because the 8 ns sampling interval of the data acquisition was subject to aliasing the fast-rising alpha S1 signals.

## 6.5 SLOW CONTROL

The slow control for the test bed consists of a few monitoring variables such as temperature and pressure, and a voltage supply that turns on heaters. The inner experimental vessel was instrumented with two platinum RTDs to monitor temperature and a capacitance manometer to monitor pressure. A flow meter in the circulation line determined the flow rate of xenon as it passed through the getter and returned to the inner vessel. These four variables are read using Omega i-series digital panel meters to provide a real-time display; two points of calibration are provided to the digital panel meters to translate voltage to human-readable pressure, temperature, etc. In addition, two  $25\ \Omega$  resistors are mounted, in parallel, on the cold-head. Supplying voltage to these resistors raises the temperature of the cold-head and decreases the cooling power delivered by the liquid nitrogen bath; the voltage supplied to the heaters was also recorded, but not shown with digital panel meters. The voltages for the monitoring variables and the heater voltages were fed into a USB Device from Measurement Computing, which interfaces with a computer. A slow control script on a lab computer recorded the monitoring variables and heater

voltages. The script also determined if power should be supplied to the heaters and if text message and e-mail alarms should be sent for a variable out of expected range. A basic schematic of the slow control is shown in Figure 49.

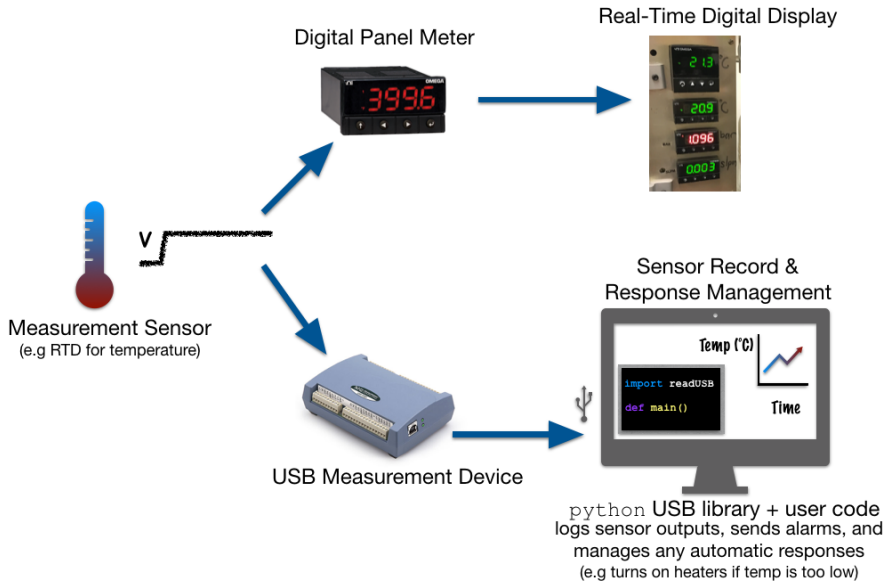


Figure 49: A diagram showing components of the slow control.

## 6.6 DATA ACQUISITION

Data were acquired with a Picoscope 5000a, a USB-compatible “oscilloscope.” The picoscope python library was used to write voltage records of PMT and charge signals to ROOT files, which were opened later for reprocessing into reduced quantities such as pulse area or pulse height. The picoscope was run as a 14 bit ADC with 125 MHz (8 ns) sampling. For special cases, when only one channel was desired, it was possible to increase the sampling rate to 500 MHZ (2 ns).

## 6.7 HIGH VOLTAGE FEEDTHROUGH DESIGN

A significant amount of time was spent developing and testing HV feedthroughs for the test bed. This section describes a few of the feedthroughs that were unsuccessful, leading to the final design, which is capable of delivering -11kV to the cathode with no observable breakdown or other effects. Extensive detail of the tests and procedures are not provided. Instead, the

following vignettes are intended as an overview to be useful to a student tasked with designing a HV feedthrough.

### 6.7.1 IMPLEMENTING SHV FEED THROUGHS FROM VACUUM SUPPLIERS

The first attempts at building feedthroughs were to use off-the-shelf products from typical vacuum supply vendors such as MDC and Kurt Lesker. Vacuum HV feedthroughs are intended to for use from air to vacuum, not air to LXe; we were attempting to operate them outside of their intended usage parameters. Additionally, by combining ceramic and metal (typically aluminum, stainless steel, nickel, copper) they are especially prone to breakdown at the meeting of these different materials, known colloquially as “triple points”. When there are interfaces between materials with different permittivities (dielectric constants), the electric fields are distorted. Electric field is “pushed” out of the higher dielectric material into the lower dielectric material. This creates a field enhancement where peak fields can be much higher than average fields in the system. The field enhancement from triple points where there is an interface between a conductor and two dielectrics (e.g conductor, ceramic insulator, and gaseous Xe) is a common source of breakdown along insulator surfaces. Good design practices, namely choices of geometry, reduce the field enhancements in these regions. With commercial feedthroughs, the geometry choice is set and may not be sufficient for the task.

Note that ceramic feedthroughs are not appropriate for low background experiments due to their high radioactivity, but for test beds, where low radioactivity is not a priority, they may be used.

The first few feed throughs used a 12kV Safe High Voltage (SHV) weldable feed though as shown in Figure 50. If used as operation is intended, the side indicated by A is used on the vacuum-side and B connects to the voltage supply. Instead, we trimmed the long B side and attached a copper, screw-port connector to make the 90 degree connection from vertical feed through to horizontal grid. This was done to avoid placing a conducting surface at high voltage (the tip of side A) in gaseous xenon, thereby increasing the risk of breakdown to the walls of the detector. The feed through’s vertical placement is designed such that the copper connector is fully submersed in LXe (Figure ??).

Feed throughs were tested by performing a cool down, ramping the HV supply slowly, and watching an oscilloscope for a higher than baseline photon rate (Figure 53) or a full xenon breakdown (Figure 54). The effect of raising the voltage on the HV supply at a specific rate was also tested, and it was determined that the extremely slow and steady rate of a computer program was not necessarily superior to the imperfect method

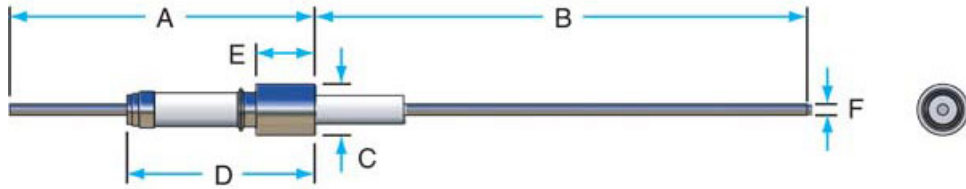


Figure 50: A 12kV SHV weldable connector from vacuum supplier Kurt Lesker.



Figure 51: (left) The copper tape in this picture is sitting on top of a 1/2 -in swage connector. The swage connector captures a 1/2 in pipe, which has the 12 kV SHV feedthrough welded to the end. (right) 12 kV SHV weldable connector, inverted, clipped, and attached with a machined copper connector. The connector uses a screw to capture the SHV feed though, and the same screw to capture a stranded wire, visible in this picture, which is then fed through a hole drilled in the PTFE to connect to the wire grid frames. The wire was wrapped around the grid frame.

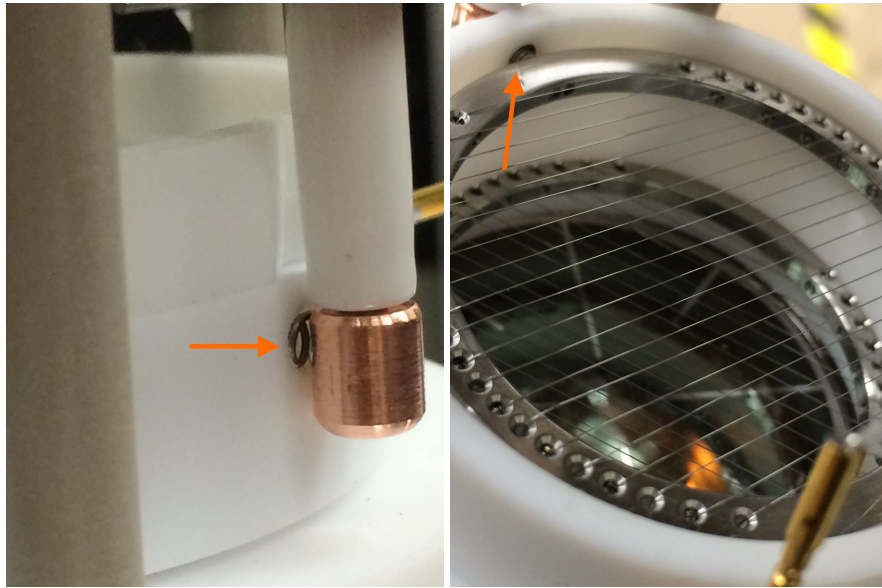


Figure 52: The same 12kV SHV feed through, now with a modified spring connection connecting the feed through to the grid frame. A close up of the cathode grid showing the spring connection is on the **right**

of the human experimenter – the construction of the feedthrough, itself, outweighed any gains from computer-supervised voltage ramping.

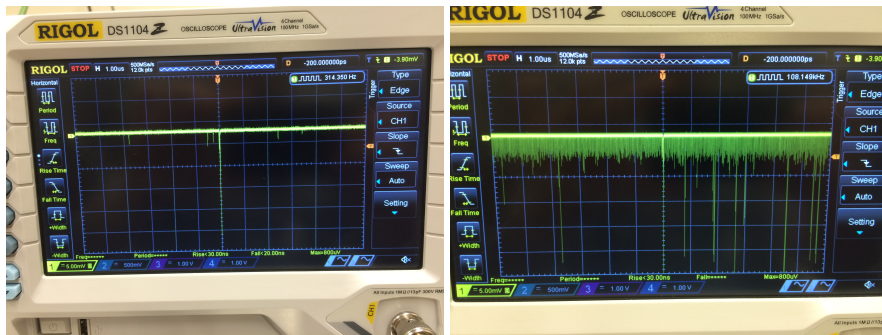


Figure 53: Oscilloscope showing baseline rate of single photons (left) compared to a high rate of single photons (right) caused by the high voltage feed through.

Iterations of the 12 kV SHV feed though were not able to reach and sustain more than about 7 kV for extended periods of time like those that would be required for data acquisition.

We also tried a stock 20 kV SHV feed through with a custom end cap designed by HV engineer Will Waldron, meant to smooth out typical triple point issues. This feed through was mounted on a CF flange far from the active region. A length of cable was stripped of grounding sheath for its

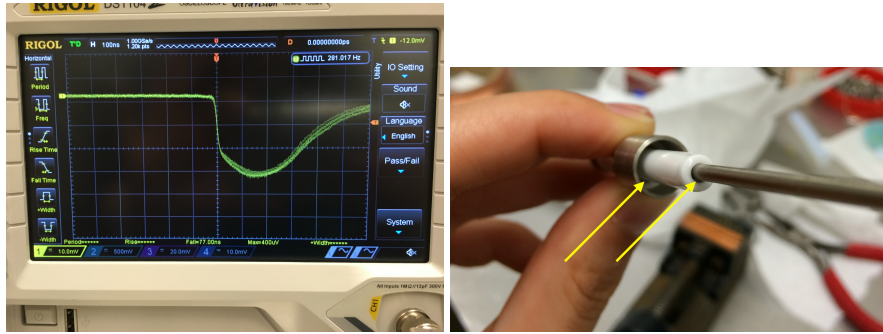


Figure 54: (Left) Full xenon breakdown as visible on the PMT trace. The large, saturated pulse is caused by the high intensity of light. This type of breakdown was often accompanied by an audible buzz, and a rise in current that would initiate a trip of the high voltage supply. (Right) a close up of the xenon-facing side of the feedthrough. Visible gaps where xenon gas is exposed to high fields are particularly problematic for breakdowns.

entire length. A small section on one end was stripped of dielectric, this end was tied to the SHV feed though with copper wire, and the custom end cap was placed over this. The side of the cable making the connection to the cathode grid was drilled out for a short length on the bottom, leaving only a tube of dielectric with no conductor. A threaded rod was inserted into the cable, such that the rod made contact with the conductor. The cathode grid frame was screwed onto the threaded rod. The SHV-20 feed though is summarized in pictures in Figure 55, and was found to hold sufficient voltage (10 kV) for extended periods of time. However, it was found that the voltage capability of this feed though decreased over time; this is discussed in the next section.

#### 6.7.1.1 FEEDTHROUGH AGING

It was noticed during subsequent operation that the SHV-20 feed through was subject to some sort of aging process (black line in Figure 57). A month of use resulted in noticeably lower voltage capabilities. The issue could have been any point along the entire voltage chain: feed through - custom cap - connection to cable - cable - connection to grid - grid. Tests focusing on different parts of the voltage chain didn't reveal any weak points. Instead, it was found that the SHV-20 feed though, itself, was subject to aging (red line in Figure 57).

Feedthrough aging can be the result of arcing and discharges which cause local heating and carbonization of an insulator surface. Once there is a carbon path, the insulator is considered "tracked" and then holds a much lower voltage than before. Sophisticated HV systems keep peak cur-

## 6.7 HIGH VOLTAGE FEEDTHROUGH DESIGN

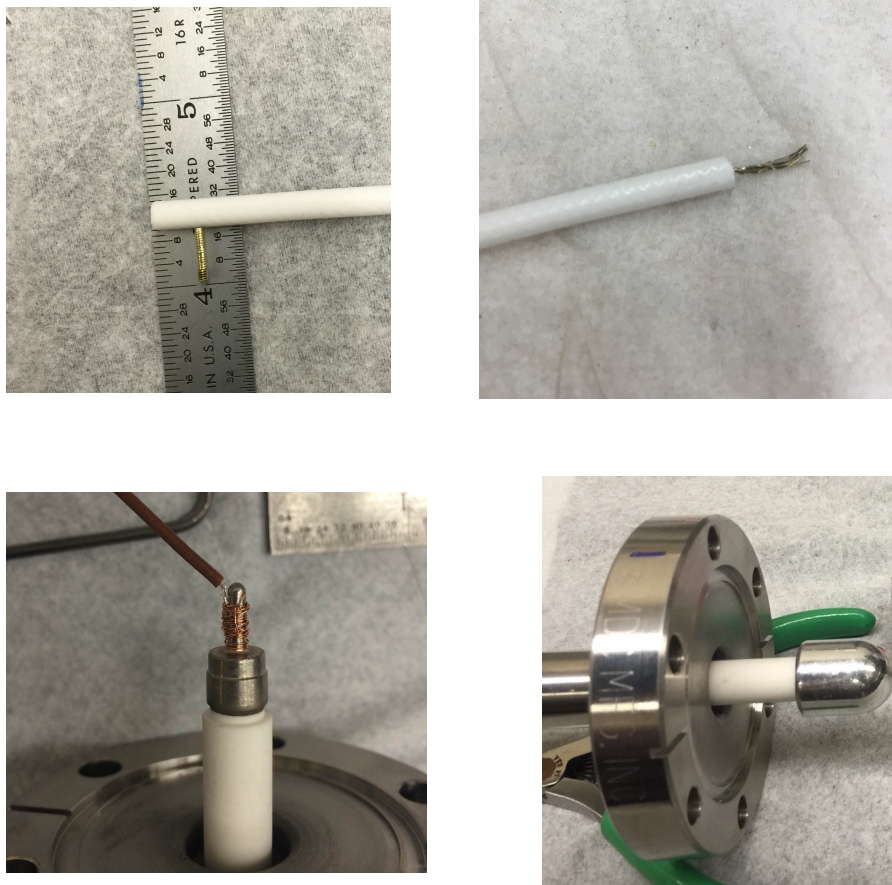


Figure 55: Top: (left) cathode connection side (right) SHV-20 connection side  
Bottom: (left) an example showing how the cable was attached to the stock SHV-20 feed though end (right) a custom cap fit over the connection, smoothing out triple points.



Figure 56: Effect of holding the feed through in place with PEEK zip ties was explored, effects were minimal.

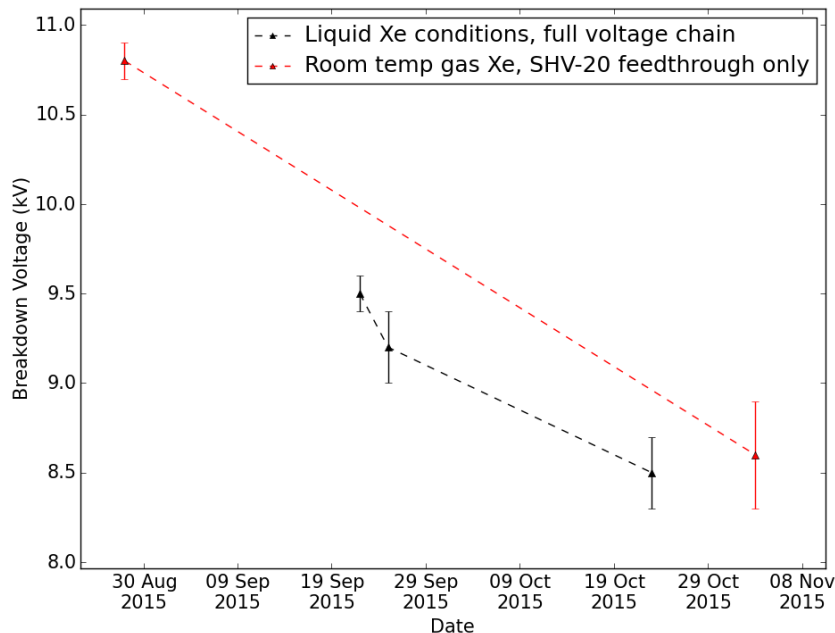


Figure 57: The black line shows the aging observed in the course of normal operations. The red line shows breakdown tests of the SHV-20 feed through in gas, illustrating that the aging observed during operation was due to aging of the feed though.

rents and fault energies to a minimum using series resistors. In this way, a breakdown event does not degrade system performance in the future. In addition to carbon tracks, there can also be insulator degradation from exposure to UV if there is ionization in the region. Xenon ionization is in the UV region of the spectrum, and so any ionization near a feed through insulator may degrade the feed through performance. In the case of this particular feed though, the high field which caused the breakdowns or ionization was likely a result of poor triple-point geometry.

## 6.7.2 CUSTOM FEEDTHROUGHS

To achieve better voltage performance, we moved away from typical, stock feedthroughs composed of ceramic and metal. Figure 58 shows a feed through made with a Swagelock reducing union. This blue and white PTFE piece connects 1/4 in SS pipe to an 1/8 in PTFE tube, which then houses a SS rod. The rod is screwed onto a connector, which holds a wire to connect to the grid. This feed through had stable voltage performance, but could not achieve sustained voltages higher than about 9 kV. A woven SS shield was added to the feed though to reach higher voltages (Figure 58 (left)) but this actually decreased the voltage performance to a maximum of about 5 kV.

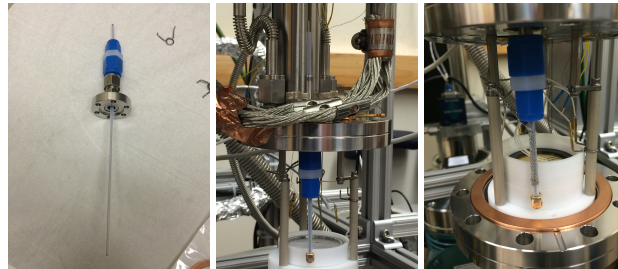


Figure 58: First attempt at a custom feed through built out of Swagelock parts combined with basic materials like PTFE and stainless steel rods. The orientation shown (left) was later inverted due to concerns of temperature stress and pressure stress on the PTFE ferrules. The feedthrough as assembled (center) was functional, but higher voltage capability was desired. The effect of adding a grounding braid (right) was found to decrease the voltage capability instead of increasing it.

There are two issues with the approach of adding a grounding braid in this method: (1) the braid is not tight to the dielectric, which introduces peak fields between the dielectric and the braid (Figure 59) (2) at the braid termination, a small effective radius creates an enhanced radial field through the dielectric and an enhanced field along the cable dielectric facing the high voltage. Peak fields can occur in unexpected places, greatly

decreasing the voltage capability of a feedthrough that seems, naively, robust. The breakdown field of xenon gas depends on a variety of factors such as temperature (i.e density), purity, electrode shape, etc. Peak fields arising in gas regions in or around HV feedthroughs are sources of unwanted light and in the worst case complete breakdown and eventual degradation of the feedthrough.

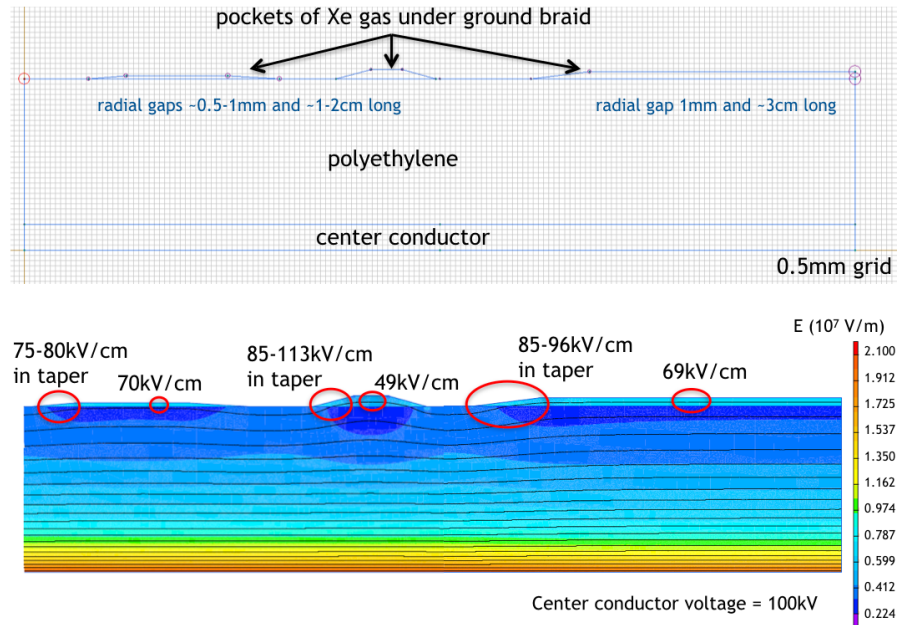


Figure 59: (top) Input to a COMSOL model simulating gaps between the grounding braid and dielectric of a high voltage feedthrough. (bottom) COMSOL output the model, showing that peak fields arise when gaps exist between dielectric and grounding braid.. Both images provided by high voltage engineer W. Waldron.

Due to the poor performance of custom feedthrough, and concerns about the cold connection, a feedthrough was built out of a SS rod with PTFE dielectric and no shield braid (Figure 60) that enters the inner vessel from the top of tall CF tower, where the connection is warm. The end is a copper rod bent into a U-shape which connects to the SS conduction rod via a pin, and the other end, which is threaded, screws into to the cathode grid frame. The bare copper section is only exposed under the liquid level, elsewhere the PTFE dielectric helps contain the electric field and prevent breakdown to the inner vessel wall. This feedthrough had good voltage performance, and there was no sign of aging. It was decided, however, that the charge amplifiers were more susceptible to detecting transients from an unshielded feedthrough, so another feedthrough with shielding was constructed (Figure 61). This feedthrough has an outer PTFE sheath to keep the shielding tight against the inner dielectric. This

## 6.7 HIGH VOLTAGE FEEDTHROUGH DESIGN

final feedthrough design was extremely successful, and has been in use for 2 years at the time of writing this thesis.

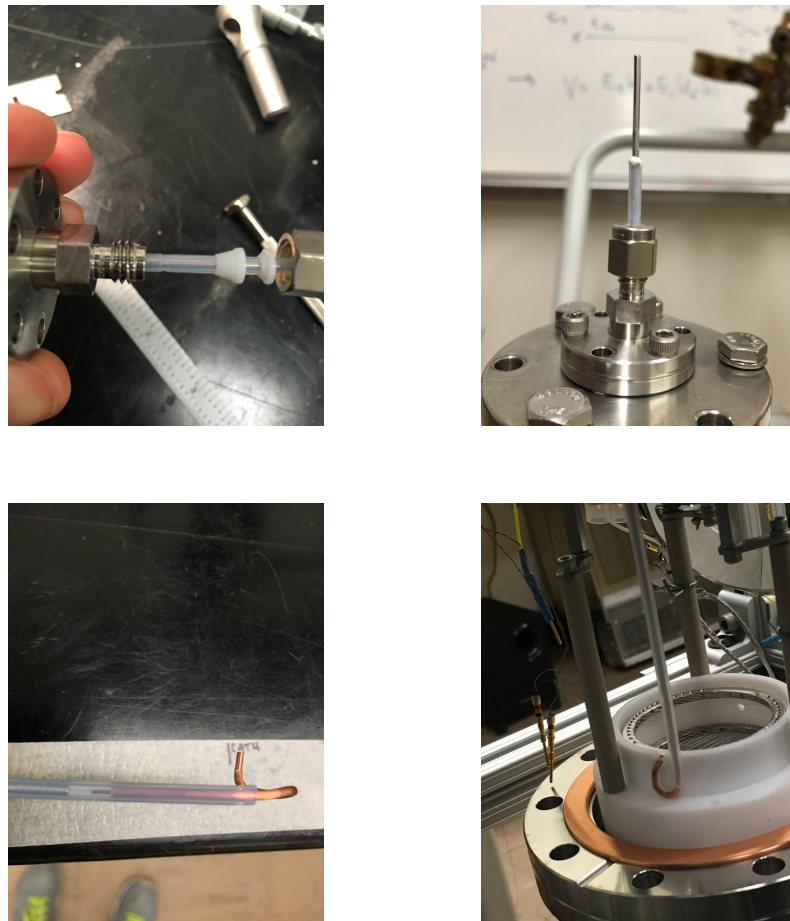


Figure 60: Top: (left) Close up showing the PTFE ferrules and notch. (right) Close up of the sealed top connection; epoxy was added to prevent leaks between the dielectric and conductor rod . Bottom: (left) Threaded U-bend cathode connector (right) Feed through assembled and installed.



Figure 61: Top: (left) Sealed top connection with liberal epoxy use. A male Bendix pin was soldered to the cable conductor. (middle) SHV connector with female Bendix to mate with feedthrough (right) Grounded safety housing with SHV connector. Bottom: (left) Ends of the feedthrough were held in the Teflon stack. (middle) Close up showing cable conductor, PTFE dielectric, and grounding sheath pulled back (right) Grounding scheme for feedthrough cables.

# 7

## SOLUBILITY OF RADON DAUGHTERS IN LIQUID XENON

---

Rare-event searches are very sensitive to backgrounds from radioactivity in and on detector materials. Some of the most omnipresent and troublesome are  $^{222}\text{Rn}$  and its daughters. Decay products from  $^{222}\text{Rn}$  plate out on detector surfaces and have typically been assumed to be fixed there. In this chapter, a series of experiments is described; the results provide evidence that radon daughters can dissolve in liquid xenon.

### 7.1 MOTIVATION

Radon and radon daughters produce problematic backgrounds for rare-event searches [47]. Of particular concern for liquid xenon dark matter detectors are “naked” beta decays. These ground-state to ground-state decays have no accompanying gammas and cannot be rejected via coincidence tagging. Rejection of these backgrounds in WIMP search experiments relies solely on being able to discriminate electron recoils from nuclear recoils. For example, the ER leakage fraction from the LUX Run03 tritium calibration is on the order of 2/1000 over the WIMP search region [**LUX:Tritium**] (See Chapter ?? for more details). The  $^{222}\text{Rn}$  chain contains  $^{210}\text{Pb}$  ( $T_{1/2} = 22.23\text{ y}$ ), effectively splitting the decay chain into a “fast chain” and “slow chain” (Fig. 62). Radon can be introduced via two pathways: (1) during detector construction and (2) during detector operation (see Fig. 63). Great care is taken to ensure minimal contamination via pathway 2 because the fast chain naked betas,  $^{214}\text{Pb}$  and  $^{214}\text{Bi}$ , may decay in the fiducial volume before the purification system can remove them or before they can plate out on detector surfaces. In pathway 1,  $^{222}\text{Rn}$  and daughters plate out onto detector surfaces during construction of parts, and construction of the detector itself. Models for plate out can be found in [73] and [74]. Typically it is assumed that once  $^{222}\text{Rn}$  and daughters plate out, they remain fixed at that position, and can be rejected by a fiducial volume cut. This means that the slow chain naked betas of  $^{210}\text{Pb}$  and  $^{210}\text{Bi}$  from initial exposure during construction are assumed to occur outside the fiducial volume. However, evidence of  $^{210}\text{Bi}$  mobility has been

observed in the liquid scintillator environment of KamLAND [75], [76] and Borexino [77]. If radon daughters are soluble in liquid xenon, the late chain naked betas (from both pathway 1 and 2) pose a serious background distributed throughout the fiducial volume.

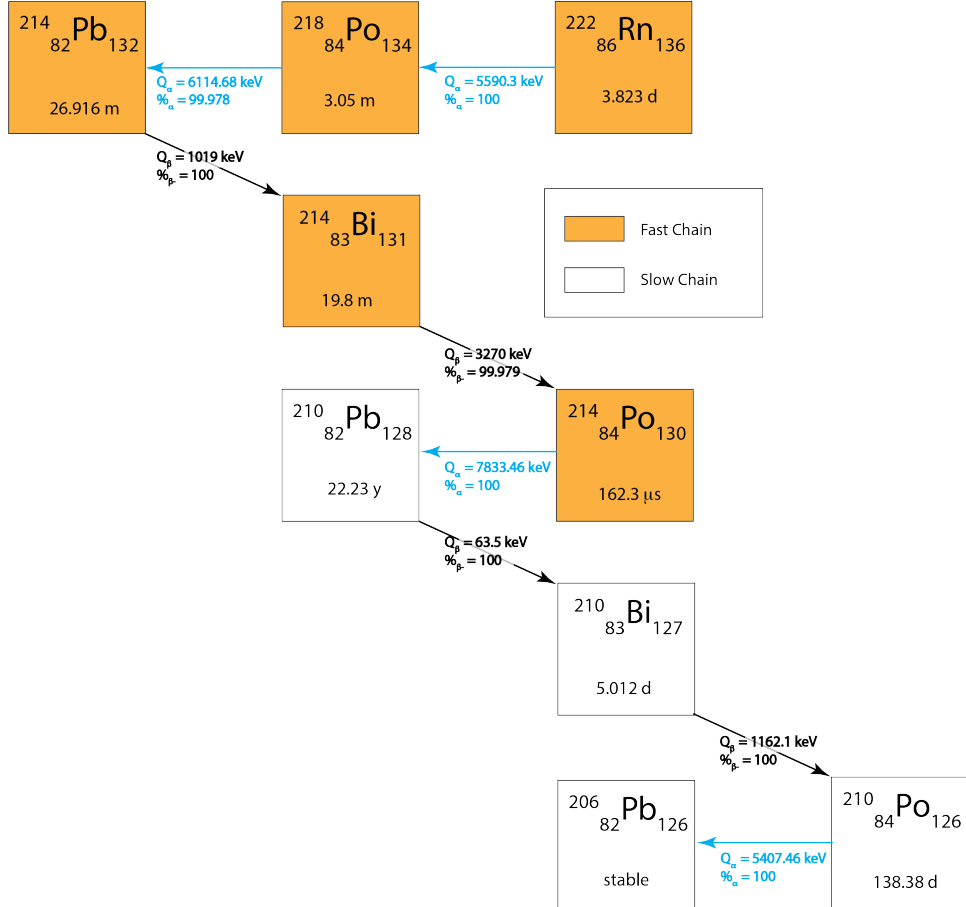


Figure 62: The  $^{222}\text{Rn}$  decay scheme. The fast and slow chains are indicated.

In order to investigate the solubility of radon daughters in liquid xenon, a  $^{220}\text{Rn}$  source was employed. The analogous long lived daughter in this chain,  $^{212}\text{Pb}$ , has a half-life of 10.6 h, making it appropriate for a laboratory test. Investigating pathway 2 in the laboratory by introducing radon in a  $\text{LXe}$  environment will necessarily yield inconclusive results, because it is impossible to tell if the daughter decay of interest plated out before decaying. Therefore, we required the radon daughters to be on a surface.

Xenon gas was circulated through the  $^{220}\text{Rn}$  source and detector components for a period of >24 h. The detector was then evacuated, thereby assuring the initial position of radon daughters on a detector surface. Any radon daughters subsequently observed in the bulk region after condensing liquid xenon must therefore have dissolved.

## Pathways to Radon and Radon Daughters Contamination

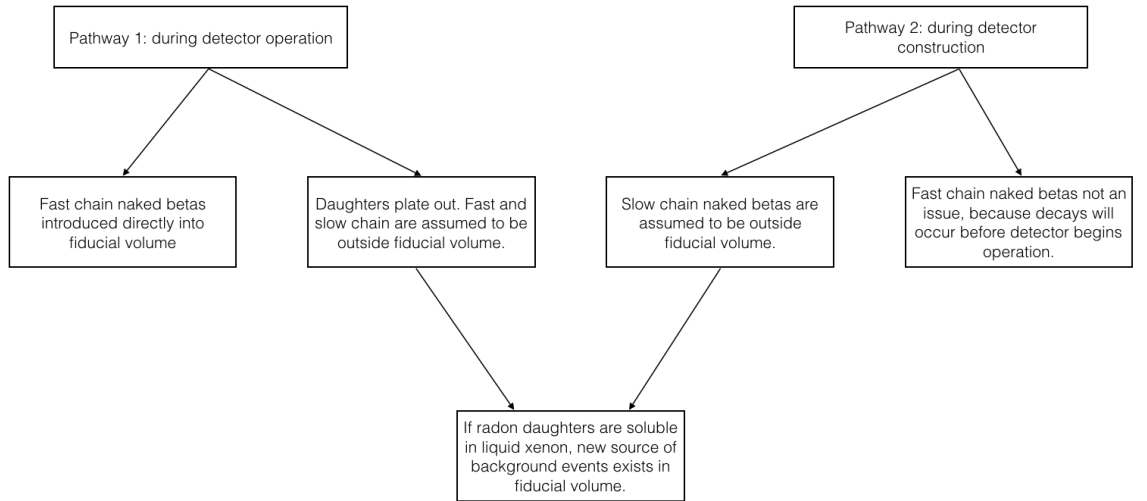


Figure 63: Pathways to radon and radon daughter contamination.

### 7.1.1 PLATE OUT

The term “plate out” is used above but not defined. The literature indicates that there two known types of radon daughter plate out [78]. The following terms are used in [78] to identify each type.

1. *implantation* Alpha recoil implantation of a daughter nucleus
2. *sticking* Daughters are sitting on the surface of a material, it is possible to wash a percentage of these off with various surface cleaning methods.

The percentages of daughters plated out in these different modes are not indicated, but [78] relates a story of researchers being unable to remove  $^{214}\text{Po}$  from glass samples, where as  $^{218}\text{Po}$  was easily removed with surface cleaning methods. This is explained by the fact that further down the  $^{222}\text{Rn}$  chain, more alpha decays have occurred, so a late-state daughter has had more chance to be implanted. It is also noted that the durability of the implanted activity subject to change under different conditions, as is the implant integrity. The author cites factors such as humidity and temperature affecting whether daughters implant, and whether they remain implanted; since the conditions for plate out are different in pathways 1 and 2 and it logical to infer that implantation functions differently in these two environments for LXe TPCs.

The chemistry of radon has been studied as well, and may provide some context to the plate-out discussion. Radon is frequently regarded as a totally inert element. It is, however, classified as a “metalloid”, and exhibits some of the characteristics of both true metals and nonmetals. For example, it is known to react chemically with fluorine, halogen fluorides, dioxygenyl salts, fluoro-nitrogen salts, and halogen fluoride-metal fluoride complexes to form ionic compounds [79]. It is also known to co-crystallize with hydrogen chloride, hydrogen sulfide, sulfur dioxide and carbon dioxide [80]. In the latter case, the author notes that the radon is not forming true chemical bonds, but rather is held in place by weak Van der Waals forces. These chemical experiments found radon to be readily reactive at “room temperature and lower”, but the low temperate range is not stated. Chemical bonds formed by radon may make up a different type of plate out, or sub-type of ‘sticking’. Presumably weak surface Van der Waals forces belong in the ‘sticking’ type as well.

If we look to surface physics, the plate-out term ‘sticking’ is well defined by the terms physisorption and chemisorption. Physisorption is distinct from chemisorption in that it is a general phenomenon occurring between the adsorbed atom and surface, where chemisorption involves a chemical reaction between surface and adsorbate, and is characterized by higher bond strengths. Chemisorption potentials have been calculated for many atoms and surfaces [81] and are generally greater than 1 eV. Physisorption potentials, such as the well-known Van der Waals potential, are less than 1 eV and as low as 10 meV.

Plate out occurs with different rates on different materials [82], and can be an order of magnitude larger on PTFE than stainless steel, likely due to PTFE’s tendency to accumulate negative static charge [83]. Plate out of radon daughters can be reduced by employing a nitrogen gas purge or an electric field (approximately 90% of radon daughters are charged) [84]. However, [82], [83], and [84] do not distinguish between implantation and sticking, and only use the term “plate out”.

## 7.2 EXPERIMENTAL CONFIGURATION AND METHOD

A diagram of the TPC for this work is shown in Fig. 64. A 50 mm diameter cathode wire grid, extraction wire grid, and a planar, segmented anode were held in Teflon PTFE housing. The anode was instrumented with charge-sensitive preamplifiers. Both grids were constructed from a stainless steel frame strung with 4  $\mu\text{m}$  diameter stainless steel wire on a 2 mm pitch. The xenon inlet was a PTFE tube which introduced xenon gas into the liquid region where it was condensed. The xenon liquid outlet was a thin stainless steel capillary that drew liquid from the TPC into the

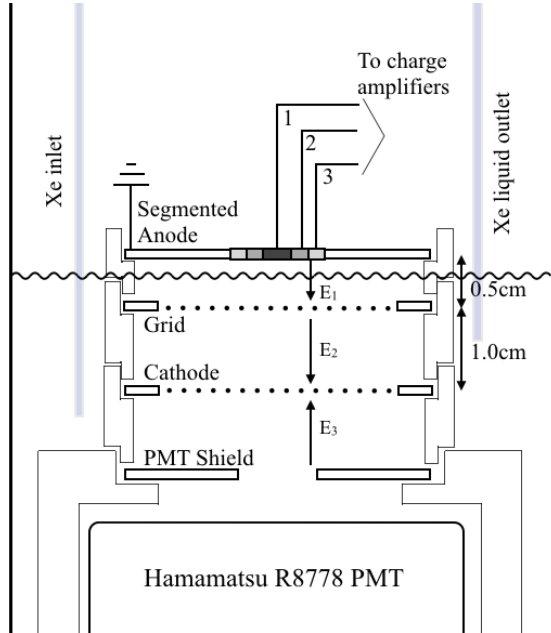


Figure 64: Diagram of the test bed. For this study, the cathode is held at -6.0 kV, and the grid is held at -4.0 kV.  $E_1^{liq} \approx 5.0$  kV/cm,  $E_1^{gas} \approx 10.0$  kV/cm  $E_2 = 1.0$  kV/cm.  $E_3 = 2.7$  kV/cm. The large gray regions represent the structural rings of PTFE. The line between the grid and anode represents the liquid xenon level. The xenon inlet pipes incoming gas directly into the liquid region, and the liquid outlet pulls from the level of the active region. A gas outlet (not pictured) also draws xenon gas into the circulation system to be purified.

purification system. Both inlet and outlet tubes were placed near holes drilled in the PTFE to aid circulation into the active volume.

A particle interaction in the liquid xenon volume produced primary scintillation photons (S1) and ionization electrons. The ionization electrons were drifted with an electric field into the gas phase, where they produced secondary scintillation light (S2). A single Hamamatsu R8778 VUV-sensitive PMT was installed in Teflon PTFE housing, facing upward to view the active region. Directly above the PMT was a copper shield mask, held at the same voltage as the PMT bias of -1250 V.

The TPC was filled with 1.5 bar of xenon gas at room temperature. The gas was circulated continuously through the TPC and a heated zirconium getter for at least 24 hours to remove contaminants. The TPC was then cooled to  $-100^\circ$  C while circulating xenon gas. Circulation was stopped, and xenon was condensed into the TPC until the liquid level rose to between the extraction grid and anode. The process of filling the TPC took 4 to 5 hours. The liquid level was kept stable by keeping the temperature and pressure constant in the TPC. During data collection, xenon from the

TPC was circulated through a getter and re-condensed into the TPC to remove impurities.

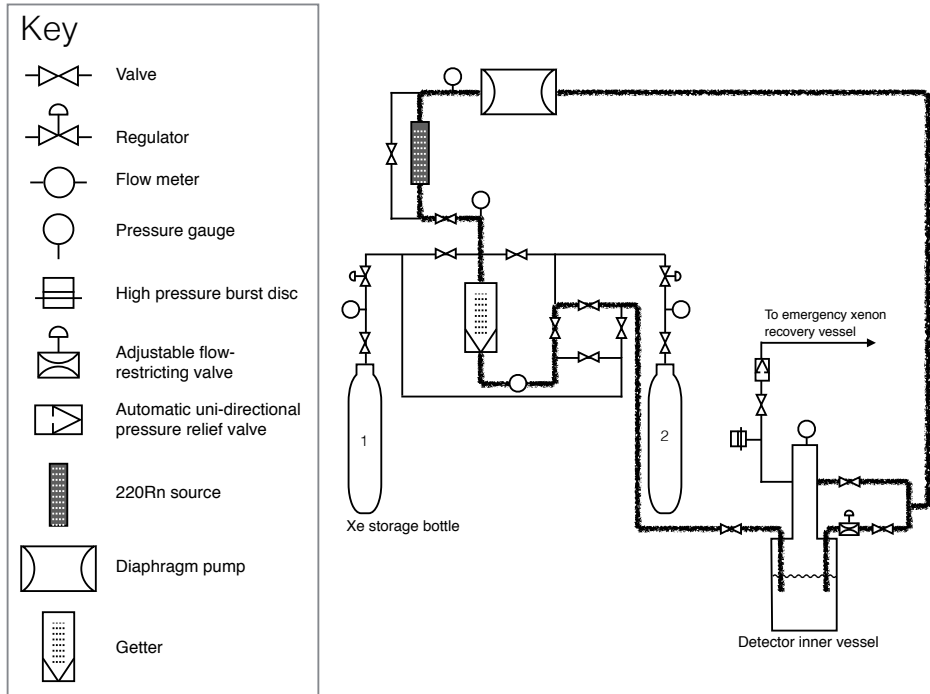


Figure 65: An example a circulation path used for plate out is shown on the pumping and instrumentation diagram. During data-taking the radon source was bypassed. The typical liquid level is indicated on the diagram to show that the outlet drew from the liquid via a capillary, ensuring purification of the liquid xenon. A gas purge also purified the gas column in the detector.

### 7.2.1 PLATE OUT OF $^{220}\text{Rn}$ DAUGHTERS

The procedure to plate out  $^{220}\text{Rn}$  daughters on the inner surfaces of the detector was the same as described in Sec. ??, except that the circulation path was directed through a 2 kBq  $^{220}\text{Rn}$  source. The  $^{220}\text{Rn}$  is shown in Fig. 66. The rate of radon activity in the TPC was measured to be  $4.5 \pm 0.5$  Hz during plate out. The total alpha rate was measured by taking repeated 1200 ms traces on an oscilloscope of the PMT with a falling edge trigger and counting the alpha decays. This rate was then halved to get the rate of radon decays. The  $4.5 \pm 0.5$  Hz rate of radon activity represents activity for all of the space internal to the PTFE support structure. Decay daughters diffused until they contacted a wall or other surface, where they could plate out. Some percentage of decay daughters are expected to be positively charged ions. If the cathode grid was biased, charged decay

daughters drifted preferentially to the cathode grid. The cathode voltage during plate outs is noted in Table 1.

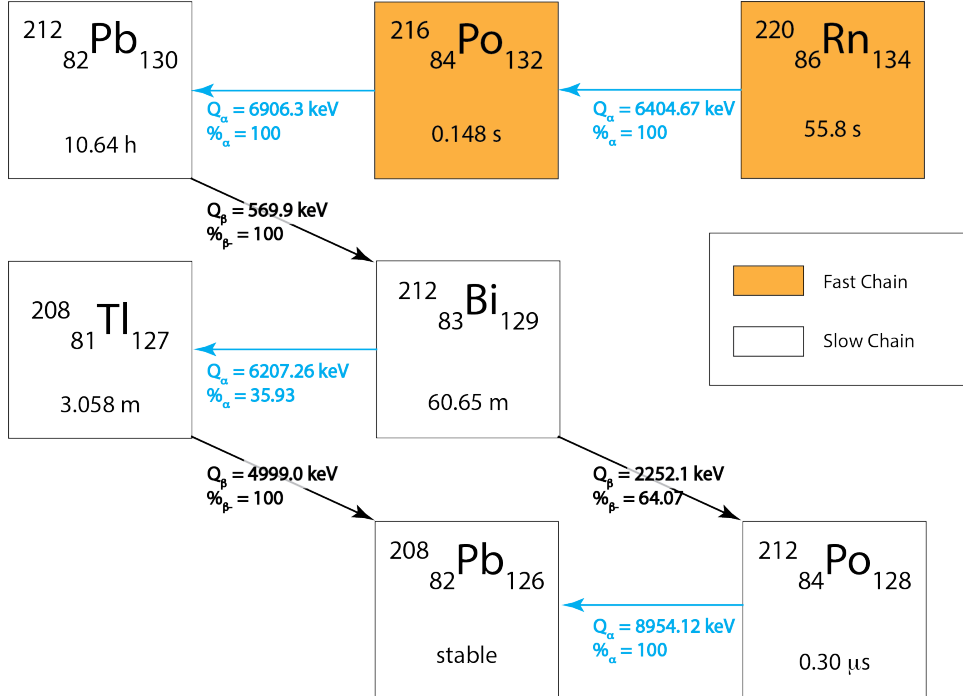


Figure 66: The  $^{220}\text{Rn}$  decay scheme. The fast and slow chains are indicated. Events in the plate out data sets are from the slow chain.

Prior to filling the TPC with liquid xenon, the circulation was stopped and the xenon gas removed from the TPC and the circulation lines. A vacuum pressure of a few  $10^{-4}$  Torr was achieved in a period of ten minutes. This step ensured removal of  $^{220}\text{Rn}$  and decay daughters which are dissolved in the gas, leaving only those daughters which had plated out on a detector surface. Since the fill time of the TPC is 4 to 5 hours, there were no fast chain alpha decays of  $^{220}\text{Rn}$  and  $^{216}\text{Po}$  in the plate out data. Additional details are summarized in Table 1.

## 7.2.2 DATA COLLECTION

Voltage records from PMT and charge channels were collected with a 14-bit ADC with 125 MHz sampling and a 20 MHz low-pass filter. The trigger was a coincidence between the PMT and the central anode segment, used to select events in the central ( $r < 3 \text{ mm}$ ) column of xenon. This avoids any electric field fringing effects.

	dataset ID	A	B	C	D
Plate-Out	Circ thur $^{220}\text{Rn}$ Source	yes	yes	no	-
	Circulation Time (h)	24	48	24	-
	Cathode Voltage (kV)	-1	0	0	-
Data-Taking	Circ thur $^{220}\text{Rn}$ Source	no	no	no	yes
	Cathode Voltage (kV)	-6	-6	-6	-6
	Grid Voltage (kV)	-4	-4	-4	-4
Livetime (h)		$12.02 \pm 0.5$	$23.93 \pm 0.5$	$25.02 \pm 0.2$	$4.15 \pm 0.2$

Table 1: Summary of plate out and data-taking conditions. Data sets A and B are taken after circulating radon gas and data set C, background, had no radon circulation. Data set D was taken following dataset A, and radon was circulated in a liquid xenon environment, purposefully introducing radon into the detector bulk to calibrate the detector.

### 7.2.3 CALIBRATION

In order to identify a signal region for bulk radon daughters, the flow through  $^{220}\text{Rn}$  source was employed directly following dataset A, allowing  $^{220}\text{Rn}$  to flow into the liquid bulk of the TPC. The bulk daughter decay of interest,  $^{212}\text{Bi}$  alpha, has an energy approximately equal to the  $^{220}\text{Rn}$  alpha decay. The alpha signals were sufficient to saturate the biasing circuit of the PMT, so alpha decays within 1 MeV of each other were indistinguishable. Therefore, the region in S1 area vs. S2 area where the  $^{220}\text{Rn}$  alphas appeared was also where  $^{212}\text{Bi}$  alphas were expected (Fig. 71).

### 7.2.4 POSITION RECONSTRUCTION

The central anode segment was assumed to select events from the central column with 100% efficiency. Events occurring under one of the outer concentric segments can produce a signal on the central anode, but the signal was largest at the anode nearest the charge. It was not required that there be zero signal on the outer segments, so the (x,y) position of the event is treated as a source of uncertainty, which is taken into account in the calculation of fiducial volume. The drift time of the events was

calculated from the time difference between the S1 and S2 pulses, and a linear scaling of 2 mm/us was applied using the Miller (1968) electron drift velocity in LXe measurements.

### 7.2.5 FIDUCIAL VOLUME

Different values for the fiducial volume are presented below.

---

Anode Segments	1	2	3	Full
Radius (mm)	3	6	9	24
Area (mm <sup>2</sup> )	28	113	255	1810
Volume (mL)	0.39 ± 0.03	1.6 ± 0.1	3.6 ± 0.3	25.3 ± 1.8
Mass (g)	1.1 ± 0.1	4.6 ± 0.3	10 ± 1	73.4 ± 5.2

---

Table 2: Calculations of fiducial volume. Liquid level is taken to be 14 ± 1 mm. Density of LXe near boiling point is 2.9 g/mL.

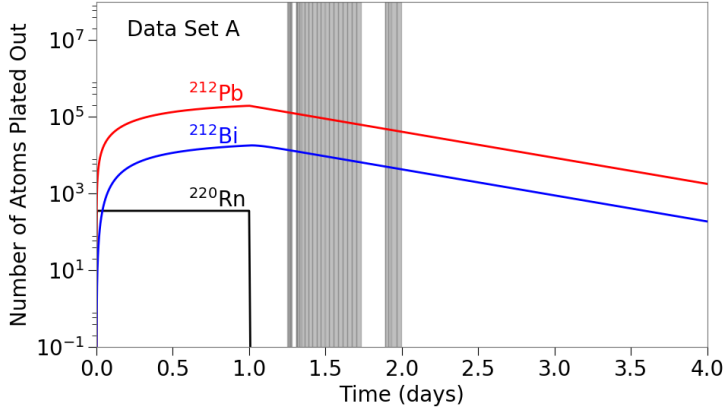
## 7.3 ANALYSIS

### 7.3.1 NUMBER OF $^{220}\text{Rn}$ DAUGHTERS IN THE TPC

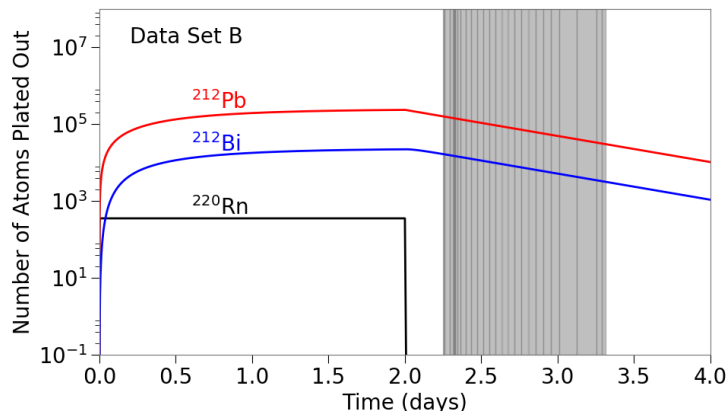
As described in Sec. 7.2.1, the rate of  $^{220}\text{Rn}$  in the TPC was measured to be  $4.5 \pm 0.5$  Hz during plate out. From this, the number of daughter atoms  $^{212}\text{Pb}$  and  $^{212}\text{Bi}$  present in the TPC just prior to filling the liquid xenon were calculated. The number of daughter atoms as a function of the plate out time is shown in Fig. 67 along with the data acquisition periods for each dataset. This calculation assumes that the diffusion time in the PTFE walls was less than removal time via the capillary.

### 7.3.2 DATA SELECTION

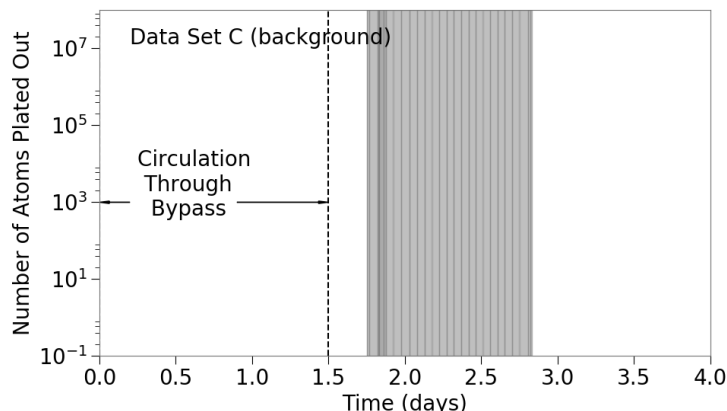
The trigger described in Sec. 7.2.2 captured the slow chain decays as shown in Fig. 66. The  $^{212}\text{Bi}$  beta decay is followed by the 300 ns alpha decay of  $^{212}\text{Po}$ ; these decays are referred to herein as “Bi-Po”.



(a)



(b)



(c)

Figure 67: a) and (b) and (c) show the plateout conditions of datasets A, B, and C, respectively. The gray bands indicate time when data was being acquired. Dataset D (calibration) was taken following dataset A and consisted of a few hours.

The aim of this analysis was to reconstruct the z-position of radon daughter alpha decays via the timing difference between the S1 and S2 of an event. Therefore, Bi-Po events were rejected, as the two S2s presented a timing ambiguity. The focus was instead on identifying  $^{212}\text{Bi}$  alpha decays. All events were expected to take place on detector surfaces, so  $^{212}\text{Bi}$  alpha decays in the drift region indicate mobility of plated-out daughters  $^{212}\text{Pb}$  and/or  $^{212}\text{Bi}$ ; it was not possible to determine whether the original position was on the cathode wires, PTFE walls, or other detector surface.

The software cuts used to select  $^{212}\text{Bi}$  alphas are described below:

1. **Data Cleaning** Remove events with any railed charge channel.
2. **Fiducialization** Require more signal in the central anode segment than the other two concentric anode segments.
3. **Select Alpha Events** The tallest pulse in an event was required to be an S1. Alphas are higher energy than the other decays in the  $^{220}\text{Rn}$  chain, and have a characteristically high light yield, so this cut is generous in keeping all alpha events.
4. **Reject Bi-Po Topology** Of the alpha events, those with one S1 and one S2 (single-scatter) were classified as  $^{212}\text{Bi}$  alpha. Events with two S1s (one of which is alpha-like), and one or two S2s were classified as Bi-Po.
5. **Reject Bi-Po Energy** There are two ways a Bi-Po event can mimic the topology of  $^{212}\text{Bi}$  alpha: (i) alpha decay was prompt and so the scintillation signals from the beta and alpha were combined into one large S1 (ii) the beta was ejected into the cathode wire and therefore there was no signal detectable from the beta. To robustly identify  $^{212}\text{Bi}$ , the alpha S1 areas of  $^{212}\text{Bi}$  alpha and Bi-Po events from Step 2 were histogrammed and fit with Gaussian functions.  $^{212}\text{Bi}$  alpha events were tightly selected with a high and low S1 area cut placed on single-scatter alpha events: anything above  $(\mu - 3\sigma)_{\text{Bi-Po}}$  was considered a Bi-Po event and anything below  $(\mu + 3\sigma)_{\text{Bi-alpha}}$  was considered a beta or gamma, and discarded (Fig. 68). It should be noted that this cut doesn't affect the signal region for  $^{212}\text{Bi}$  alpha in bulk; it affects the region for  $^{212}\text{Bi}$  alpha on the cathode. This cut is conservative in discarding Bi-Po events, as this leads to a more conservative fraction for dissolved fraction of  $^{212}\text{Bi}$  alphas.
6. **Z-position Cut** Events in the cathode region were separated from events in the bulk region with a z-position cut (discussed further below).

7. **Bulk Signal Area Cut** Only  $^{212}\text{Bi}$  alpha tagged events which also fell in a signal region expected from calibration with the  $^{220}\text{Rn}$  flow though source (Fig. 71h) were considered to be daughters which have dissolved.

In order to choose the value for the z-position cut in Step 4, a Monte Carlo approach was used. A Bi-Po decay with a prompt alpha (appears as single-scatter) where the beta penetrates into the bulk region, could mimic a  $^{212}\text{Bi}$  alpha bulk event. To better understand Bi-Po cathode events and the danger of mis-identifying them as  $^{212}\text{Bi}$  alphas in bulk, a Monte Carlo study was done with the  $^{212}\text{Bi}$  beta spectrum (the highest energy beta in the  $^{220}\text{Rn}$  chain) to determine the maximum distance a beta could penetrate into the bulk region. The study yielded a maximum beta penetration of  $z_{max,MC} = 0.12$  cm, see Fig. 69. The z position cut separating cathode from bulk was then defined to be  $z_{cut} = z_{max,MC} + 3\sigma_{fit}$ , where  $\sigma_{fit}$  is just the width of a Gaussian fit for the position of the cathode. Figures 70a and 70c show the cathode position fits as well the the location of  $z_{cut}$ . The cathode position fit error,  $\sigma_{fit}$ , was the same for both datasets A and B, and was also used to determine  $z_{cut}$  for the background and calibration sets.

One feature that merits further discussion from Figure 70 is the strong anti-correlation in S1 Pulse Area vs. S2 Pulse Area apparent in cathode events. The cathode region was subject to very high, non-uniform fields due to the thin wires that comprised the cathode grid. Events that occurred on the wires encountered different fields depending on their position on the surface of the wire. Additionally, two events that occurred at exactly the same spot encountered different fields depending on which direction the decay particle (alpha, beta, etc.) traveled. The amount of scintillation and ionization from an interaction in liquid xenon depends on the field at the interaction site. Higher fields result in more ionization electrons being separated from the interaction site and therefore more S2. Mono-energetic events occurring in a uniform field have small anti-correlated fluctuations in S1 and S2 size. Non-uniform fields greatly exaggerate the typical variation in S1 and S2 size resulting in the spread out cathode region (blue) observed in Figures 70 and 71 (right). Events in the bulk region encounter a relatively low, uniform field resulting in a compact signal region in S1 vs. S2 (visible in red region of calibration data, Dataset D).

## 7.4 RESULTS AND DISCUSSION

We observed 11 bulk  $^{212}\text{Bi}$  alphas for dataset A, 20 for dataset B, and 1 background event in the signal region from dataset C. The counts of cath-

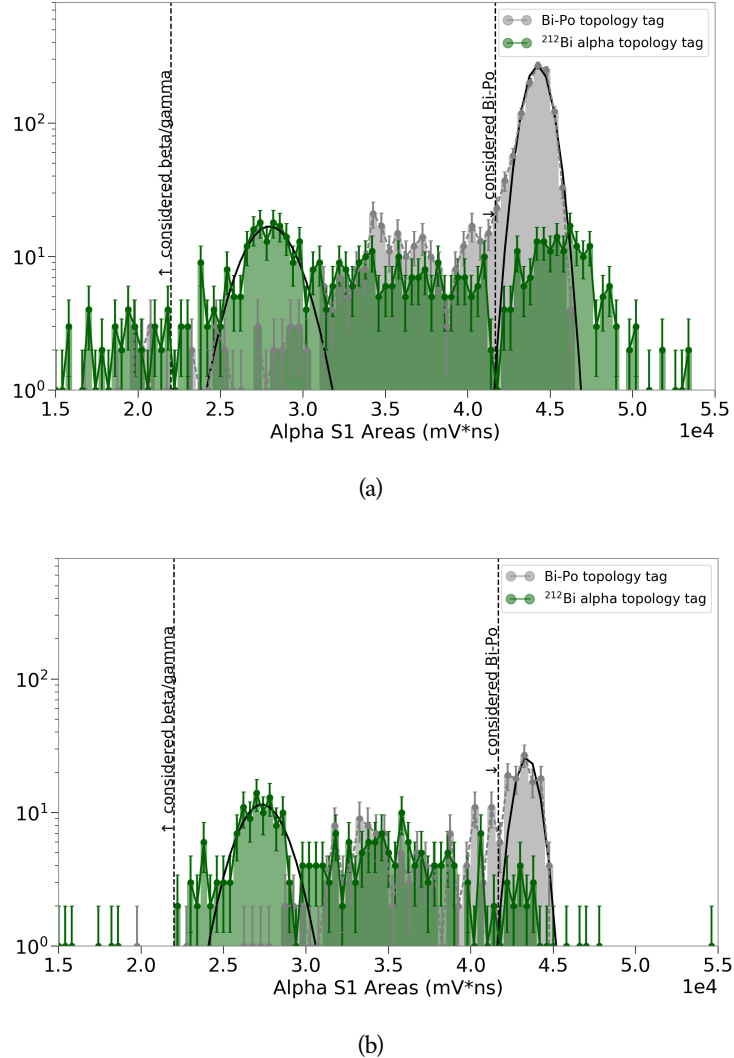


Figure 68: The S1 areas of events that were tagged using topological features.

These distributions were then used to employ the cuts in Step 3. The branching ratio for  $^{212}\text{Bi}$  is 36:64 for  $\alpha$ :Bi-Po. Dataset (a) showed 10:90 and dataset (b) showed 35:65. It is unclear why the branching ratios for dataset (a) deviate so much from expectation. The trigger is more efficient for Bi-Po events because those decays would produce more a larger charge signal. It's possible that the cathode being left on during the plate out procedure had some effect on the geometrical distribution of daughters on the cathode wires, which further biased the trigger.

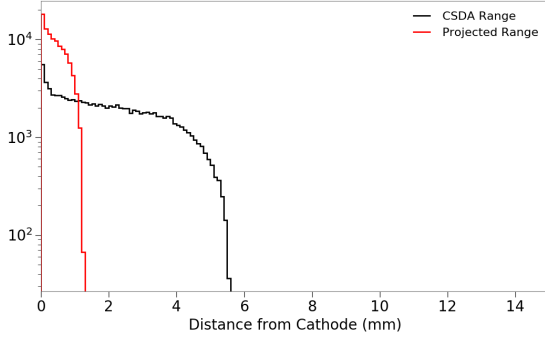


Figure 69: Monte Carlo study to find the maximum distance a  $^{212}\text{Bi}$  beta (2.2 MeV) on the cathode could penetrate into the drift region. The projected range (red) is the relevant curve for this analysis; it shows a beta is not expected to travel more than 1.2mm from the cathode.

ode region  $^{212}\text{Bi}$  alphas are presented in Table 3. There was only one background event observed in the signal region, so with 95% confidence the true background count is at most 4.74. The observed counts for dataset A and B lie far above the 95% confidence limit for background, indicating they are true observations of  $^{212}\text{Bi}$  alphas in bulk. Defining dissolved fraction as  $N_{bulk} / N_{cath}$ , the dissolved fraction of  $^{212}\text{Bi}$  alphas for dataset A ( $\approx 13$  h livetime) is  $0.035 \pm 0.010$ , and for data set B ( $\approx 25$  h livetime) is  $0.099 \pm 0.020$ .

These results indicate that either  $^{212}\text{Pb}$  or  $^{212}\text{Bi}$  itself is soluble to a small degree in liquid xenon.

Table 3: Number of detected alpha particle events whose energy determination was consistent with  $^{212}\text{Bi}$  decay to  $^{208}\text{Tl}$ . Live times are quoted in Table 1

dataset ID:	A	B	C
Bulk Events	11	20	1
Cathode Events	300	183	4

The solubility is presented in the following units:

$$\frac{\frac{Bq (dissolved)}{kg LXe}}{\frac{Bq (plated out)}{cm^2 (detector surface)}}$$

## 7.4 RESULTS AND DISCUSSION

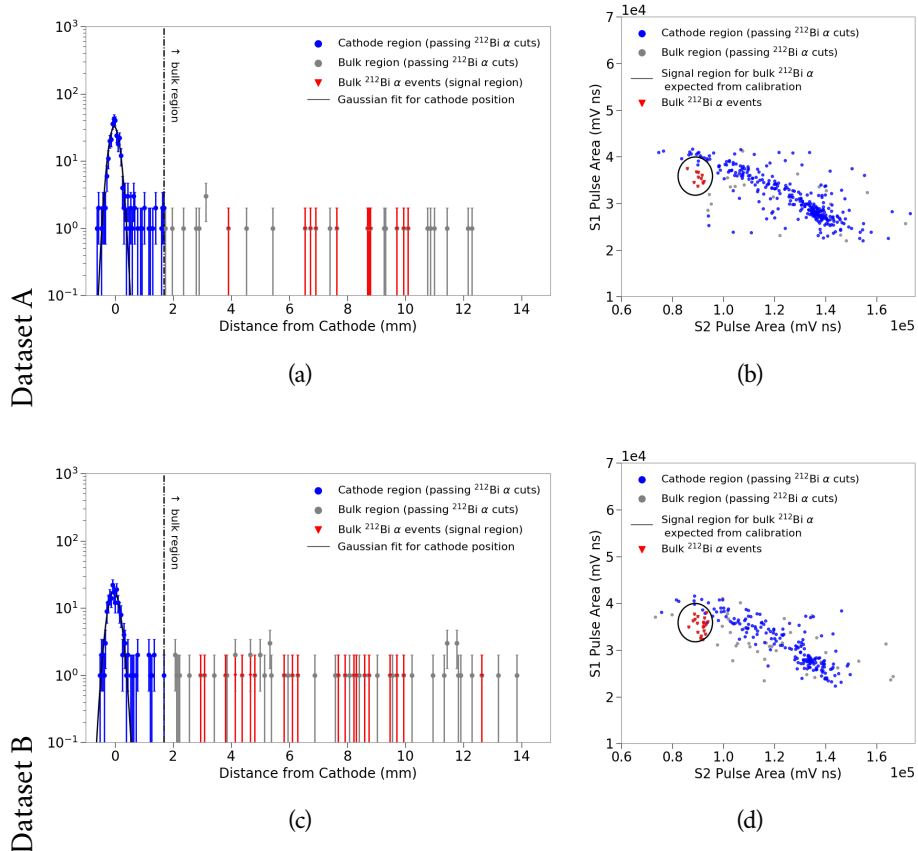


Figure 70: For datasets A and B: **(left)** Distribution of events in  $z$ . **(right)** The same events distributed in the  $S_1 - S_2$  plane, showing selection criteria for candidate  $^{212}\text{Bi}$  alpha events in the bulk liquid xenon.

## 7.4 RESULTS AND DISCUSSION

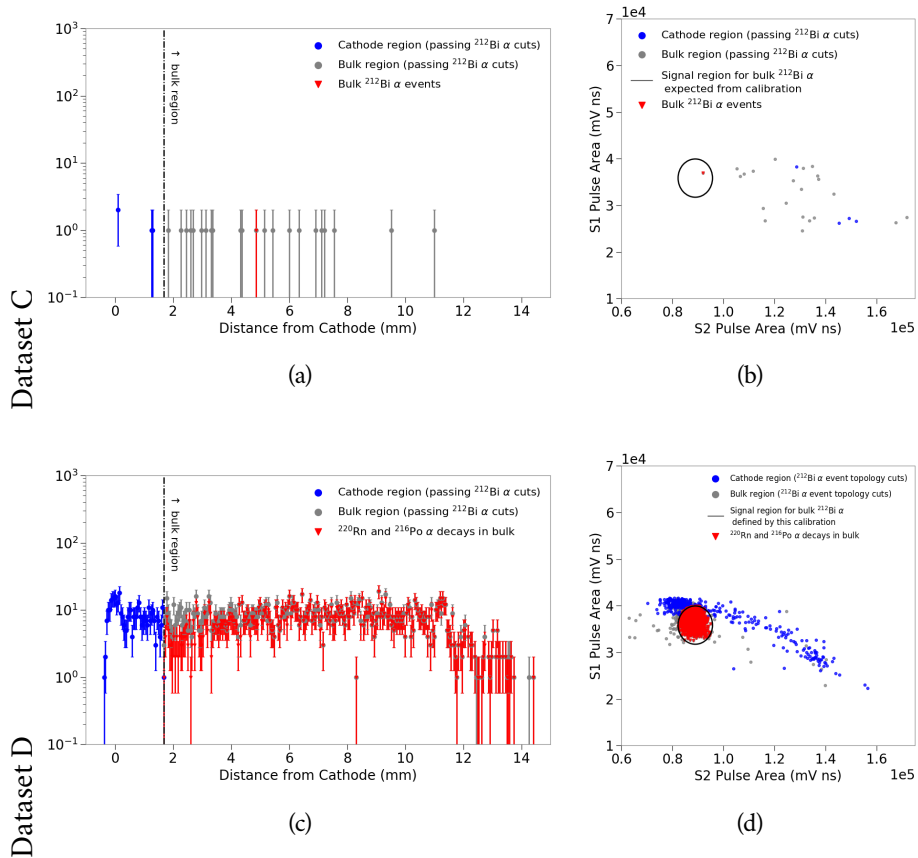


Figure 71: For datasets C and D: **(left)** Distribution of events in  $z$ . **(right)** The same events distributed in the S1-S2 plane, showing selection criteria for candidate  $^{212}\text{Bi}$  alpha events in the bulk liquid xenon.

The solubility calculation is subject to errors from the following factors. Where appropriate, it is noted how the error taken into account in the calculation; otherwise, the assumption is stated.

1. Liquid height (folded into fiducial volume)
2. Area over which charge amps are sensitive (calculation using different fiducial volumes)
3. Area over which daughters are plated out (varying area over which  $^{212}\text{Bi}$  is distributed; assume 10% error in area calculation)
4. Initial activity of plated out daughters (assume circulation time for gas to leave inner PTFE stack > decay time of  $^{216}\text{Po}$ )
5. Live time calculation (uncertainty included)

The solubility found in dataset A is at worst  $84 \pm 26 \text{ Bq/kg/Bq/cm}^2$  and at best  $0.091 \pm 0.030 \text{ Bq/kg/Bq/cm}^2$ . For dataset B, the worst case is  $58. \pm 18. \text{ Bq/kg/Bq/cm}^2$  and the best case is  $0.064 \pm 0.021 \text{ Bq/kg/Bq/cm}^2$ .

These results are first evidence that the  $^{220}\text{Rn}$  daughters  $^{212}\text{Pb}$  and/or  $^{212}\text{Bi}$  are soluble in liquid xenon. The dissolved events are a small fraction of events that are plated-out on detector surfaces. These daughters are proxies for the isotopes  $^{210}\text{Pb}$  and/or  $^{210}\text{Bi}$ , which undergo naked beta decays in the  $^{222}\text{Rn}$  chain and pose a problem for liquid xenon dark matter detectors. Our study counts dissolved  $^{212}\text{Bi}$  alpha events as well as  $^{212}\text{Bi}$  alphas plated out on the cathode. We found 11 counts in dataset A and 20 counts in dataset B consistent with  $^{212}\text{Bi}$  decay in the bulk region; these counts are significantly above a background count of 1. The experimental apparatus is not characterized extensively. Regardless, we carried through the solubility calculation, taking into account uncertainties to arrive at a ‘best case’ and ‘worst case’ result.

The limit derived from LUX observations, stated in the LZ projected sensitivity paper [85], is  $0.1 \mu \text{Bq/kg LXe}$  for  $^{212}\text{Bi}$  mobility, given  $50 \text{nBq/cm}^2$  on PTFE panels. Our observed solubility is much greater than this. One explanation is that we are sensitive to the ‘stuck’ radon daughters that wash off easily in the first few days of an experiment due to the introduction of [LXe](#). Large TPCs may then expect an increased rate of radon daughter decays in the fiducial volume at the beginning of a search, but a decreasing rate as these are removed by the getter or are implanted in detector materials.

Another, testable, explanation that would reconcile the different solubilities in the  $^{220}\text{Rn}$  and  $^{222}\text{Rn}$  chain is beta ejection. Referring to Figures ?? and ??, both bottleneck decays,  $^{XXX}\text{Pb}$ , are beta decays. However,  $^{212}\text{Pb}$  in the  $^{220}\text{Rn}$  chain has a beta decay endpoint of 570 keV, which

## 7.4 RESULTS AND DISCUSSION

about 10 times of the endpoint energy for  $^{210}\text{Pb}$  in the  $^{222}\text{Rn}$  chain. Daughter recoils from beta decay are indeed small; the endpoints are approximately 0.6 eV for the recoil from  $^{212}\text{Pb}$  decay in the  $^{220}\text{Rn}$  chain and 0.006 eV for the recoil from  $^{210}\text{Pb}$  decay in the  $^{222}\text{Rn}$  chain. The physisorption potential in for both cases is expected to be below 1 eV. Depending on the exact value, which is unavailable, the  $^{212}\text{Pb}$  decay could provide enough energy to liberate the daughter  $^{212}\text{Bi}$  most of the time, whereas  $^{210}\text{Pb}$  decay produces a maximum recoil value below the potential depth.

Further study, where a known amount of  $^{220}\text{Rn}$  daughters are plated out on a known area is necessary to measure dissolution rates. Additional studies that compare the solubility of radon daughters adsorbed on different materials, and under different conditions (e.g. temperature) would also be useful. The effect of cleaning these surfaces before searching for dissolved daughters should also be investigated.

If beta recoil, not ‘washing’ by the  $\text{LXe}$ , is the cause of radon daughter solubility, then the high rate seen by this study of  $^{220}\text{Rn}$  can be reconciled with the low rate of  $^{222}\text{Rn}$  daughter dissolution seen in large experiments.

## 7.4 RESULTS AND DISCUSSION

Table 4: Using observations from 3, proceed through solubility calculation.

dataset ID:	A	B
Total Inferred Bi decays	$20 \pm 6$	$36 \pm 11$
Livetime (hours)	$12.02 \pm 0.5$	$23.93 \pm 0.5$
$\mu\text{Bq}$ Bi in bulk	$460 \pm 140$	$420 \pm 130$
Bq (dissolved) / kg LXe (smallest fiducial)	$0.42 \pm 0.13$	$0.38 \pm 0.12$
Bq (dissolved) / kg LXe (largest fiducial)	$0.0063 \pm 0.0020$	$0.0057 \pm 0.0018$

Plate-Out Areas		
	Area	
Total Internal Area Including PMT	$496 \text{ cm}^2$	
Active Region PTFE	$36 \text{ cm}^2$	

dataset ID:	A	B
Number of $^{212}\text{Bi}$ Plated-Out	13191	17280
Bq (plated-out)	2.5	3.2
Bq (plated) / $\text{cm}^2$ min	$0.0050 \pm 0.0005$	$0.0065 \pm 0.0007$
Bq (plated) / $\text{cm}^2$ max	$0.069 \pm 0.007$	$0.089 \pm 0.009$

Solubility		
dataset ID:	A	B
Solubility min	$0.091 \pm 0.030$	$0.064 \pm 0.021$
Solubility max	$84. \pm 26.$	$58. \pm 18.$

# 8

## ELECTRON TRAIN STUDIES

---

### 8.1 ELECTRON TRAIN STUDIES

8.1.1 MOTIVATION

8.1.2 EXPERIMENTAL CONFIGURATION

8.1.3 RESULTS

PART IV

## APPENDIX

# A

## DUMMY APPENDIX

---

## BIBLIOGRAPHY

---

- [1] F Zwicky. “Die Rotverschiebung von extragalaktischen Nebeln”. In: *Helv. Phys. Acta* **6**: (1933), pp. 110–127. ISSN: 0018-0238. arXiv: [arXiv:1011.1669v3](https://arxiv.org/abs/1011.1669v3). URL: [http://adsabs.harvard.edu/cgi-bin/nph-data\query?bibcode=1933AcHPH...6..110Z\&link\type=GIF%5Cnpapers2://publication/uuid/E29E0909-762A-4A9D-B5B6-B850822D944A](http://adsabs.harvard.edu/cgi-bin/nph-data&query?bibcode=1933AcHPH...6..110Z&linktype=GIF%5Cnpapers2://publication/uuid/E29E0909-762A-4A9D-B5B6-B850822D944A).
- [2] Gianfranco Bertone and Dan Hooper. “A History of Dark Matter”. In: (2016), pp. 1–88. arXiv: [1605.04909](https://arxiv.org/abs/1605.04909). URL: <http://arxiv.org/abs/1605.04909>.
- [3] Vera C Rubin and W Kent Ford. “Rotation of the Andromeda Nebula From a Spectroscopic Survey of Emission Regions”. In: *Astrophys. J.* **159**: February (1970).
- [4] J.P. Ostriker and P.J.E Peebles. “A Numerical Study of the Stability of Flattened Galaxies: Or, Can Cold Galaxies Survive?” In: *Astrophys. J.* **186**: (1973), pp. 467–480.
- [5] Vera C Rubin, W Kent Ford, and Norbert Thonnard. “Rotational Properties of 21 Sc Galaxies with a Large Range of Luminosities and Radii, from NGC 4605 (R=4kpc) to UGC 2885 (R=122kpc)”. In: *Astrophys. J.* **238**: (1980), pp. 471–487.
- [6] M. Milgrom. “A Modification Of the Newtonian Dynamics as a Possible Alternative to the Hidden Mass Hypothesis”. In: *Astrophys. J.* **270**: (1983), pp. 365–370.
- [7] M. Milgrom. “A Modification of the Newtonian Dynamics: Implications for Galaxies”. In: *Astrophys. J.* **270**: (1983), pp. 371–383.
- [8] M. Milgrom. “A Modification of the Newtonian Dynamics: Implications for Galaxy Systems”. In: *Astrophys. J.* **270**: (1983), pp. 384–389.
- [9] T. S. van Albada, J. N. Bahcall, K. Begeman, and R. Sanscisi. “Distribution of Dark Matter in the Spiral Galaxy NGC 3198”. In: *Astrophys. J.* **295**: (1985), pp. 305–313.
- [10] Julio F. Navarro, Carlos S. Frenk, and Simon D. M. White. “The Structure of Cold Dark Matter Halos”. In: *Astrophys. J.* **462**: (1996), p. 563. ISSN: 0004-637X. arXiv: [9508025 \[astro-ph\]](https://arxiv.org/abs/astro-ph/9508025). URL: <http://adsabs.harvard.edu/doi/10.1086/177173>.

- [11] W. J. G. de Blok, Stacy S. McGaugh, Albert Bosma, and Vera C. Rubin. “Mass Density Profiles of Low Surface Brightness Galaxies”. In: *Astrophys. J.* **552**:1 (2001), pp. L23–L26. ISSN: 0004637X. arXiv: [0103102 \[astro-ph\]](#). URL: <http://stacks.iop.org/1538-4357/552/i=1/a=L23>.
- [12] W.J. G. de Blok, Stacy S. McGaugh, and Vera C. Rubin. “High-Resolution Rotation Curves of Low Surface Brightness Galaxies. II. Mass Models”. In: *Astron. J.* **122**:5 (2001), pp. 2396–2427. ISSN: 00046256. arXiv: [0107326 \[astro-ph\]](#). URL: <http://stacks.iop.org/1538-3881/122/i=5/a=2396>.
- [13] Kyle A. Oman et al. “The unexpected diversity of dwarf galaxy rotation curves”. In: *Mon. Not. R. Astron. Soc.* **452**:4 (2015), pp. 3650–3665. ISSN: 13652966. arXiv: [1504.01437](#).
- [14] Davide Martizzi, Romain Teyssier, and Ben Moore. “Cusp-core transformations induced by AGN feedback in the progenitors of cluster galaxies”. In: *Mon. Not. R. Astron. Soc.* **432**:3 (2013), pp. 1947–1954. ISSN: 00358711. arXiv: [1211.2648](#).
- [15] Jonah Herzog-Arbeitman, Mariangela Lisanti, Piero Madau, and Lina Necib. “Empirical Determination of Dark Matter Velocities Using Metal-Poor Stars”. In: *Phys. Rev. Lett.* **120**:4 (2018), p. 41102. ISSN: 10797114. arXiv: [1704.04499](#). URL: <https://doi.org/10.1103/PhysRevLett.120.041102>.
- [16] Lina Necib, Mariangela Lisanti, and Vasily Belokurov. “Dark Matter in Disequilibrium: The Local Velocity Distribution from SDSS-Gaia”. In: (2018), pp. 1–21. arXiv: [1807.02519](#). URL: <http://arxiv.org/abs/1807.02519>.
- [17] Denis Erkal, Sergey E. Koposov, and Vasily Belokurov. “A sharper view of Pal 5’s tails: Discovery of stream perturbations with a novel non-parametric technique”. In: *Mon. Not. R. Astron. Soc.* **470**:1 (2017), pp. 60–84. ISSN: 13652966. arXiv: [1609.01282](#).
- [18] Nilanjan Banik, Gianfranco Bertone, Jo Bovy, and Nassim Bozorgnia. “Probing the nature of dark matter particles with stellar streams”. In: *J. Cosmol. Astropart. Phys.* **2018**:7 (2018). ISSN: 14757516. arXiv: [1804.04384](#).
- [19] M. Markevitch, A. H. Gonzalez, L. David, A. Vikhlinin, S. Murray, W. Forman, C. Jones, and W. Tucker. “A Textbook Example of a Bow Shock in the Merging Galaxy Cluster 1E0657-56”. In: (2001). ISSN: 0004-637X. arXiv: [0110468 \[astro-ph\]](#). URL: <http://arxiv.org/abs/astro-ph/0110468{\%}0Ahttp://dx.doi.org/10.1086/339619>.

- [20] Douglas Clowe, Marusa Bradac, Anthony H. Gonzalez, Maxim Markevitch, Scott W. Randall, Christine Jones, and Dennis Zaritsky. “A direct empirical proof of the existence of dark matter”. In: (2006). ISSN: 0004-637X. arXiv: [0608407 \[astro-ph\]](#). URL: <http://arxiv.org/abs/astro-ph/0608407{\%}0Ahttp://dx.doi.org/10.1086/508162>.
- [21] George F. Smoot. “COBE observations and results”. In: *Conf. 3K Cosmol.* (1999), pp. 1–10. arXiv: [9902027 \[astro-ph\]](#). URL: <http://aip.scitation.org/doi/abs/10.1063/1.59326>.
- [22] Wayne Hu. “Lecture Notes on CMB Theory: From Nucleosynthesis to Recombination”. In: (2008). arXiv: [0802.3688](#). URL: <http://arxiv.org/abs/0802.3688>.
- [23] Planck Collaboration. “Planck 2018 Results VI Cosmological parameters”. In: **62**: (2018), pp. 1–71. arXiv: [arXiv:1807.06209v1](#). URL: <https://pla.esac.esa.int>.
- [24] Chris Quigg. “Cosmic Neutrinos”. In: (2008). arXiv: [0802.0013](#). URL: <http://arxiv.org/abs/0802.0013>.
- [25] Steen Hannestad. “Cosmological neutrinos”. In: (2004). arXiv: [0404239 \[hep-ph\]](#). URL: <http://arxiv.org/abs/hep-ph/0404239{\%}0Ahttp://dx.doi.org/10.1088/1367-2630/6/1/108>.
- [26] Jonathan L. Feng. “Dark Matter Candidates from Particle Physics and Methods of Detection”. In: (2010), pp. 495–547. ISSN: 0066-4146. arXiv: [1003.0904](#). URL: <http://arxiv.org/abs/1003.0904{\%}0Ahttp://dx.doi.org/10.1146/annurev-astro-082708-101659>.
- [27] Mariangela Lisanti. “Lectures on Dark Matter Physics”. In: (2016). arXiv: [1603.03797](#). URL: [http://arxiv.org/abs/1603.03797{\%}0Ahttp://dx.doi.org/10.1142/9789813149441{\%}\\_0007](http://arxiv.org/abs/1603.03797{\%}0Ahttp://dx.doi.org/10.1142/9789813149441{\%}_0007).
- [28] D. S. Akerib et al. “Chromatographic separation of radioactive noble gases from xenon”. In: *Astropart. Phys.* **97**: (2018), pp. 80–87. ISSN: 09276505. arXiv: [1605.03844](#).
- [29] E. Aprile et al. “Removing krypton from xenon by cryogenic distillation to the ppq level”. In: *Eur. Phys. J. C* **77**:5 (2017). ISSN: 14346052. arXiv: [1612.04284](#).
- [30] Carl Eric Dahl. “The physics of background discrimination in liquid xenon, and first results from Xenon10 in the hunt for WIMP dark matter.” In: PhD Thesis (2009).

- [31] J. Mock, N. Barry, K. Kazkaz, D. Stolp, M. Szydagis, M. Tripathi, S. Uvarov, M. Woods, and N. Walsh. “Modeling pulse characteristics in Xenon with NEST”. In: *J. Instrum.* **9**:4 (2014). issn: 17480221. arXiv: [arXiv:1310.1117v2](https://arxiv.org/abs/1310.1117v2).
- [32] K. Abe et al. “XMASS detector”. In: *Nucl. Instruments Methods Phys. Res. Sect. A Accel. Spectrometers, Detect. Assoc. Equip.* **716**: (2013), pp. 78–85. issn: 01689002. arXiv: [1301.2815](https://arxiv.org/abs/1301.2815).
- [33] XMASS Collaboration. “A direct dark matter search in XMASS-I”. In: (2018), pp. 1–23. arXiv: [1804 . 02180](https://arxiv.org/abs/1804.02180). URL: <http://arxiv.org/abs/1804.02180>.
- [34] F. Neves, A. Lindote, A. Morozov, V. Solovov, C. Silva, P. Bras, J. P. Rodrigues, and M. I. Lopes. “Measurement of the absolute reflectance of polytetrafluoroethylene (PTFE) immersed in liquid xenon”. In: *J. Instrum.* **12**:1 (2017). issn: 17480221. arXiv: [1612 . 07965](https://arxiv.org/abs/1612.07965).
- [35] C Faham. “Prototype, Surface Commissioning and Photomultiplier Tube Characterization for the Large Underground Xenon (LUX) Direct Dark Matter Search Experiment”. In: PhD Thesis (2014).
- [36] M. Auger et al. “The EXO-200 detector, part I: Detector design and construction”. In: *J. Instrum.* **7**:5 (2012). issn: 17480221. arXiv: [1202 . 2192](https://arxiv.org/abs/1202.2192).
- [37] D. S. Akerib et al. “Signal yields, energy resolution, and recombination fluctuations in liquid xenon”. In: *Phys. Rev. D* **95**:1 (2017), pp. 1–12. issn: 24700029. arXiv: [1610 . 02076](https://arxiv.org/abs/1610.02076).
- [38] C. H. Faham, V. M. Gehman, A. Currie, A. Dobi, P. Sorensen, and R. J. Gaitskell. “Measurements of wavelength-dependent double photoelectron emission from single photons in VUV-sensitive photomultiplier tubes”. In: *J. Instrum.* **10**:9 (2015). issn: 17480221. arXiv: [1506 . 08748](https://arxiv.org/abs/1506.08748).
- [39] D. S. Akerib et al. “Calibration, event reconstruction, data analysis and limits calculation for the LUX dark matter experiment”. In: *Phys. Rev. D* **97**:10 (2017), p. 102008. issn: 24700029. arXiv: [1712 . 05696](https://arxiv.org/abs/1712.05696). URL: <http://arxiv.org/abs/1712.05696>.
- [40] E. Aprile and T. Doke. “Liquid xenon detectors for particle physics and astrophysics”. In: *Rev. Mod. Phys.* **82**:3 (2010), pp. 2053–2097. issn: 00346861. arXiv: [0910 . 4956](https://arxiv.org/abs/0910.4956).
- [41] J Lindhard, V Nielsen, M Scharff, and P V Thomsen. “Integral equations governing radiation effects”. In: *Det Kgl. Danske Viden.* **33**:10 (1963). URL: <http://www.sdu.dk/bibliotek/materiale+efter+type/hostede+ressourcer/matfys>.

- [42] Peter Sorensen and Carl Eric Dahl. “Nuclear recoil energy scale in liquid xenon with application to the direct detection of dark matter”. In: *Phys. Rev. D - Part. Fields, Gravit. Cosmol.* **83**:6 (2011), pp. 1–6. issn: 15507998. arXiv: [1101.6080](https://arxiv.org/abs/1101.6080).
- [43] J. D. Lewin and P. F. Smith. “Review of mathematics, numerical factors, and corrections for dark matter experiments based on elastic nuclear recoil”. In: *Astropart. Phys.* **6**:1 (1996), pp. 87–112. issn: 09276505. arXiv: [1410.6160](https://arxiv.org/abs/1410.6160).
- [44] Laura Baudis. “WIMP dark matter direct-detection searches in noble gases”. In: *Phys. Dark Universe* **4**: (2014), pp. 50–59. issn: 22126864. arXiv: [1408.4371](https://arxiv.org/abs/1408.4371). url: <http://dx.doi.org/10.1016/j.dark.2014.07.001>.
- [45] V. Chepel and H. Araújo. “Liquid noble gas detectors for low energy particle physics”. In: *J. Instrum.* **8**:4 (2013). issn: 17480221. arXiv: [1207.2292](https://arxiv.org/abs/1207.2292).
- [46] U Oberlack. “First limits on WIMP dark matter from the XENON10 experiment”. In: *J. Phys. Conf. Ser.* **110**:6 (2008), p. 062020. issn: 1742-6596. url: <http://stacks.iop.org/1742-6596/110/i=6/a=062020?key=crossref.bfd78c6898a820849cdc54a2974555a3>.
- [47] D. S. Akerib et al. “First results from the LUX dark matter experiment at the Sanford Underground Research Facility”. In: *Phys. Rev. Lett.* **112**: (2014). issn: 0031-9007, 1079-7114. arXiv: [arXiv:1310.8214](https://arxiv.org/abs/1310.8214). url: <http://arxiv.org/abs/1310.8214>.
- [48] E. Aprile et al. “First dark matter results from the XENON100 experiment”. In: *Phys. Rev. Lett.* **105**:13 (2010), pp. 9–13. issn: 00319007. arXiv: [1005.0380](https://arxiv.org/abs/1005.0380).
- [49] P. Sorensen et al. “Lowering the low-energy threshold of xenon detectors”. In: *Proc. Sci.* (2010). issn: 18248039. arXiv: [arXiv:1011.6439v1](https://arxiv.org/abs/1011.6439v1).
- [50] Peter Sorensen. “Anisotropic diffusion of electrons in liquid xenon with application to improving the sensitivity of direct dark matter searches”. In: *Nucl. Instruments Methods Phys. Res. Sect. A Accel. Spectrometers, Detect. Assoc. Equip.* **635**:1 (2011), pp. 41–43. issn: 01689002. arXiv: [1102.2865 \[astro-ph.IM\]](https://arxiv.org/abs/1102.2865).
- [51] J. Angle et al. “Search for light dark matter in XENON10 data”. In: *Phys. Rev. Lett.* **107**:5 (2011), pp. 1–6. issn: 10797114. arXiv: [1104.3088](https://arxiv.org/abs/1104.3088).

- [52] Rouven Essig, Aaron Manalaysay, Jeremy Mardon, Peter Sorensen, and Tomer Volansky. “First direct detection limits on Sub-GeV dark matter from XENON10”. In: *Phys. Rev. Lett.* **109**:2 (2012), pp. 1–5. ISSN: 00319007. arXiv: [1206.2644](https://arxiv.org/abs/1206.2644).
- [53] D. S. Akerib et al. “A search for annual and diurnal rate modulations in the LUX experiment”. In: (2018), pp. 1–12. arXiv: [1807.07113](https://arxiv.org/abs/1807.07113). URL: <http://arxiv.org/abs/1807.07113>.
- [54] D. S. Akerib et al. “First Searches for Axions and Axionlike Particles with the LUX Experiment”. In: *Phys. Rev. Lett.* **118**:26 (2017), pp. 1–7. ISSN: 10797114. arXiv: [1704.02297](https://arxiv.org/abs/1704.02297).
- [55] Nicole A Larsen. “An Effective Field Theory Analysis of the First LUX Dark Matter Search”. In: PhD Thesis (2016).
- [56] A. Dobi, C. Davis, C. Hall, T. Langford, S. Slutsky, and Y. R. Yen. “Detection of krypton in xenon for dark matter applications”. In: *Nucl. Instruments Methods Phys. Res. Sect. A Accel. Spectrometers, Detect. Assoc. Equip.* **665**: (2011), pp. 1–6. ISSN: 01689002. arXiv: [1103.2714](https://arxiv.org/abs/1103.2714) [astro-ph]. URL: <http://dx.doi.org/10.1016/j.nima.2011.11.043>.
- [57] D. S. Akerib et al. “The Large Underground Xenon (LUX) experiment”. In: *Nucl. Instruments Methods Phys. Res. Sect. A Accel. Spectrometers, Detect. Assoc. Equip.* **704**: (2013), pp. 111–126. ISSN: 01689002. arXiv: [1211.3788](https://arxiv.org/abs/1211.3788).
- [58] D.S. Akerib et al. “Radiogenic and muon-induced backgrounds in the LUX dark matter detector”. In: *Astropart. Phys.* **62**: (2015), pp. 33–46. ISSN: 09276505. arXiv: [1403.1299](https://arxiv.org/abs/1403.1299). URL: <http://dx.doi.org/10.1016/j.astropartphys.2014.07.009><http://linkinghub.elsevier.com/retrieve/pii/S0927650514001054>.
- [59] D. S. Akerib et al. “FPGA-based trigger system for the LUX dark matter experiment”. In: *Nucl. Instruments Methods Phys. Res. Sect. A Accel. Spectrometers, Detect. Assoc. Equip.* **818**: (2016), pp. 57–67. ISSN: 01689002. arXiv: [1511.03541](https://arxiv.org/abs/1511.03541).
- [60] A Currie et al. “Position Reconstruction in a Dual Phase Xenon Scintillation Detector”. In: *IEEE* **59**:6 (2012), pp. 3286–3293.
- [61] D. S. Akerib et al. “Position reconstruction in LUX”. In: *J. Instrum.* **13**:2 (2018). ISSN: 17480221. arXiv: [1710.02752](https://arxiv.org/abs/1710.02752).
- [62] D. S. Akerib et al. “83m-Kr calibration of the 2013 LUX dark matter search”. In: *Phys. Rev. D* **96**:11 (2017), p. 112009. ISSN: 2470-0010. arXiv: [arXiv:1708.02566v1](https://arxiv.org/abs/1708.02566v1). URL: <https://link.aps.org/doi/10.1103/PhysRevD.96.112009>.

- [63] D. S. Akerib et al. “Tritium calibration of the LUX dark matter experiment”. In: *Phys. Rev. D* **93**:7 (2016). issn: 24700029. arXiv: [1512.03133](https://arxiv.org/abs/1512.03133).
- [64] D. S. Akerib et al. “3D modeling of electric fields in the LUX detector”. In: *J. Instrum.* **12**: (2017), P11022.
- [65] D. S. Akerib et al. “Results from a Search for Dark Matter in the Complete LUX Exposure”. In: *Phys. Rev. Lett.* **118**:2 (2017), pp. 1–8. issn: 10797114. arXiv: [1608.07648](https://arxiv.org/abs/1608.07648).
- [66] LUX Collaboration et al. “Low-energy (0.7-74 keV) nuclear recoil calibration of the LUX dark matter experiment using D-D neutron scattering kinematics”. In: (2016), pp. 1–24. issn: 15502368. arXiv: [1608.05381](https://arxiv.org/abs/1608.05381). URL: <http://arxiv.org/abs/1608.05381>.
- [67] D. S. Akerib et al. “Improved Limits on Scattering of Weakly Interacting Massive Particles from Reanalysis of 2013 LUX Data”. In: *Phys. Rev. Lett.* **116**:16 (2016), pp. 1–7. issn: 10797114. arXiv: [1512.03506](https://arxiv.org/abs/1512.03506).
- [68] C. et al. (Particle Data Group) Patrignani. “Passage of Particles Through Matter”. In: *PDG* (2017). issn: 1434-6044. URL: <http://dbcompas.ihep.su/2006/reviews/passagerpp.pdf>.
- [69] H. Bethe. “Zur Theorie des Durchgangs schneller Korpuskularstrahlen durch Materie”. In: *Ann. Phys.* **5**: (1930), pp. 325–400. issn: 15213889.
- [70] U Fano. “Penetration of Protons, Alpha Particles, and Mesons12”. In: *Ann. Rev Nucl. Scei* **12**: (1963), pp. 1–66. URL: [https://www.google.com/books?hl=tr&lr={\&}id=I6wrAAAAYAAJ{\&}oi=fnd{\&}pg=PA287{\&}dq=Fano,+U.+ \(1964\).+Penetrations+of+protons,+alpha+particles,+and+mesons.+Studies+in+Penetra+tion+of+Charged+Particles+in+Matter,++1133 : 287. +\(cited+on+pages+15 , +16 , +and+17 \) {\&}ots=PYmM1cE](https://www.google.com/books?hl=tr&lr={\&}id=I6wrAAAAYAAJ{\&}oi=fnd{\&}pg=PA287{\&}dq=Fano,+U.+ (1964).+Penetrations+of+protons,+alpha+particles,+and+mesons.+Studies+in+Penetra+tion+of+Charged+Particles+in+Matter,++1133 : 287. +(cited+on+pages+15 , +16 , +and+17 ) {\&}ots=PYmM1cE).
- [71] Hans Bichsel. “A method to improve tracking and particle identification in TPCs and silicon detectors”. In: *Nucl. Instruments Methods Phys. Res. Sect. A Accel. Spectrometers, Detect. Assoc. Equip.* **562**:1 (2006), pp. 154–197. issn: 01689002.
- [72] J.H. Allison, W. W. M ; Cobb. “Relativistic Charged Particle Identification By Energy Loss”. In: *Ann. Rev. Nucl. Part. Sci.* **30**: (1980), pp. 253–298.
- [73] V. E. Guiseppe, S. R. Elliott, A. Hime, K. Rielage, and S. Westerdale. “A Radon Progeny Deposition Model”. In: 2011, pp. 95–100. URL: <http://aip.scitation.org/doi/abs/10.1063/1.3579565>.

- [74] E. O. Knutson. "Radon and Its Decay Products in Indoor Air". Wiley, 1988.
- [75] Yasuhiro Takemoto. "7Be solar neutrino observation with KamLAND". In: *Nucl. Part. Phys. Proc.* **265-266**: (2015), pp. 139–142. issn: 24056014. url: <http://linkinghub.elsevier.com/retrieve/pii/S2405601415003788>.
- [76] A. Gando et al. "Be 7 solar neutrino measurement with KamLAND". In: *Phys. Rev. C* **92**:5 (2015), p. 055808. issn: 0556-2813. url: <https://link.aps.org/doi/10.1103/PhysRevC.92.055808>.
- [77] G. Bellini et al. "Final results of Borexino Phase-I on low-energy solar neutrino spectroscopy". In: *Phys. Rev. D* **89**:11 (2014), p. 112007. issn: 1550-7998. url: <https://link.aps.org/doi/10.1103/PhysRevD.89.112007>.
- [78] Christer Samuelsson. "Plate-out and Implantation of 222Rn Decay Products in Dwellings". In: *Environ. Int. Vol.* **22**:Suppl. 1 (1996), pp. 839–843.
- [79] Lawrence Stein. "The Chemistry of Radon". In: *Radiochim. Acta* **32**: (1982), pp. 163–171. issn: 0036-8075.
- [80] Lawrence Stein. "Chapter 18 Chemical Properties of Radon". In: *Radon Its Decay Prod.* 1987, pp. 240–251.
- [81] J.K. Hammer, B; Norskov. "Theory of adsorption and surface reactions". In: (1997), pp. 285–351.
- [82] J . Bigu. "Plate-Out of Radon and Thoron Progeny on Large Surfaces". In: *Radon Its Decay Prod.* 1987. Chap. 21, pp. 272–284.
- [83] E S Morrison, T Frels, E H Miller, R W Schnee, and J Street. "Radon daughter plate-out onto Teflon." In: *arXiv.org, e-Print Arch. Phys.* **090002**: (2017), pp. 1–4. issn: 15517616. url: <http://arxiv.org/pdf/1708.08534.pdf>.
- [84] M. Bruemmer, M. Nakib, R. Calkins, J. Cooley, and S. Sekula. "Studies on the reduction of radon plate-out". In: *AIP Conf. Proc.* **1672**: (2015). issn: 15517616. arXiv: <1506.04050>.
- [85] D. S. Akerib et al. "Projected WIMP sensitivity of the LUX-ZEPLIN (LZ) dark matter experiment". In: (2018), pp. 1–16. arXiv: <1802.06039>. url: <http://arxiv.org/abs/1802.06039>.